UNIVERSITY OF CALIFORNIA,

IRVINE

Sensor Validation and Digital Biomarker Exploration for Health Monitoring

DISSERTATION

submitted in partial satisfaction of the requirements
for the degree of

DOCTOR OF PHILOSOPHY

in Biomedical Engineering

by

En Fan (Sophia) Chou

Dissertation Committee:
Professor Michelle Khine, Chair
Professor Bernard Choi
Professor Beth Lopour
Professor Shaista Malik

2023

DEDICATION

To my mom, Hsiao-Yeh Chou,
who sacrifices daily for me and helps shape me into the person I am today.
I am forever thankful for your unconditional love and may I make you forever proud.

To my sister, Ting-Yu Lynn Chou,
who has been a great companion since the day I was born.

To the patients and their families who are suffering still,
I hope this dissertation gives you hope toward the battle.

Glory to God

TABLE OF CONTENTS

LIST OF FIGURES

LIST OF TABLES

LIST OF ABBREVIATIONS

Abbreviation	Explanation
A-Line	Arterial line
AAMI	Association for the advancement of medical instrumentation
AASM	American Academy of Sleep Medicine
ADL	Average diagonal line length
AHI	Apnea-hypopnea index
AMI	Average mutual information
ANSI	American national standards institute, Inc.
ApEn	Approximate entropy
BMI	Body mass index
BP	Blood pressure
CAD	Coronary artery disease
CAP	The wireless soft capacitive pressure sensor
CPAP	Continuous positive airway pressure
CMSE	Composite multiscale entropy
CVD	Cardiovascular disease
DBP	Diastolic blood pressure
DFA	Detrended fluctuation analysis
EA	Electroacupuncture
ECG	Electrocardiography
EDF	European data format
EMR	Electronic medical records
ER	Emergency room
FDA	U.S. Food and Drug Administration
FFT	Fast Fourier Transform

HF	High-frequency
HF norm	Normalized high-frequency
HR	Heart rate
HRV	Heart rate variability
ICU	Intensive care unit
IDC	International data corporation
IDE	Integrated development environment
IEEE-SA	The Institute of Electrical and Electronics Engineers Standards Association
IMU	Inertial measurement unit
IPC	Intermittent pneumatic compression
ISO	International Organization for Standardization
LE	Lyapunov exponents
LF	Low-frequency
LF/HF	Ratio of low-frequency to high-frequency
LF norm	Normalized low-frequency
LLE	The largest Lyapunov exponent
MAD	Median absolute deviation
MAP	Mean arterial pressure
MDL	Maximum diagonal line length
mmHg	Millimeters of mercury
MODWT	Maximal overlap discrete wavelet transform
MSE	Multiscale entropy
NIBP	Noninvasive blood pressure
NN	Normal-to-normal
NREM	Non-rapid eye movement
OR	Operating room

OSA	Obstructive sleep apnea
PDMS	Polydimethylsiloxane
pF	Picofarad
pNN50	The percentage of successive normal-to-normal intervals greater than 50 ms in all normal-to-normal intervals
PPG	Photoplethysmography
PTT	Pulse transit time
PWV	Pulse waveform velocity
RDI	Respiratory disturbance index
RMSSD	Root mean square of standard deviation
RP	Recurrence plot
RQA	Recurrence quantification analysis
SampEn	Sample entropy
SBP	Systolic blood pressure
SDNN	Standard deviation of normal-to-normal interval
Sym4	Symlet 4 wavelet
ULF	Ultra-low-frequency
VLF	Very low-frequency
VLF norm	Normalized very low-frequency
wAu	Wrinkled Au
1D-CNN	One-dimensional convolutional neural network
%DET	Percent determinism
%REC	Percent recurrence

ACKNOWLEDGEMENTS

I would like to express my sincerest gratitude first and foremost to my advisor, Professor Michelle Khine, for her continued guidance throughout my graduate career. She has provided me tremendous opportunities, given me space to create solutions, and paved the way for my research career. As an advisor, Dr. Khine demonstrates what generosity and being supportive is. She was the one who knew it was the right path for me when I did not think I was ready. I would have not accomplished if it wasn't her pushing me to grow through the journey. Besides Dr. Khine, I would like to thank the rest of my committee members, Dr. Bernard Choi, Beth Lopour, and Shaista Malik, for all the encouragement, opinions, and suggestions that inspired and motivated me.

I would like to express my gratitude to collaborators in projects shown in this dissertation. Dr. Joseph Rinehart was supportive and enthusiastic in the project. He is intelligent and easy to work with. His willingness of spending time discussing the project together to work it out is precious and appreciated. In the project of ECG data length, I want to thank Dr. Rahul Soangra and Thurmon Lockhart for giving me a new perspective on collaboration. We worked together when the pandemic just started. It is amazing how we had the work done without meeting each other in person. The time Dr. Soangra had spent on the project with me is greatly appreciated. The work would not have been completed without his constant support and guidance. Next, I am grateful to Dr. Rami Khayat for offering a new field of study to expand my knowledge. The meetings and feedback he gave have contributed significantly to the fundamental of the project. Last but not the least, a thank you to the electroacupuncture team which includes Dr. Shaista Malik, Dr. Stephanie Tjen-A-Looi, and Dr. Lifang Xie. In addition, thank you Dr. Stephanie Tjen-A-Looi for being such an aspirational mentor. With your professional background and deep care, I admire your passion toward the truth in research.

Lastly, I would like to acknowledge the financial support received in my graduate career and the publishers' permission for reprinting material in this dissertation. Financial support was provided by Dr. Michelle Khine, Dr. Rami Khayat, Midmark Corporation, Department of Teaching Excellence and Innovation Fellowship and UC Irvine Graduate Division through the Public Impact Fellowship. The aforementioned publishers include Wiley-VCH GmbH, Frontiers, and Multidisciplinary Digital Publishing Institute (MDPI). Portion of Chapter 1 and 2 of this dissertation is a reprint of the material as it appears in the journal Advanced Healthcare Materials, used with permission from Wiley-VCH GmbH. The co-authors listed in this publication are J. Kim, J. Le, S. Wong, M. Chu, and M. Khine. Portion of Chapter 3 of this dissertation is a reprint of the material as it appears in the journal Frontiers in Digital Health which is granted by the Creative Commons CC-BY

license. The co-authors listed in this publication are S.Y.C. Cheung, H.C. Maxwell, N. Pham, M. Khine, and J. Rinehart. Portion of Chapter 4 of this dissertation is a reprint of the materials as it appears in the journal Sensors, an open access journal from MDPI. The co-authors listed in this publication are M. Khine, T. Lockhart, and R. Soangra.

VITA

En Fan (Sophia) Chou

2015	B.S. in Electrical Engineering, Chang Gung University, Taiwan
2015	Research Assistant, Research Center for Applied Sciences, Academia Sinica, Taiwan
2019-22	Graduate Student Researcher, University of California, Irvine
2021	Medical Science Intern, Genentech
2022	M.S. in Biomedical Engineering, University of California, Irvine
2023	Ph.D. in Biomedical Engineering, University of California, Irvine

FIELD OF STUDY

Integrated soft electronics for health monitoring and digital biomarker exploration

PUBLICATIONS

1. Abiri, A., **Chou, E. F.**, Qian, C., Rinehart, J., & Khine, M. (2022). Intra-beat biomarker for accurate continuous non-invasive blood pressure monitoring. *Scientific Reports*, *12*(1), 1-13.
2. Rwei, P., Qian, C., Abiri, A., Zhou, Y., **Chou, E. F.**, Tang, W. C., & Khine, M. (2022). Soft Iontronic Capacitive Sensor for Beat-to-Beat Blood Pressure Measurements. *Advanced Materials Interfaces*, 2200294.

3. **Chou, E. F.**, Cheung, S. Y. C., Maxwell, H. C., Pham, N., Khine, M., & Rinehart, J. (2021). Clinical Validation of a Soft Wireless Continuous Blood Pressure Sensor During Surgery. *Frontiers in Digital Health*, *3*, 696606.
4. Sprowls, M., Serhan, M., **Chou, E. F.**, Lin, L., Frames, C., Kucherenko, I., ... & Forzani, E. (2021). Integrated Sensing Systems for Monitoring Interrelated Physiological Parameters in Young and Aged Adults: A Pilot Study. *International Journal of Prognostics and Health Management*, *12*(4).
5. **Chou, E. F.**, Khine, M., Lockhart, T., & Soangra, R. (2021). Effects of ECG data length on heart rate variability among young healthy adults. *Sensors*, *21*(18), 6286.
6. Kim, J., **Chou, E. F.**, Le, J., Wong, S., Chu, M., & Khine, M. (2019). Soft wearable pressure sensors for beat-to-beat blood pressure monitoring. *Advanced healthcare materials*, *8*(13), 1900109.

HONORS AND AWARDS

2022 Graduate Division Completion Fellowship, University of California, Irvine

2022 Division of Teaching Excellence and Innovation (DTEI) Summer Fellowship, University of California, Irvine

2019 1st Place in the Beall Student Design Competition

ABSTRACT OF THE DISSERTATION

Sensor Validation and Digital Biomarker Exploration for Health Monitoring

by

En Fan (Sophia) Chou

Doctor of Philosophy in Biomedical Engineering

University of California, Irvine, 2023

Professor Michelle Khine, Chair

We live in an era where advanced technology is enhancing the quality of life. With the assistance of new medical devices and activity trackers, our knowledge and awareness of our own health and disease state have grown rapidly. However, existing products still suffer from severe limitations. For instance, hemodynamic monitoring is essential for specific populations with conditions, as hypotension and hypertension may impair vital organ function. Continuous monitoring provides more information about how blood pressure (BP) and heart rate (HR) fluctuate, but current sphygmomanometers provide only static measurements. While current medical-grade continuous BP monitors exist, they are limited to critically ill patients due to their bulkiness and price. On the other hand, activity-tracking smartwatches are either inaccurate or intermittent. We have been developing soft conformal pressure sensors that are lightweight, inexpensive, and comfortable to wear. The aims of this work include validating the performance of the sensor in tracking beat-to-beat BP and exploring how the data can be understood in various clinical settings. The pressure sensors were compared against both invasive and FDA-cleared noninvasive BP devices. In addition to the beat-to-beat absolute systolic and diastolic BP, the waveform shape

analysis, HR, HR variability (HRV), and temporal response to vasopressors show promising potential. Yet, how the data is interpreted is challenging even with accurate recordings from devices. For this reason, we explore continuous physiological data to determine its predictive capabilities in well-controlled clinical settings.

One promising digital biomarker that has been widely studied for the past several decades is heart rate variability (HRV). More and more methods of evaluating HRV have been proposed, yet its prognostic potential remains unclear. Hence, our first study covers the fundamentals of HRV analysis, including investigating the proper minimum data length of each common HRV measure in young healthy subjects. Next, we explore clinical applications via an ongoing sleep study and electroacupuncture (EA) study with our clinical collaborators. The apnea-hypopnea index (AHI) is commonly used to diagnose sleep apnea in clinical practice. A counterargument is that AHI cannot holistically represent the disorder without considering the full picture of physiological characteristics such as the durations and depths of oxygen desaturation episodes. To discover new indicators for the severity level of sleep apnea, we demonstrate that the nasal airflow signal alone could predict arousal using a deep learning method with an accuracy of 85%. For the EA clinical study, we seek to understand how this therapy regulates BP among hypertensive subjects. Throughout 8 weeks of EA at cardiovascular-specific acupoints, we assessed changes in both HRV and BPV.

INTRODUCTION

High-valued health care is inevitable in human society. The seeking of life-saving medical breakthroughs never ends. The pandemic, COVID-19, brought many a higher level of awareness of wellness while we mourn individual losses. To ensure quality of life, healthcare nowadays is taking a step towards preventive healthcare, decentralized monitoring, and data-driven science.

Besides the outbreak of COVID-19, society already exists tremendous healthcare issues such as the prevalence of chronic conditions and the growth of the geriatric population. Studies have shown that the elderly, especially with their comorbidities, tend to experience more severe symptoms and have a higher mortality rate with COVID-19.[1,2] With these concerns and the increasing consciousness of general health, the market of global wearable medical devices and health sensors is anticipated to expand.[3,4] Moreover, smartwatch companies are gradually stepping foot into this market for consumer health tracking. According to the International Data Corporation (IDC) report, Apple Watches had 6.6% year-over-year growth and dominated the wearables market with a 30.5% market share in Q1 2022 followed by Samsung, Xiaomi, and Huawei.[5] While more and more people track their activities with smartwatches or other digital health gadgets as part of their routine, the expectation of being capable to measure more sophisticated health metrics is becoming the norm. Hence, the challenges are not only obtaining the health data accuracy but also making it understandable.

The International Organization for Standardization (ISO) develops international standards to help understand the performance of health measurements. Furthermore, the

United States Food and Drug Administration (FDA) which regulates whether a medical device is safe and effective enough to be sold in the United States adopts ISO standards. With that being said, most of the commercially available products that support health information have a guideline to follow. On the other hand, numerous research articles reported the accuracy of medical devices and smartwatches.[6–12] Take blood pressure (BP) monitoring for example, a BP cuff, as a common piece of equipment in a doctor's office, it's a simple and convenient device. It provides valuable information on patients' cardiovascular health. Nevertheless, a single pair of BP results from a BP cuff can't truly assist this highly dynamic system. The critically ill patients at the hospital are often given arterial catheters for continuous BP monitoring. Unfortunately, only a select group of patients receive this procedure regarding how invasive it is.[13,14] Over the past decade, there has been growing interest in developing devices that can measure BP continuously and noninvasively. Most of these market-available BP monitors are very pricey, bulky, and not as accessible to the general public. Hence, it's not commonly used. On the other hand, wristwatch-like BP monitoring devices are considered more comfortable for daily normal activities. However, it is hard to find one with beat-to-beat BP tracking. Moreover, the accuracy of BP measurements is questionable.

Khine Lab has developed a soft conformal capacitive pressure sensor that is able to directly measure mechanical changes on the surface of the skin as the result of arterial pulsations. The focus of this dissertation is on validating the accuracy of this type of sensor for monitoring physiological signals from the cardiovascular system and investigating the potential biomarkers for clinical events and diseases. The dissertation is divided into the following parts. Chapter one discusses the advantages and disadvantages of existing BP

monitors and the objective of the present study. Chapter two reports the performance of BP monitoring between the Khine Lab pressure sensor and two FDA-approved NIBP systems. Chapter three shows the validation of the Khine Lab pressure sensor in comparison with the gold standard in a clinical setting. Besides the BP tracking ability of this system, it is also important to understand how to appropriately interpret the acquired physiological data. The following three chapters explore the usage of digital biomarkers and their potential to indicate or predict disease states. Chapter four aims to find the appropriate data length when it comes to calculating HRV measures. Chapters five and six show preliminary data from two ongoing clinical studies, the sleep and electroacupuncture study, respectively.

CHAPTER 1: Objective of present study

Portions of this chapter appears in the journal Advanced Healthcare Materials.[15]

Chapter 1.1: Objective of present study

Inspired by the late 80s children's toy, Shrinky Dinks, the wrinkled stretchable sensors developed in Khine Lab have the advantage of being mechanically reliable and low-cost. In addition, the elastomeric material of the sensors improves conformability to the human skin. Hence, these sensors can potentially be used for health monitoring as cheaper and easier-to-wear options.

The objective of this dissertation is to evaluate the ability of continuous beat-to-beat BP measurement using Khine Lab's soft capacitive pressure sensor by comparing it against the standard commercially available BP systems including both invasive and noninvasive methods. To validate the sensing performance, not only the accuracy of beat-to-beat BP values compared, but also the waveform similarity, heart rate (HR), and temporal response to a vasopressor. Moreover, potential digital biomarkers obtained from physiological measurements with the use of wearable sensors are explored. Specifically, the effect of data length on various heart rate variability (HRV) measures among healthy young subjects is discussed here.

Chapter 1.2: Standardization of BP monitor

Several organizations published the validation protocols for BP monitors:

1.2.1 The American National Standards Institute, Inc/Association for the Advancement of Medical Instrumentation/International Organization for Standardization (ANSI/AAMI/ISO)

As the standards development organizations, ANSI/AAMI/ISO provides a universal guideline for validation procedure of noninvasive BP (NIBP) measuring devices accuracy and performance.[16]

1.2.2 The Institute of Electrical and Electronics Engineers Standards Association (IEEE-SA)

In 2014, IEEE-SA published the standards focusing on wearable cuffless BP monitors (IEEE-SA 1708™). The standard includes all types of BP measuring wearable devices such as epidermal and unobtrusive ones. It is also not limited to intermittent or continuous BP measurements.

Chapter 1.3: Measurement techniques for cuffless NIBP monitor

Undoubtedly, BP monitoring is an essential practice to understand cardiovascular health. In the perioperative setting, acute fluctuations occurred often due to the changes in hemodynamic status from anesthesia and pain. The arterial line (A-Line) and digital sphygmomanometer are the two appropriate devices to monitor BP invasively and noninvasively, respectively. A-Line is considered the gold standard which measures BP directly through the cannulation of an artery. However, A-Line is associated with a variety of medical complications[17–20] and is required trained personnel to operate. There are less than half of the critically ill patients received it.[21] On the other hand, the digital sphygmomanometer which uses the oscillometric technique, using automated inflatable

brachial arm cuffs, is intermittent and only provides one systolic and diastolic BP value over a duration of ≈30–40 s.[22–24] The following sections discuss different techniques for BP monitoring that are noninvasive and continuous.

1.3.1 The volume clamp method

In 1976, Penaz et al. proposed an indirect method to monitor BP called the volume clamp method.[25] With a combination of an inflatable cuff and a photodiode, the method estimates the diameter of the artery and the pressure changes in the cuff. FDA-approved devices ClearSight™ (Edwards Lifesciences, Irvine, CA) and CNAP® (Monitor 500, distributed by BIOPAC® as NIBP100D) are based on this technique. These devices are considered easy and convenient to use; however, they are fairly bulky and pricey. They are mainly seen in a clinical setting but for one's daily BP tracking.

1.3.2 Pulse wave velocity/pulse transit time-based estimation

In theory, pulse wave velocity (PWV) describes how fast the pressure pulses propagate through an artery or the arterial tree whereas pulse transit time (PTT) provides information about the arrival time of a pressure pulse between two different arterial sites. It is often achieved using a combination of photoplethysmography (PPG) and electrocardiography (ECG) or two PPG sensors placed on two different sites. PWV can be viewed as the ratio of the distance between two regions of the human body (D) and the time that takes a pressure pulse to arrive from one arterial site to another (**Equation 1-1**)

$$PWV = \frac{D}{PTT} \tag{1-1}$$

While the implementation of this method does not require additional monitors, the correlation between PWV/PTT and BP is yet fully developed. Although knowing they are related, several studies have proposed models to show how PWV or PTT can estimate BP. Some researchers presented methods based on linear regression.[26–32] However, others argued that the relationship was not always linear.[33–35]

CHAPTER 2: Validation of soft wearable pressure sensors compared with commercially available noninvasive BP systems

Portions of this chapter appear in the journal Advanced Healthcare Materials.[15]

We introduce soft capacitive pressure sensors that incorporate highly wrinkled Au (wAu) thin films to develop soft stretchable electrodes for radial tonometry applications as shown in **Figure 2.1**. The wrinkled structures of the Au thin film create mechanical robustness for the thin film to repeatedly flex (**Figure 2.1.b**).

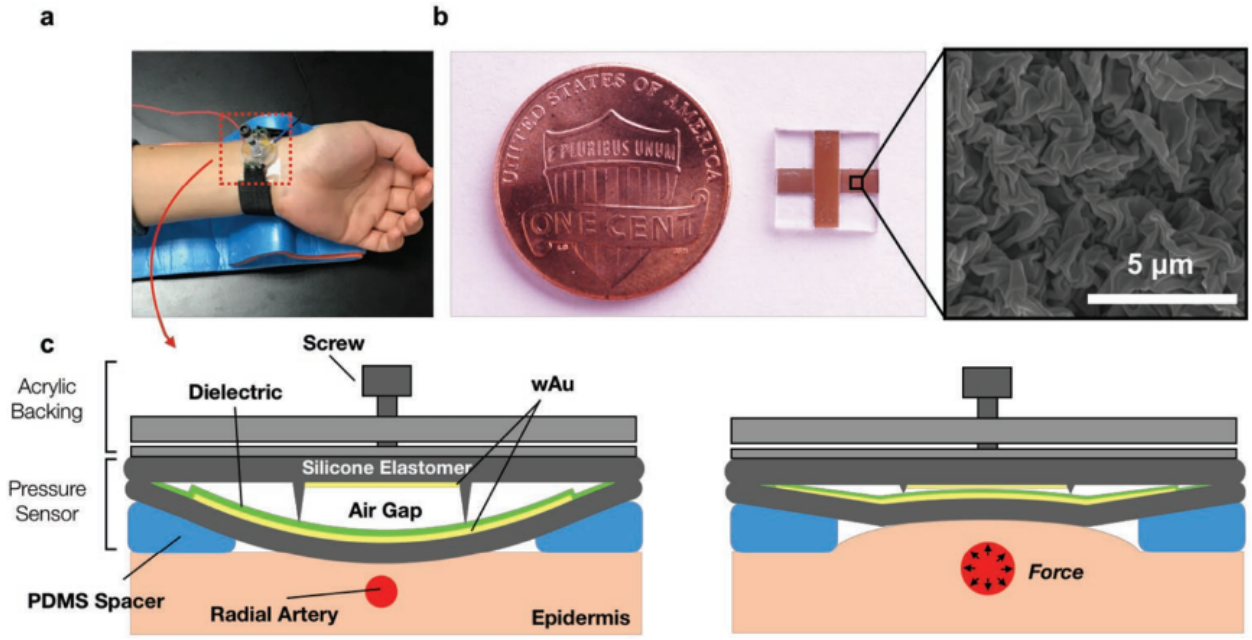

Figure 2.1. a) Image of how the pressure sensor is attached to the wrist. Photograph image of the parallel wAu electrodes. **b)** Photographic image of a capacitive pressure sensor and a scanning electron microscope (SEM) image of the wAu. **c)** Schematic illustration of the pressure sensor when placed on the wrist above the radial artery. On the right, the pressure sensor is deformed as blood pulses through the radial artery. A screw is used to add incremental pressure to applanate the radial artery.

This enables continuous arterial pulse pressure measurements with enough sensitivity over a large dynamic range and fast response times of less than 10 ms to capture the details of the pulse pressure waveform (**Figure 2.2**).

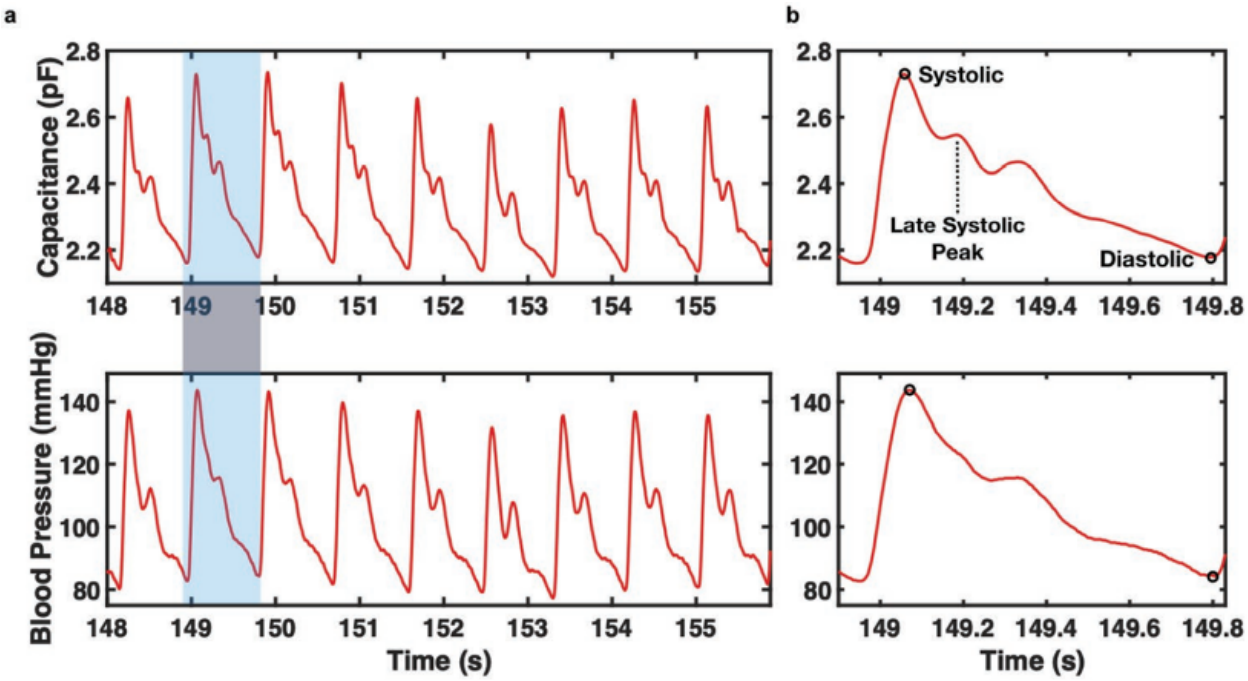

Figure 2.2. a) Example of arterial pulse waveforms measured by the capacitive pressure sensor (top row) and the Clearsight™ device (bottom row). **b)** Inset of one pulse waveform indicating cardiovascular features.

To assess the accuracy of these soft capacitive pressure sensors in continuous measurements of beat-to-beat BP, two FDA-approved NIBP monitoring devices were used as references. In the following sections of this chapter, we demonstrate the correlation between pressure sensors and two references with different breathing maneuvers.

Chapter 2.1: Comparison between the pressure sensor and ClearSight™ with alternative deep and normal breathing

2.1.1 Experimental setup for NIBP

To demonstrate beat-to-beat BP monitoring, we applied the soft capacitive pressure sensors to healthy subjects under approval from the Institutional Review Board of the University of California (IRB no.2016-2924). One soft capacitive pressure was tested on a total of seven subjects to demonstrate robustness. Two additional soft capacitive sensors were tested on Subject 1 to demonstrate reproducibility. The pressure sensor was attached to the wrist over the radial artery. Afterward, the subjects were told to keep their palm facing up and slightly hyperextended to help expose the radial artery on the surface of the skin. Subjects were sitting up with the pressure sensor close to heart level during these measurements. No allergic reactions or pain was reported by the subjects tested. For arterial pulse measurements, the pressure sensor was mounted onto an acrylic backing with a Velcro strap. A screw was attached to the acrylic backing such that the acrylic backing can apply incremental pressure to applanate the radial artery. The incremental pressure increased the baseline capacitance of the capacitive pressure sensor. The schematic illustration for the pressure sensor device can be seen in **Figure 2.1**. Medical tape, Tegaderm (3M Health Care) was also attached to the wrist to improve contact between the pressure sensor and the human skin. Lastly, a polydimethylsiloxane (PDMS) spacer (250 μm) was also used between the pressure sensor and the epidermis to further compress the tissue and amplify the radial arterial pulse. As BP increases in the radial

artery, the radial artery expands deforming the surrounding tissue, subsequently deforming the pressure sensor as seen in **Figure 2.1.c**. This pressure can be related to arterial BP as long as the contact between the pressure sensor and the body is consistently maintained.

To evaluate the capacitive pressure sensor's ability to measure beat-to-beat BP, the pressure sensor was compared against an FDA approved finger volume clamp device, ClearSight™. The ClearSight™ was attached to the right index finger of the subject. Measurements were taken simultaneously where the pressure sensor measured the pressure exerted by the radial artery and the ClearSight™ measured brachial arterial pressure. An example of the radial arterial pulse waveforms measured from the pressure sensor and the ClearSight™ is presented in **Figure 2.3.a**. As seen in Figure **2.3.b**, the quick response time and pressure sensitivity allowed for detection of the unique features in the radial arterial pulse waveform including the late systolic peak, which is not easily discernible in the ClearSight™ signal. The parameters that were investigated included systolic (SBP), diastolic (DBP), and mean arterial pressures (MAP). These parameters are the most common when evaluating a person's cardiovascular health. The SBP is the BP against the arterial walls when the heart has contracted, the DBP is the BP against the arterial walls when the heart has relaxed, and the MAP is the average pressure throughout one cardiac cycle and can be calculated using **Equation 2-1**[36]

$$MAP = DBP + \frac{1}{3}PP \tag{2-1}$$

where PP is the pulse pressure, which is equal to SBP minus DBP.

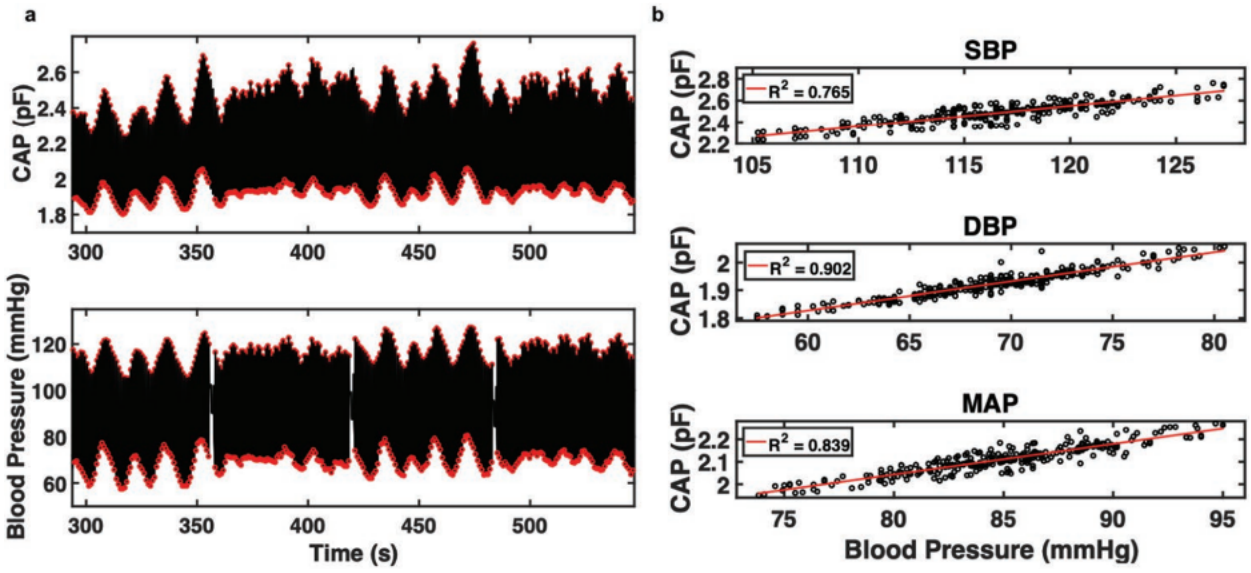

Figure 2.3. a) Example of the four 70-beat sections from Subject 1 that were used to compare between the capacitive pressure sensor and the ClearSight™. Arterial pulse waveforms are shown in black and highlighted in red indicate the SBP and DBP. **b)** Linear regression analysis of SBP, DBP, and MAP between the pressure sensor and the ClearSight™.

2.1.2 Beat-to-beat BP data analysis

When the ClearSight™ begins taking measurements, the ClearSight™ measures 10 cardiac cycles before a calibration step begins. After self-evaluation in accuracy, the ClearSight™ then measures 20 cardiac cycles and repeats the calibration step. The ClearSight™ will continue to measure additional cardiac cycles until it has reached 70 cardiac cycles at which the ClearSight™ is considered to be the most accurate and precise in measuring BP. These epoch regions were where the capacitive pressure sensors were compared against the ClearSight™. In addition, subjects were asked to alternate between breathing deeply and normally after each subsequent 70-beat section, respectively. By breathing deeply, it is possible to increase BP due to slight heart compression from lung expansion.[37] Subjects were asked to breathe deeply to assess the soft capacitive pressure sensor's ability to track larger changes in BP. **Figure 2.3.a,b** illustrates the data collected for

one subject. The remaining subject data can be seen in **Tables 2.1-2.3**. In **Figure 2.3.a**, qualitative analysis shows that the two devices measured similar trends in BP. This is apparent during the deep breathing sections where low frequency BP changes are reflected in both the pressure sensor and ClearSight™. The SBP, DBP, and MAP were subsequently plotted against each other and analyzed using linear regression, as seen in **Figure 2.3.b**. The goodness of fit between the pressure sensor and ClearSight™ device showed strong correlation with $R^2 = 0.765$ for SBP, $R^2 = 0.902$ for DBP, and $R^2 = 0.839$ for MAP. As stated earlier, previous studies show that the ClearSight™ device has difficulties in measuring accurate and precise SBP values, which could explain the lower R^2 between the pressure sensor and the ClearSight™.[22,38–40]

Table 2.1. R^2 of SBP in each 70-beat section and four sections combined for seven young healthy subjects.

Subject	Deep(1)	Normal(1)	Deep(2)	Normal(2)	Combined
1	0.741	0.601	0.815	0.915	0.765
2	0.824	0.769	0.827	0.639	0.754
3	0.520	0.798	0.854	0.767	0.662
4	0.650	0.815	0.720	0.886	0.578
5	0.755	0.235	0.317	0.469	0.554
6	0.429	0.500	0.866	0.722	0.477
7	0.733	0.743	0.619	0.289	0.536

Table 2.2. R^2 of DBP in each 70-beat section and four sections combined for seven young healthy subjects.

Subject	Deep(1)	Normal(1)	Deep(2)	Normal(2)	Combined
1	0.903	0.663	0.968	0.932	0.902
2	0.929	0.912	0.921	0.794	0.906
3	0.727	0.841	0.880	0.765	0.766
4	0.646	0.943	0.900	0.978	0.810
5	0.934	0.707	0.848	0.822	0.865
6	0.889	0.851	0.972	0.905	0.852
7	0.887	0.964	0.872	0.664	0.837

Table 2.3. R^2 of MAP in each 70-beat section and four section combined for seven young healthy subjects.

Subject	Deep(1)	Normal(1)	Deep(2)	Normal(2)	Combined
1	0.848	0.576	0.903	0.928	0.839
2	0.897	0.843	0.845	0.684	0.843
3	0.555	0.836	0.823	0.728	0.683
4	0.404	0.890	0.728	0.936	0.637
5	0.896	0.535	0.693	0.734	0.789
6	0.637	0.504	0.871	0.798	0.579
7	0.764	0.913	0.769	0.471	0.704

To further assess the accuracy and precision of the pressure sensor's ability to monitor beat-to-beat BP, the pressure sensor was calibrated to the ClearSight™ to generate a model for the pressure sensor and cross validated. To create the model, three consecutive cardiac cycles were first averaged together. After averaging, 75% of the data was randomly selected to generate a linear regression model for the pressure sensor. The remaining withheld dataset from the pressure sensor was converted to units of BP–millimeters of mercury (mmHg). An example of this calibration from one subject is shown in **Figure 2.4.a–c**.

Bland–Altman analysis was then used to assess the agreement in measurements of BP between the pressure sensor and ClearSight™.[41] Bland–Altman looks at the difference in

BPs that were measured at the same time plotted against the average of the BP measured at the same time. Larger differences would indicate larger disagreement between the two devices. As shown in **Figure 2.4.d**, all seven subjects are compiled into one Bland–Altman plot including data sets from Subject 1 that was tested with two additional sensors. Mean bias and standard deviation calculated was −0.054 ± 2.09 mmHg. The ISO 81060–2 set by the AAMI has indicated that a NIBP is deemed interchangeable with an arterial catheter if mean biases are less than 5 mmHg with standard deviations of less than 8 mmHg.[22,42] The Bland– Altman analysis here shows that the mean bias and standard deviation are well below the requirements indicated by the ISO standards. This suggests that the capacitive pressure sensor is highly accurate and precise in measuring BP when calibrated to the ClearSight™ device. However, it is important to note that the ISO standards require that NIBP devices be directly compared against an arterial catheter and not against other NIBP devices. Future studies are therefore required to compare against the gold standard, arterial catheter. The soft capacitive pressure sensors show strong evidence that radial tonometry is a feasible method for beat-to-beat NIBP monitoring. The capabilities to accurately monitor a wide range of pressures are enabled by the electromechanical properties of the pressure sensor. In addition, the quick response times of the capacitive pressure sensors allowed for detecting the radial arterial pulse waveform with high fidelity allowing for accurate and precise measurements of BP.

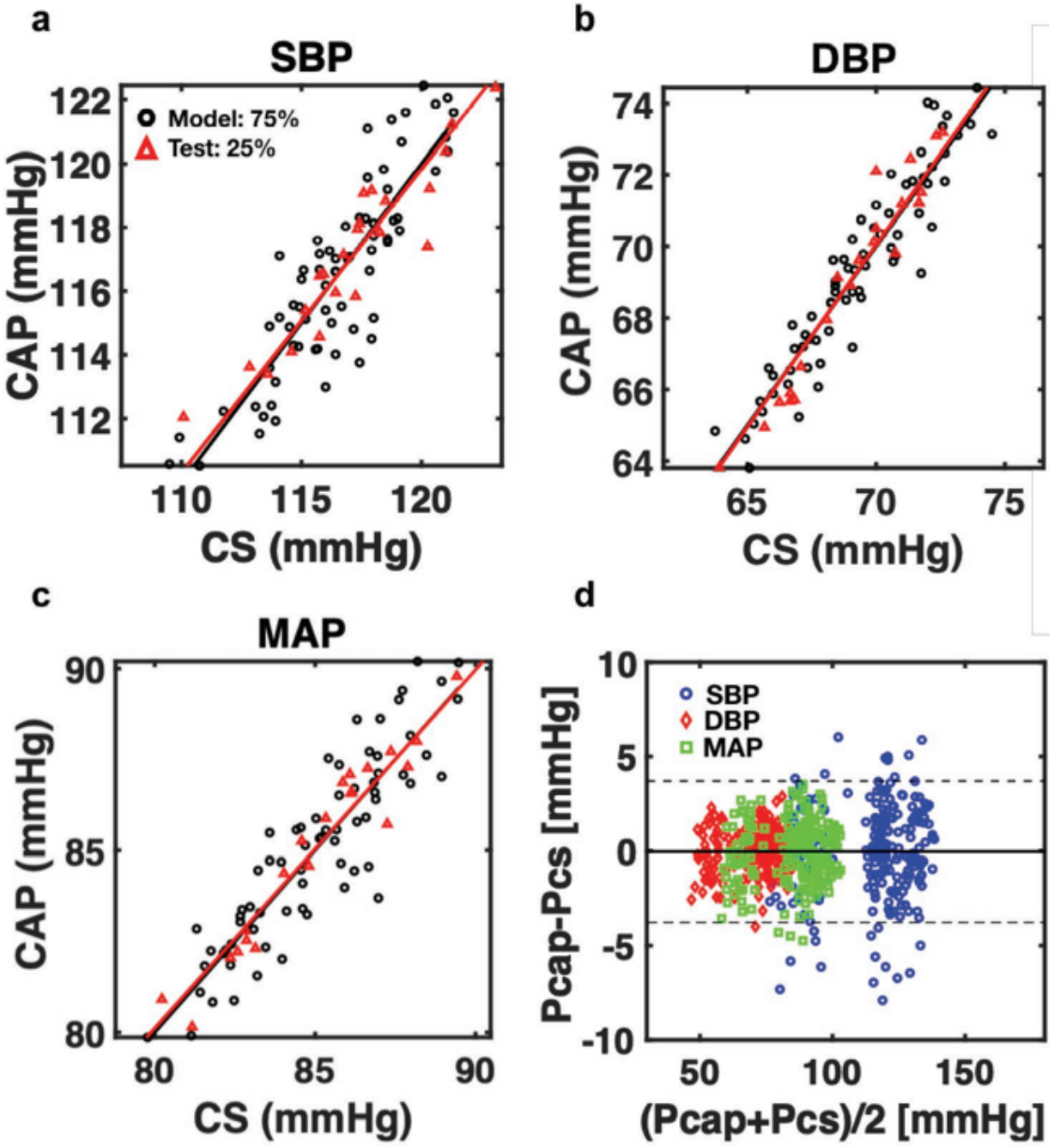

Figure 2.4. Example of pressure sensor calibration model from Subject 1 for **a)** SBP **b)** DBP, and **c)** MAP. **d)** Bland–Altman plot for all subjects combined. Data includes the different sensors used on Subject 1 for a total of nine independent tests. Dashed lines indicate two standard deviations and solid indicates mean bias.

Chapter 2.2: Comparison between the pressure sensor, ClearSight™, and CNAP®

2.2.1 Experimental setup for NIBP

To understand the performance of the pressure sensors comparing against FDA approved NIBP monitors, beat-to-beat BP measurements were collected using soft capacitive pressure sensor and two FDA approved NIBP monitors, ClearSight™ and CNAP®, simultaneously. The pressure sensor was set up following same instruction in chapter 2.1.1. ClearSight™ and CNAP® were placed on the index and middle fingers of opposite hands. Lastly, a wireless upper arm BP monitor, Evolv® (Omron Corporation, Kyoto, Japan) was placed on the upper arm as the initial BP reference for the NIBP devices.

A total of three healthy young participants were recruited. They were asked to sit quietly before and during the test. The NIBP systems acquired signals at the same time while the participants resting in a sitting position with normal breathing.

2.2.2 Beat-to-beat BP data analysis

Similar to chapter 2.1.2., the correlation of beat-to-beat SBP and DBP of every two NIBP systems were assessed using the goodness of fit in linear regression (**Figure 2.5**). **Table 2.4** shows the R^2 values in SBP, DBP, and combined results of three participants.

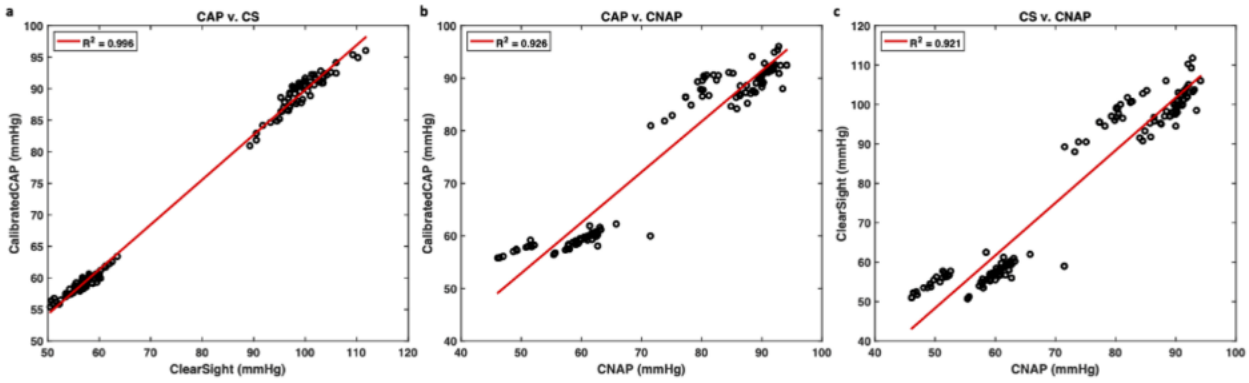

Figure 2.5. Linear regression analysis of a combination of SBP and DBP between two continuous NIBP devices from Subject 1. The black circles and the red line represent the beat-to-beat SBP and DBP values and the linear regression line of the two systems, respectively. The linear regression analysis between two systems: a) the pressure sensor and the ClearSight™ system, b) the pressure sensor and CNAP®, and c) the ClearSight™ system and CNAP®.

Table 2.4. The R^2 values of SBP, DBP, and the combination of SBP and DBP between two continuous NIBP systems from each participant.

	CAP vs. CS			CAP vs. CNAP			CS vs. CNAP		
Subject No.	SBP	DBP	Combined	SBP	DBP	Combined	SBP	DBP	Combined
1	0.864	0.893	0.996	0.506	0.652	0.926	0.464	0.517	0.921
2	0.568	0.422	0.969	0.762	0.829	0.982	0.679	0.606	0.985
3	0.934	0.905	0.995	0.257	0.003	0.875	0.259	0.011	0.853

CAP: the soft capacitive pressure sensor from Khine Lab;
CS: ClearSight device from Edwards Lifesciences;
CNAP: noninvasive blood pressure amplifier from BIOPAC Systems, Inc.

CHAPTER 3: Clinical validation of a soft wireless continuous blood pressure sensor during surgery

Portions of this chapter appears in the journal Frontiers in Digital Health.[43]

With the confidence that the soft capacitive pressure sensors can be used as NIBP monitors after certain calibration methodologies, we further compared the sensors against an arterial catheter during surgery as a clinical validation.

Chapter 3.1: Abstract

We test a new wireless soft capacitance sensor (CAP) based on applanation tonometry at the radial and dorsalis pedis arteries against the gold standard, invasive A-Line, for continuous beat-to-beat BP measurements in the Operating Room (OR) during surgical procedures under anesthesia in 17 subjects with the mean age and body mass index (BMI) of 57. 35 ± 18.72 years and 27.36 ± 4.20 kg/m^2, respectively. We have identified several parameters to monitor in order to compare how well the CAP sensor tracks the entire hemodynamic waveform as compared to the A-Line. This includes waveform similarity, HR, absolute SBP, DBP, and temporal response to a vasopressor. Overall, the CAP sensor shows good correlations with A-Line with respect to hemodynamic shape ($r > 0.89$), HR (mean bias = 0.0006; SD = 0.17), absolute SBP, and DBP in a line of best fit (slope = 0.98 in SBP; 1.08 in DBP) and the mean bias derived from Bland-Altman method to be 1.92 (SD = 12.55) in SBP and 2.38 (SD = 12.19) in DBP across body habitus and age in OR patients under general anesthesia. While we do observe drifts in the system, we still obtain decent

correlations with respect to the A-Line as evidenced by excellent linear fit and low mean bias across patients. When we post-process using a different calibration method to account for the drift, the mean bias and SD improve dramatically to −1.85 and 7.19 DBP as well as 1.43 and 7.43 SBP, respectively, indicating a promising potential for improvement when we integrate strategies to account for movement identified by our integrated accelerometer data.

Chapter 3.2: Introduction

BP is one of the core physiological measurements of interest in virtually all healthcare contexts as it provides insight into a patient's cardiac function, volume status, organ perfusion, and overall hemodynamic stability. It is typically monitored using a noninvasive sphygmomanometer, otherwise known as the BP cuff, and in higher-risk surgery may be monitored using an invasive A-Line. The A-Line is considered the gold standard in capturing beat-to-beat BP values to detect immediate fluctuations. This requires the insertion of a catheter into an artery, typically the radial or dorsalis pedis arteries. Because A-Lines are invasive, they are associated with an increased risk of complications including infection, thrombosis, and embolization.[18,20,44] Clinicians may also experience difficulty cannulating the arteries so clinical expertise is required for proper insertion.[45] As a result, 30% or less of patients in the OR or Intensive Care Unit (ICU) receive A-Lines.[44] Instead, the overwhelming majority of patients even in hospital settings are only monitored intermittently using the BP cuff, which inherently lacks the temporal resolution to detect real-time fluctuations in hemodynamically labile patients. Moreover,

such intermittent measurements have been observed to under or overestimate BP readings when compared with the A-Line.[46,47] In fact, a recent study has shown that BP cuff measurements are inaccurate (within ISO guidelines) up to almost 50% of the time.[48] Since BP is a dynamic physiological parameter that changes constantly over time, continuous NIBP monitoring would reveal important hemodynamic information in real-time that is currently delayed by the intermittent BP cuff readings. This is especially important when labile BP warrants close monitoring–such as in the Emergency Room (ER), OR, or ICU settings. Furthermore, as healthcare moves towards digital health, options for remote continuous BP monitoring (e.g., in ambulatory settings) would be incredibly useful in the management of hypertension, which affects roughly half of all American adults, as well as other medical conditions with vascular underpinnings.[49] This is particularly important for personalized medicine—for example, to remotely monitor how patients respond to vasoactive pharmaceuticals. For these reasons, noninvasive methods for continuous BP monitoring, or NIBP, is an area of continued interest. Existing NIBP methods to capture continuous BP include optical techniques; derivations based on other vital sign measurements such as PTT; ultrasound technology; and tonometry. Concerning optical techniques, ClearSight™ and CNAP® are both FDA-approved infrared PPG devices that use the finger cuff volume clamp method. These devices are used preliminarily in the ICU or post-operative patients in the hospital because patients must remain stationary, the method is uncomfortable (a finger cuff repeatedly inflates), and they do not work well on patients with peripheral vascular disease or administration of high-dose vasopressors.[14,50,51]

More recently, cuffless PPGs have been used to indirectly estimate BP using PTT, which is the time it takes for a BP waveform to propagate from one location to another. As such, estimates depend on physiological conditions and have been shown to be inaccurate in certain populations.[52,53] More recently, conformal ultrasound patches can monitor BP waveforms. However, they are yet to be wireless and require connection to a power source and a benchtop machine to display the data.[54,55] Finally, the last technology category, tonometry involves applying force over the artery to measure the pulsatile displacement of the vessel wall under applanation. Typically, the pressure transducers in this class have been rigid, bulky, and shown to be inaccurate in obese and cardiac patients.[56,57] We have previously demonstrated the accuracy of a CAP sensor based on applanation tonometry for continuous non-invasive measurement of BP compared to the FDA-approved NIBP monitor ClearSight™ in a small cohort of healthy, young individuals.[15] For clinical validation, however, it is important to compare against the gold standard in a clinical setting across body habitus and age. In this paper, we demonstrate calibration and comparison of pulse waveforms from the CAP sensor to A-Line measurements taken simultaneously in the intraoperative setting across 17 patients ranging in age from 24 to 79 years and importantly, with BMI from 24 (normal) to 34 (obese) kg/m^2. Importantly, to do our comparison, we needed to develop an objective signal processing framework to analyze large data sets of different length scales with real-world noise and motion artifacts. Moreover, to make sense of the data, we needed to determine strategies to compare key parameters.

Chapter 3.3: Methods

BP data were acquired invasively and non-invasively using an A-Line and a CAP sensor, respectively. Surgical patients aged 18 to 99 years under general anesthesia in the OR setting who needed an A-Line placed as a standard of care were recruited at University of California Irvine Health between June 2020 and March 2021. Exclusion criteria were patients aged <18 years, refusal, or inability to give informed consent. All subjects gave informed consent for the study which was approved by the Institutional Review Board of the University of California (IRB no. 2019-5251).

3.3.1 Measuring devices and systems

This study simultaneously employed two continuous BP measurement systems (**Figure 3.1.a**). The A-Line was inserted into the radial artery and connected to a pressure transducer (ICU Medical Transpace© IV Monitoring Kit (60''), REF no. 42584-05) and displayed on a monitoring system (GE Patient Data Module & Monitoring system, General Electric, Boston, MA). The A-Line signal was then captured at an average sampling rate of 100 Hz using a DAQ board (National Instruments cDAQ-9171 with NI 9234) with a custom application written in C#.

The non-invasive system comprises a CAP sensor[15] and an EcoBP[58], an eco-friendly dual-channel custom data acquisition board that includes an inertial measurement unit (IMU). The CAP sensor was placed at the radial artery (or in two cases, the dorsalis pedis

artery) for continuous arterial pressure measurement. The CAP signal was captured at a sampling rate of 90 Hz in single-channel mode and 45 Hz in dual-channel mode.

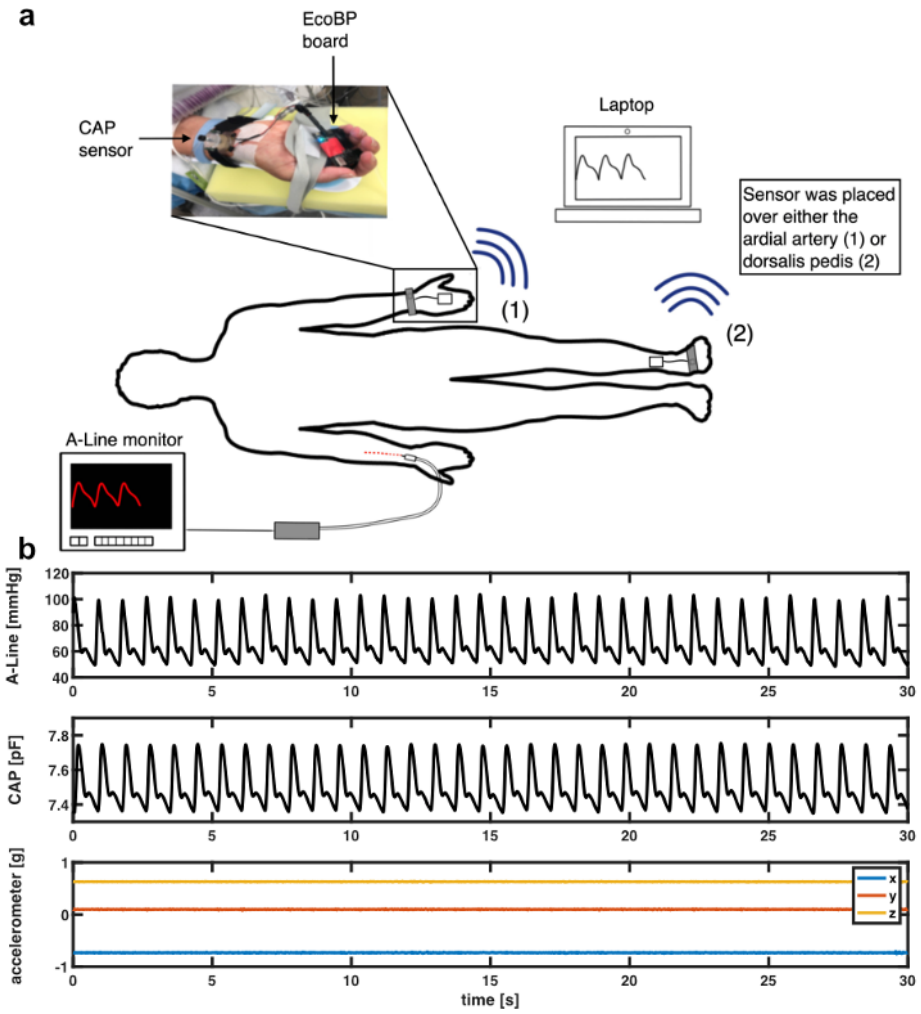

Figure 3.1. **a)** Measurement setup in the OR. An A-Line was inserted in the radial artery. The CAP system was placed either on the radial artery or the dorsalis pedis artery depending on the procedure. **b)** An example of a 30-s segment raw signal acquired from A-Line, the CAP sensor, and the accelerometer data that was used to compare waveform similarity, HR, and BP.

3.3.2 Experimental procedure

The A-Line was inserted into the radial artery on either arm and calibrated per hospital protocol. A BP cuff (CRITIKON™ SOFT-CUF™REF SFT-A2-2A, GE Healthcare,

Chicago, IL) was also placed on either arm for periodic measurements. The CAP sensor was placed over the radial artery, on the arm without the A-Line, and stabilized with slight pressure via mechanical fixation using Velcro strap, sea-band (Sea-Band Ltd., Hinckley, Leicestershire, England), or Prelude Sync Radial Compression Device (Merit Medical Systems, Inc.). In cases where the radial artery was not readily available for placement, the dorsalis pedis artery was used (**Figure 3.1**). The EcoBP board was taped down onto the skin using Transpore tape (3M, Minnesota, USA).

After anesthesia induction, measurements were continuously collected from both CAP (non-invasive) and A-Line (invasive) systems by the anesthesiologist for a minimum of 15 min during the operation. The timing of administration of all intraoperative vasoactive medications was recorded in the electronic medical records (EMR).

3.3.3 Data extraction and quality assessment

The collected data was post-processed using Matlab (R2019b, The MathWorks, Natick, Massachusetts, USA). The raw signals were first spline interpolated to 500 Hz. To synchronize the signals recorded on different systems, cross-correlation was applied to the signal obtained by differentiating the discrete sequence of systolic peaks. After signal synchronization, clearly identified artifacts from invasive and non-invasive measurements were cleaned out. The A-Line data was visually screened by the authors for errors; excessively noisy sections defined by a sudden change of pressure >30 mmHg within two beats were removed. On the other hand, artifacts in the CAP signals were removed based on the movement data captured by the IMU. A 2.5-scaled median absolute deviation (MAD)

filter was applied to accelerometer data on each of the 3 axes to detect outliers due to sudden and immoderate movement (**Figure 3.2.a**). A 100- points (0.2 s) moving window was then applied and windows with at least 10% of data categorized as outliers were sliced out (**Figure 3.2.b**). In addition to specific artifact removal techniques separately applied to A-Line and CAP signals, the intermittent BP cuff occlusions affected either A-Line or CAP measurements. Consequently, the affected data sections were cleaned out. It is worth noting that for consistency, any artifact-ridden data section in A-Line was also sliced out of CAP signal and vice-versa. After the removal of segments with excessive artifacts, the remaining signals were then considered valid data for further analysis.

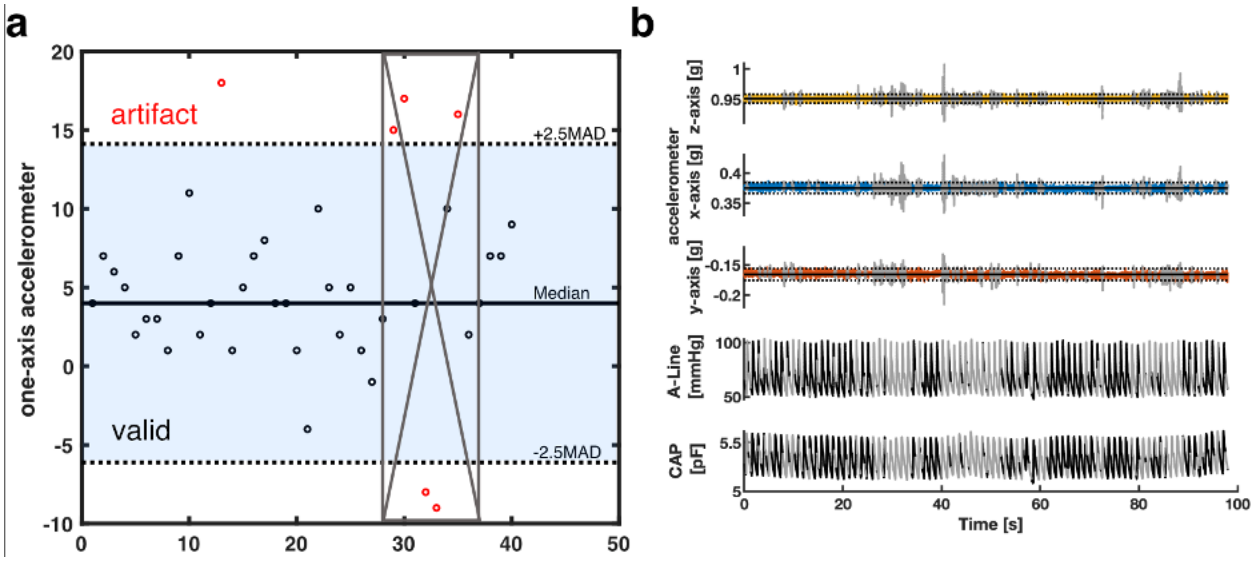

Figure 3.2. The artifact removal procedure using accelerometer data **a)** Illustration of MAD filter and moving window. The horizontal solid line is the median value of the accelerometer dataset. The dotted lines are the 2.5-scaled MAD. Black circles represent the data within 2.5-scaled MAD. Red circles are considered outliers. The gray crossed area represents the invalid segment after a 50 percent threshold moving window with a window size of 8. **b)** A representative segment showing how the data was filtered with a MAD filter and the moving window. The top three rows are the 3-axis of the accelerometer data. The horizontal solid line represents the

median in each axis. The dotted lines are the 2.5-scaled MAD of each axis. The bottom two rows represent the corresponding A-Line and the CAP sensor data. The signal section colored gray and defined by the vertical lines was categorized as having excessive artifacts from the accelerometer data and thus removed.

3.3.4 Waveform similarity analysis

The diastolic and systolic pressure values and timestamps of each valid segment of data were identified for waveform analysis. A complete waveform was defined as the signal data bounded by two consecutive diastolic pressure values.

To analyze waveform shape similarity, corresponding A-Line and CAP sensor waveforms were normalized between 0 and 1. For each waveform, 0 was set as the average of the starting and ending diastolic pressure values, and 1 as the waveform maximum (systolic pressure value). A 0.1 threshold value was then applied to avoid false detection of minima (diastolic pressure).

3.3.5 Heart rate monitoring

HR is the reciprocal of the beat-to-beat time interval of the continuous BP signal (**Equation 3-1**). The systolic intervals were obtained as the time interval from one systolic pressure value to the subsequent one as shown in **Figure 3.3**.

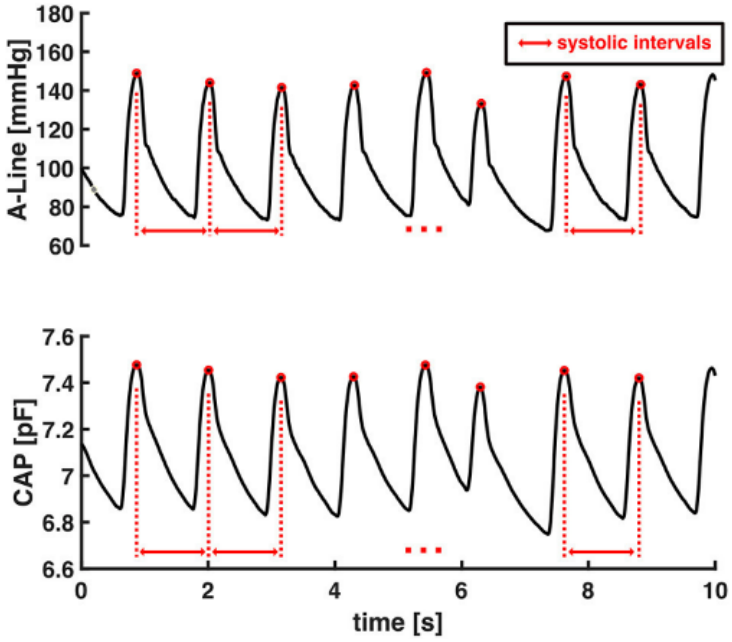

Figure 3.3. An example of the interval of two consecutive systolic pressures used to calculate HR.

The HRs were calculated as the reciprocal of these systolic intervals. The accuracy of HR estimation from capacitive pressure signal was evaluated by computing average HR values in each 30- s data window from valid segments of CAP sensor and then comparing against A-Line's. Each valid signal was sliced into 30- s non-overlapping windows starting from the beginning of the signal and any remaining data that was <30-s was excluded from HR computation.

$$Heart\ rate\ [bpm] = \frac{1}{beat-to-beat\ interval\ [min]} \quad (3\text{-}1)$$

3.3.6 Blood pressure comparison

Using valid data segments from A-Line and CAP sensor measurements, the CAP sensor's ability to accurately infer absolute BP is assessed.

Given that the CAP sensor's raw measurements are captured as capacitance values in picofarad (pF) and the A-Line's as absolute pressure in mmHg, a conversion from the CAP sensor's capacitance to absolute pressure in mmHg is needed to accurately assess the CAP sensor against A-Line. In this regard, we propose a calibration algorithm.

The initial step in the calibration process is the extraction of systolic and diastolic pressure signals from the raw A-Line and CAP sensor measurements. A 5-points median filter was applied to the extracted signals to smooth out detected false values. The filtered systolic and diastolic pressure signals were then split into individual 60-s segments for use in subsequent calibration steps. In a normal resting condition, a 60-s segment should contain 60–100 beats. The choice of 60-s as segment length is based on ClearSight™'s use of 70 beats between re-calibration.[59]

The calibration algorithm took the average values of the first three beats in systolic and diastolic pressure every 60-s epoch. Sixty seconds was chosen for re-calibration periodicity as this is standard practice in ClearSight™, a commercially available continuous NIBP device. A linear regression model was then created as the relationship between pressure measured in pF and mmHg. The remaining systolic and diastolic capacitance pressure values in the 60-s segment were then converted to the units of BP (mmHg). An example of the calibration algorithm can be found in **Figure 3.4**.

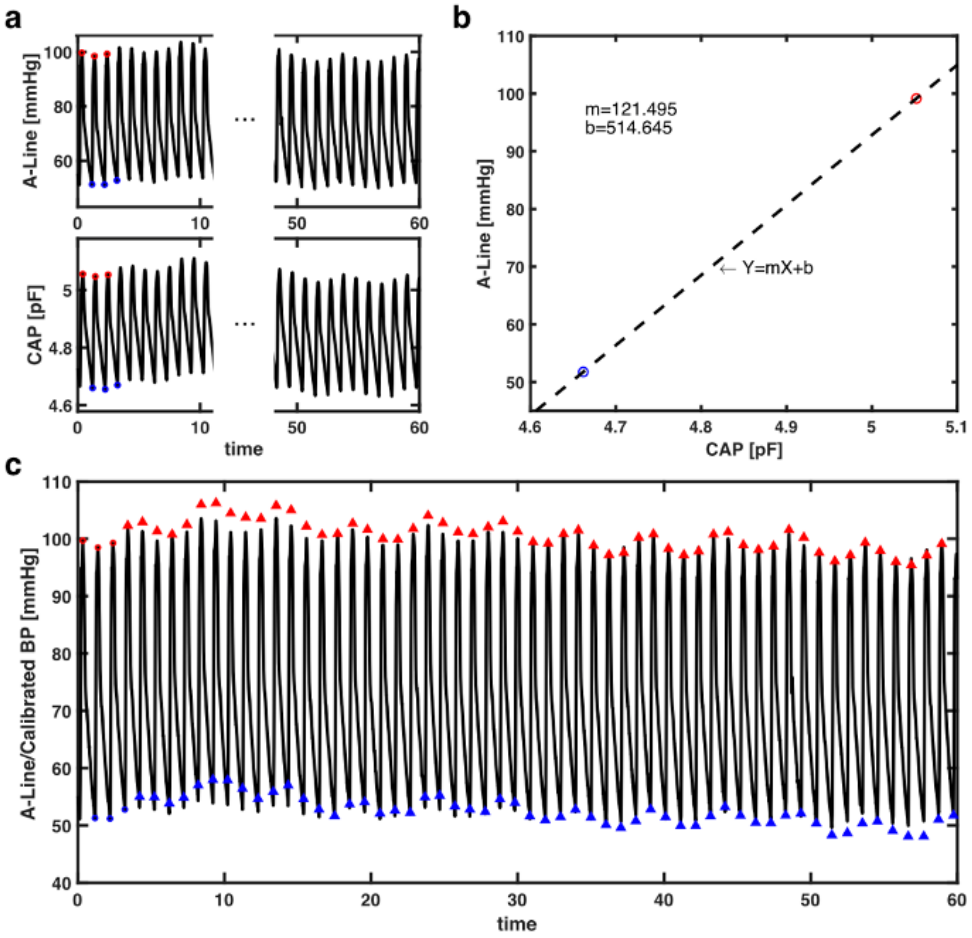

Figure 3.4. The presented calibration algorithm. a) An example of a 60-s epoch raw signal acquired from A-Line and the CAP sensor. The red and blue circles are first three systolic and diastolic pressure values extracted for calibration from each signal, respectively. b) Linear regression that models the relationship between the averaged systolic (red) and diastolic (blue) pressure values of A-Line and the CAP sensor from the first three beats. The dashed line is a linear regression line that forms the equation with m the slope and b the intercept. c) The raw 60-s signal of A-Line, first three beats of SBP and DBP (red/blue circles), and the SBP and DBP values (red/blue triangles) calibrated from the CAP signal using the presented calibration algorithm.

3.3.7 Statistics

To assess the CAP sensor's ability in comparison to A-Line in an OR setting, several statistical methods were performed. Pearson correlation coefficient gives the linear correlation between features acquired from A-Line and the CAP sensor. Here, Pearson's r

was computed to quantify the similarity between corresponding A-Line and CAP sensor normalized waveforms after aligning the two by their maxima (normalized systolic pressures) and how well the CAP sensor tracked BP compared to A-Line in vasoactive-drug-administered incidents. Moreover, the mean bias, SD, and 95% limits of agreement (estimated as the SD of the differences × 1.96) were calculated to understand the agreement between two methods by Bland-Altman method of paired measurements.[60,61]

Mean HR in 30-s epochs and SBP and DBP in 60-s epochs derived from A-Line and CAP measurements were evaluated by this method. Lastly, the slope and R^2-value of a simple linear fit were presented to evaluate the accuracy of beat-to-beat DBP and SBP using the proposed calibration algorithm.

Chapter 3.4: Results

We have identified several parameters to monitor in order to compare how well the CAP sensor tracks continuous BP as compared to the A-Line. This includes waveform similarity, HR, absolute SBP and DBP, and temporal response to a vasopressor.

3.4.1 Participants

A total of 32 patients undergoing surgery requiring an A-Line placed were recruited during the study period, seven of whom were excluded due to the failure of data collection (data not recorded or data acquisition issues), five were excluded with obvious distortion in the measurements (artifacts or inaccurate sensor placement), and three others were excluded when the pulse signal from dorsalis pedis was affected by the intermittent

pneumatic compression (IPC) device placed on the legs during the entire measurement. Thereafter, 17 patients (six male) with a mean age of 57.35 ± 18.72 years and a mean BMI of 27.36 ± 4.20 kg/m2 were reported in the paper. Patients' demographics, the placement of CAP sensor, and the procedure are shown in **Table 3.1**. The post-processing method was used to remove obvious incorrect measurements and potential distortion affected by apparent artifacts. After removing artifacts as heretofore described, the mean and standard deviation of the total amount of data included across the 17 studies was 46 ± 21%.

Table 3.1. Patients' demographic, CAP placement, and procedure.

Subj. no	Age	Gender	BMI	Sensor placement	Procedure
1	24	F	24.0	Radial	Open abdominal
2	49	M	26.6	Dorsalis pedis	Neck dissection
3	74	M	34.0	Radial	Microvascular decompression
4	78	F	33.5	Radial	Laparoscopic abdominal
5	23	F	20.0	Radial	Right calf sarcoma resection
6	55	F	32.0	Radial	Open abdominal
7	62	M	30.7	Radial	Radical, cystoprostatectomy
8	79	F	25.0	Radial	Open abdominal
9	61	F	27.0	Radial	Whipple
10	64	F	29.0	Radial	Whipple
11	22	F	30.2	Radial	Hip
12	72	M	26.6	Radial	Open abdominal
13	52	F	23.0	Radial	Ankle
14	59	F	28.0	Dorsalis pedis	Mandible tumor removal
15	61	F	21.6	Radial	Whipple
16	61	M	23.0	Radial	Open abdominal
17	79	M	31.0	Radial	Open abdominal

3.4.2 Waveform similarity

All the full-beat waveforms were included to understand the similarity of hemodynamic waveforms from two sites of the subject's body. A total of 20,090 full-beat waveforms were analyzed, which included non-invasive pulse waveforms from the radial artery and dorsalis pedis artery, to compare against BP derived from A-Line. Pearson's r is applied to indicate the strength of similarity between the two curves. Due to the length difference of valid segments in each dataset, the results are presented as averaged r-values with the quantity of full-beat waveforms as listed in **Table 3.2**. It is shown that the hemodynamic waveforms acquired from two different locations, regardless of the invasiveness of the acquisition technique, of the same patient have a very strong linear relationship.[62] Besides, the two studies with averaged r lower than 0.9 (Subject 2 and Subject 14) were the only two studies having the pressure sensor placed on dorsalis pedis artery rather than the radial artery.

Table 3.2. Mean and standard deviation of Pearson correlation coefficient r across 17 subjects.

Subj. no	*N*	Mean	STD
1	343	0.9920	0.0041
2	281	0.8888	0.0339
3	593	0.9410	0.0238
4	861	0.9046	0.0198
5	537	0.9459	0.0315
6	533	0.9332	0.0948
7	1097	0.9739	0.0262
8	664	0.9362	0.0296
9	466	0.9310	0.0196
10	834	0.9818	0.0113
11	442	0.9732	0.0087
12	513	0.9854	0.0261
13	3,063	0.9807	0.0126
14	1,470	0.8983	0.0308
15	3,742	0.9473	0.0192
16	2,699	0.9277	0.0571
17	1,952	0.9839	0.0041

Values of each subject were calculated according to the number of valid waveforms (N). STD, standard deviation.

3.4.3 Heart rate monitoring

To assess the accuracy of heart rate detection across all the patients in the study, a total of 562 30-s valid segments for both A-Line and CAP were extracted and compared in the mean and standard deviation of HR. The mean bias and SD of mean HR in two measurements are 0.0006 and 0.1666 bpm, respectively. The 95% limits of agreement lie in the range of −0.3259 and 0.3272 bpm (**Figure 3.5**).

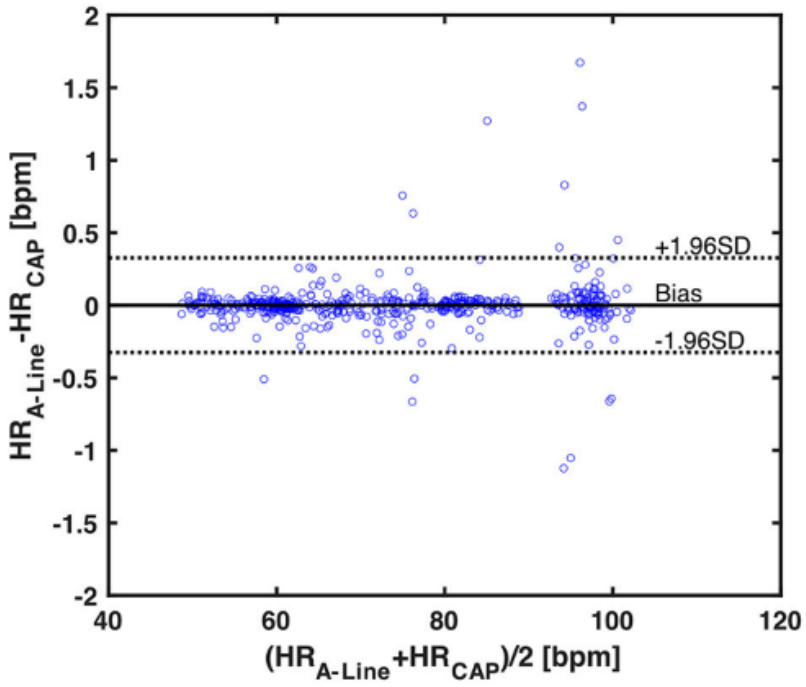

Figure 3.5. A Bland-Altman plot of 562 averaged heart rates calculated from 30-s valid segments across 17 patients. Each blue circle is one averaged HR data. The black horizontal solid and dotted lines represent the mean bias and the upper and lower 95% limits of agreement, respectively. The mean bias in differences is 0.0006, upper 95% limit is 0.3272, and lower 95% limit is −0.3259.

3.4.4 Blood pressure comparison

A total of 29,319 BP values (14,645 diastolic and 14,674 systolic) were obtained and compared from 209 60-s segments. The mean bias of overall DBP and SBP are 2.3842 (SD = 12.1908) and 1.9153 (SD = 12.5525), respectively. The limits of agreement in DBP are from −21.5098 to 26.2782 mmHg and for SBP from −22.6876 to 26.5182 mmHg (**Figures 3.6.a,b**). To understand the correlation of BP measurements within two systems, a best-fit line with a slope of 1.0047 was derived (**Figure 3.6.c**).

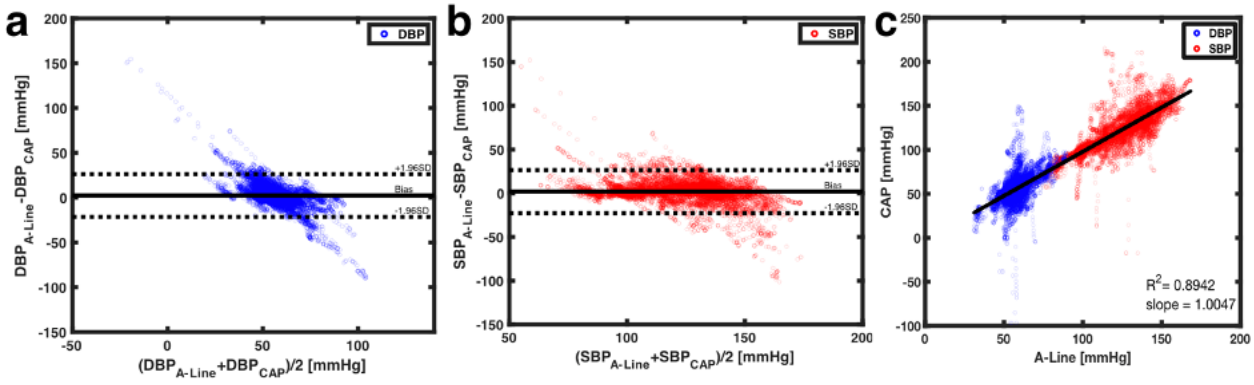

Figure 3.6. Beat-to-beat BP comparison using Bland-Altman method and linear regression. **a)** With 14,645 paired data points of DBP (blue circles), a mean bias of 2.3842 (solid black line) and an SD of 12.1908 were calculated. The dotted black lines are the upper (26.2782) and lower (−21.5098) 95% limits of agreement. On the other hand, **b)** 14,674 paired measurements of SBP (red circles) were compared. The mean bias of 1.9153 (horizontal black solid line) and an SD of 12.5525 were calculated. The 95% limits of agreement ranged from −22.6876 to 26.582. **c)** The CAP sensor was compared against the A-Line using a linear regression model over 29,319 data points from valid 60-s segments. A linear fit slope of 1.0047 shows the two measurements in good correlation.

The separated plots of SBP and DBP measured by A-Line and the CAP sensor can be seen in **Figure 3.7**. Lastly, we observed the BP change after the vasoactive drugs were administered. A total of 20 events were identified according to physician observation and the EMR across nine patients (no vasoactive drug administration was observed while the other eight patients were recorded). Three events were excluded due to movement artifacts caused by either the surgeon or the periodic BP cuff measurement. The mean duration of the 17 events was 55.4 (SD = 29.8) seconds. The Pearson's r of SBP between A-Line and CAP was 0.82 ± 0.28 (mean±SD). **Figure 3.8** shows a representative event in which both BP measured from A-Line and the CAP sensor increased 30 s after Ephedrine and Vasopressin

were administered. This is unlike sensors based on PPG which have difficulty tracking fast changes in BP.[63]

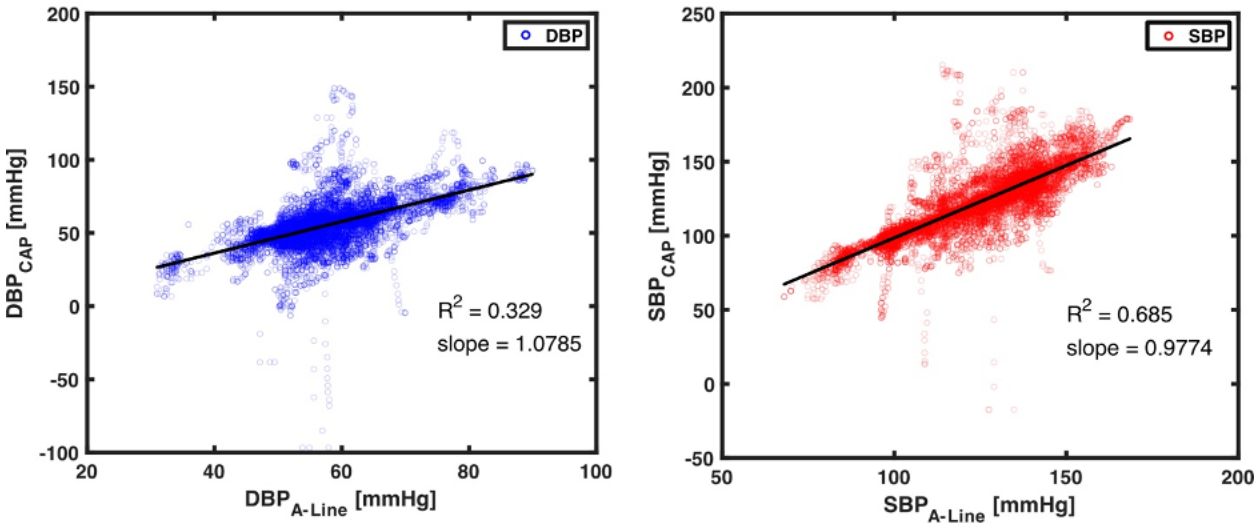

Figure 3.7. BP was measured by A-Line and the CAP sensor from valid 60-s segments using the proposed calibration method. a) A linear fit slope of 1.0785 and R2 of 0.329 were derived from 14, 645 DBP in blue circles. The black solid line across the blue circle is the best linear fit line. b) A linear fit slope of 0.9774 and R2 of 0.685 were derived from 14,674 SBP in red circles. The black solid line across the red circle is the best linear fit line.

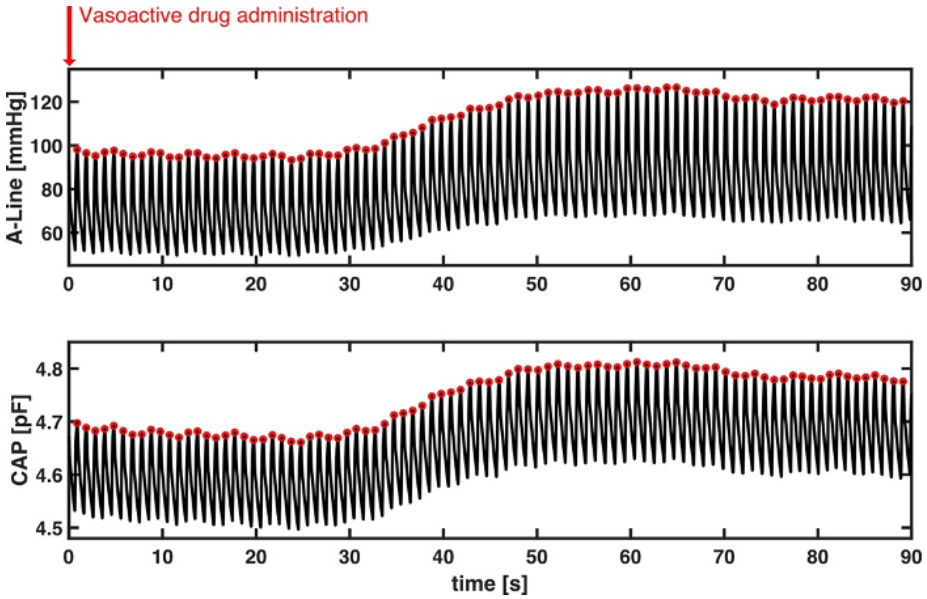

Figure 3.8. A representative section of the temporal response to vasoactive drug administration in both A-Line and CAP signals. Without motion artifacts, BP increased about 30 s simultaneously after Ephedrine and Vasopressin were administered. Systolic peak values of both A-Line and CAP signals were detected as the red circles. The Pearson correlation is 0.9973.

Chapter 3.5: Discussion

The major finding of the study is that the CAP sensor can noninvasively track BP across different body types and ages in an OR setting under general anesthesia. In particular, the study showed the sensor's capability of capturing hemodynamic waveforms from different arterial sites with high fidelity compared to the A-Line. Additionally, we found a good correlation in HR monitoring. Concerning beat-to-beat BP monitoring, we showed a low mean bias of both SBP and DBP.

3.5.1 Clinical application

At present, we have demonstrated an ability to accurately track BP with high confidence. While the present performance may be improved over time and is not a replacement for continuous arterial monitoring, there would nevertheless be clinical utility even with the present sensor as an adjunct to noninvasive monitoring (which is used universally during surgery). The NIBP monitoring could be used as it currently is, and the CAP sensor recalibrated with each cycling of the noninvasive cuff. Meanwhile, the CAP sensor would provide continuous monitoring in the periods between cuff cycles, catching hypotension faster and allowing for more rapid treatment, as well as allowing for more rapid assessment of other interventions like narcotics or anti-hypertensives.

3.5.2 Subject inclusion

Fifteen out of 32 datasets had been excluded from the study for the following reasons: failure of data collection, obvious distortion (in the A-Line data or from obvious misplacement of the CAP), and the simultaneous use of the IPC device. Improved instructions on applying the CAP sensor and/or improved applanation (strap) design should improve the ability to capture more datasets in the future.

3.5.3 Single-channel CAP sensor

As previously mentioned, 17 studies had been done either using a single or dual-channel CAP sensor. For the dual-channel CAP sensor, the second channel may be useful as a neighbor reference of the main arterial pressure signal. However, we have not yet investigated the benefits of dual-channel acquisitions and as a result, only one capacitance reading is included for all the data analysis in the study. We believe a multi-channel CAP sensor will greatly improve BP monitoring by eliminating the need for frequent recalibrations.

3.5.4 Artifact detection and quality assessment

There are a number of confounding factors inherent in any continuous physiological monitoring. This study was done in an OR setting to investigate the validity of the CAP sensor for a specific reason: we can account for and eliminate many of these variables. For instance, we have the BMI of every patient and whether they have hypertension via EMR. We found no correlation between BMI or hypertension and signal accuracy. The other

major confounding factor is movement artifact. From the development of the CAP sensor, it was found to have a low tolerance to movements. Compared to the previous study published using the CAP sensor in a relatively controlled subject group, this study was done in a real clinical setting where the measurement could be affected by multiple challenges. One obvious difference of BP measurement with noninvasive technology is that the data is obtained outside the subject's body. With different body sizes and ages of a patient, the tissue layer between the CAP sensor and the artery may create artifacts that directly influence the pressure measurement. For instance, the mechanical fixation on an elder patient with loose skin can be more challenging. Besides, the tightness and positioning of the wristband affected the signal quality. This also explains the reason why the study included multiple mechanical fixation ways. Furthermore, human-caused artifacts such as the surgeon's need to interact with the patient's body or the interference from electronic noises were inevitable in the OR. We chose to remove the artifacts of the A-Line signal by eye considering limited information. A similar data exclusion method has been previously used by several other groups.[56,64,65] In this case, it can be improved by including video recordings to have a better understanding of the artifact sources. On the other hand, the accelerometer data from the EcoBP was used to filter significant motion artifacts. The MAD filter is a robust measure of statistical dispersion. Although a 2- scaled MAD or 3-scaled MAD may serve a similar purpose of artifact removal, a 2.5-scaled MAD was chosen as an adequate threshold to separate the significant motion artifacts in the study while conserving a reasonable percentage of valid data. We also observed baseline drift in some

datasets from the CAP signal. In most cases, a downward drift occurred linearly or exponentially. The cause might be due to the movement or unknown factors. We expect a future study to resolve the issue. Despite the aforementioned challenges, it is clear that after the objective signal processing strategy outlined above, the CAP sensor showed a good correlation with A-Line during surgery and can provide a wealth of information about the hemodynamic waveform. In addition to the excellent slope value, the average mean bias and standard deviation across 15 patients were low.

3.5.5 Waveform similarity

Pearson correlation was used to evaluate the degree of the linear relationship between A-Line and CAP waveforms. Similar work had been previously done.[66] In this study, the focus for waveform similarity analysis was to compare full-beat wave shape. Consequently, the waveforms were normalized and aligned by the systolic pressure to avoid the time delay due to measuring from different sites of the body. A very strong correlation between A-Line and CAP sensor measurements was reported. Although not all waveforms from both signals perfectly match visually (**Figure 3.9**), it is in fact a characteristic of the peripheral arterial pressure waveform measured across different arterial sites. This waveform distortion effect is due to the individual physical characteristics of the arterial tree.[67,68] Additionally, the applanation tonometry waveforms were detected indirectly as the pulse signal propagated through the artery wall and the tissues. The CAP sensor not only can capture the components of the arterial pressure waveform (diastolic pressure, systolic pressure, upstroke of systole, dicrotic notch, etc.) but also potentially shows differences in the pulse pressure profile in the radial artery (upper extremity) and the dorsalis pedis

(lower extremity) as shown in **Figure 3.10**. This implies that the CAP sensor could acquire similar hemodynamic waveforms to the A-Line but non-invasively in an OR setting.

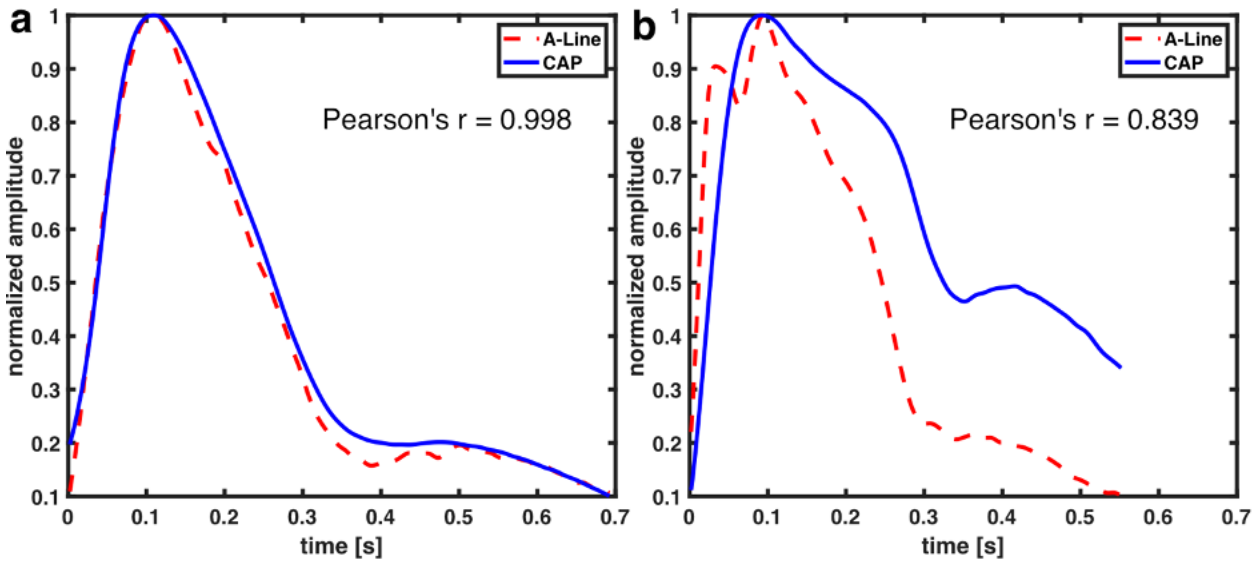

Figure 3.9. Comparison of A-Line and CAP waveform similarity. Both waveforms were derived from radial arteries. Representative figures with a) high and b) low Pearson correlation coefficient.

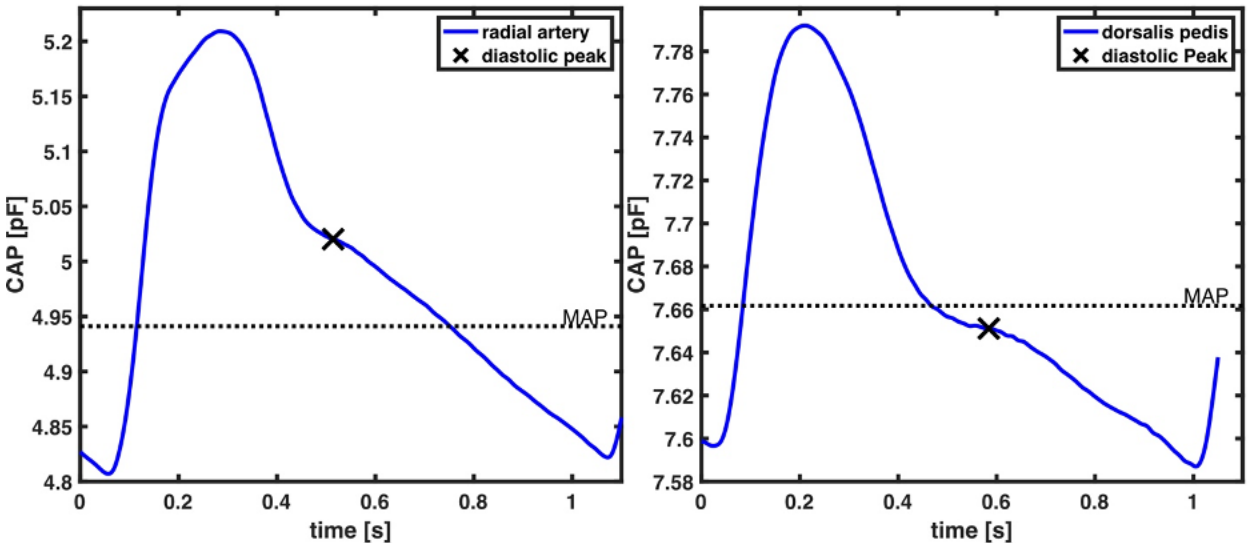

Figure 3.10. Hemodynamic waveform captured from a) radial artery and b) dorsalis pedis. The black dotted line represents the MAP of each wave.

3.5.6 Limitations

The current study is subject to several limitations. Because this is a retrospective study, we went back to calibrate to the A-Line, after completion of data collection. Going forward, a sensor that calibrates to the BP cuff in real-time would be advantageous. The greatest challenge that we had was accounting for motion artifacts and drifts in the signal after motion. We, therefore, had to splice out many sections of the data to account for active movement as captured by the accelerometer. However, outside the window that we spliced out (during active movement), we observed the movement caused a longer-term drift over time. We did not account for such drifts in our analysis but had we done so, the results would be even better. This is evidenced by the fact that if we instead calibrated to the first, middle, and last point of each 60-s epoch (instead of just the average of the first three beats), the averaged mean bias and average SD go down considerably, from 2.3842 ± 12.1908 to −1.8477 ± 7.1906 in DBP and from 1.9153 ± 12.5525 to 1.4324 ± 7.4321 in SBP (**Figure 3.11**). This indicates that the CAP signal drifts over the 60-s epoch. In future iterations, we would like to not toss away all the sections with movement but use machine learning along with the parallel sensor channels to correct for the motion.[69] We would also like to model out the drifts caused by this motion so we can objectively account for and subtract it from the signal. This would undoubtedly improve our agreements with the A-Line. Overall, in summary, we show that the CAP sensor is a promising technology that has good agreement with the A-Line regarding the hemodynamic shape, HR, SBP, and DBP across body habitus and age in OR patients under general anesthesia. While we do observe drifts in the system, we still obtain good correlations with respect to the A-Line as evidenced by excellent linear fit and averaged mean bias and standard deviation across all

patients. Moreover, CAP seems to be able to track fast changes in BP well, which is critical to monitoring hemodynamically unstable patients.

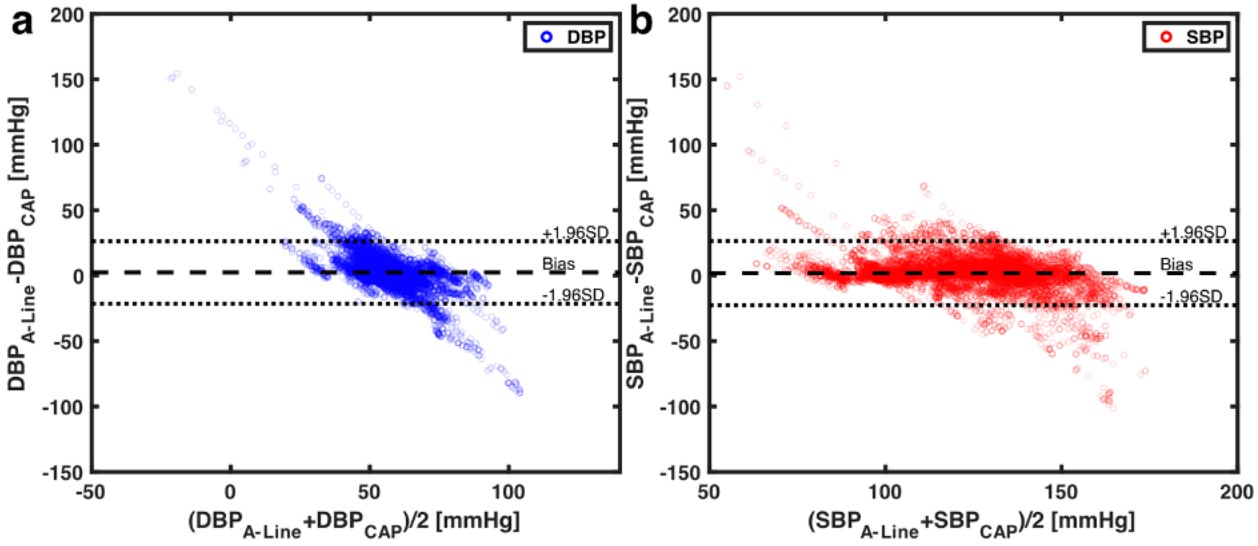

Figure 3.11. Bland-Altman plot using a) 14,645 diastolic and b) 14,674 systolic BP showing level of agreement from valid 60-s segments obtained by A-Line and the CAP sensor. The horizontal black solid, dashed, and dotted lines represent the mean bias, limits of agreement, and the zero line, respectively. The red error bars on the black dashed limits of agreement lines are the 95% confidence intervals of the upper and lower limits.

CHAPTER 4: Effects of ECG data length on heart rate variability among young healthy adults

Portions of this chapter appear in the journal Sensors.[70]

While working on the solutions of aforementioned issues of the CAP system, we have begun the investigation of data interpretation. Heart rate variability (HRV), a measure that tells the variation in time between consecutive heartbeats, is commonly computed by the ECG but can also be obtained with the use of the CAP sensor. Many literature have suggested that HRV was associated with a variety of diseases and disease progressions such as in obstructive sleep apnea (OSA)[71], Type 2 Diabetes Mellitus[72], breast cancer[73], and gastric cancer[74]. However, it didn't seem clear to us what are the minimum lengths to calculate HRV measures. The proposed work reports the appropriate way of each HRV measure which best the future research.

Chapter 4.1: Abstract

The relationship between the robustness of HRV derived by linear and nonlinear methods to the required minimum data lengths has yet to be well understood. The normal ECG data of 14 healthy volunteers were applied to 34 HRV measures using various data lengths, and compared with the most prolonged (2000 R peaks or 750 s) by using the Mann–Whitney U test, to determine the 0.05 level of significance. We found that SDNN, RMSSD, pNN50, normalized LF, the ratio of LF and HF, and SD1 of the Poincaré plot could be adequately computed by small data size (60–100 R peaks). In addition, parameters of RQA did not show any significant differences among 60 and 750 s. However, longer data length

(1000 R peaks) is recommended to calculate most other measures. The DFA and Lyapunov exponent might require an even longer data length to show robust results. Our work suggests the optimal minimum data sizes for different HRV measures which can potentially improve the efficiency and save the time and effort for both patients and medical care providers.

Chapter 4.2: Introduction

HRV is a promising measure used to assess cardiovascular health by investigating heartbeat fluctuations over time. ECG is an autonomically controlled physiological vital signal that changes due to sympathetic or parasympathetic perturbations. As such, reduction in HRV is a well-established biomarker of diabetes[75,76], cardiovascular disease (CVD)[77,78], inflammation[79–81], obesity[19] and psychiatric disorders[82,83]. Over the past half-century, three groups of mathematical methods for determining HRV have been proposed (i) time domain, (ii) frequency domain, and (iii) nonlinear analyses.[84]

Time- and frequency-domain HRV measures were standardized in 1996 by the task force of The European Society of Cardiology and the North American Society for Pacing and Electrophysiology.[85] Nonlinear variability measurements such as the Lyapunov exponent, fractal, entropy, and symbolic entropy are well-established.[86] However, the standardization in selecting a time series length for robustness in differentiating different populations and ailments is currently lacking. HRV measurements are influenced by data length, sampling frequency[87–90], noise[87,91] and, computation parameters used in specific methods such as the time delay and embedding dimensions.[89,92–96] The length of the heart-rate time series data are often considered a limitation for utilizing nonlinear analyses. The number of data points

in time series is critical for nonlinear analysis since it is unknown whether fewer data sets can characterize the whole dynamics of the system.

The length of data is an essential factor considering shorter data acquisition time can improve patient throughput and efficiency of hospitals, healthcare providers, and home monitoring in general. Additionally, it improves patient's adherence and overall experience. An essential part of the HRV analysis is knowing how many data points are needed to describe the system appropriately. An important rule of thumb suggested by researchers is to choose time series of at least 10^d data points with 'd' as the system's embedding dimension.[97] In such a scenario, if the embedding dimension is 6, then at least one million data points are required. However, sometimes obtaining such long time series data from human subjects in controlled clinical environments is practically impossible. For example, to collect one million heartbeats, one has to record ECG continuously for about 277 h. This makes human subject data collection practically impossible. Besides, it is not known if shorter time series can accurately characterize the system's dynamics. An optimal data length should capture the essential dynamics of the system. Thus, it is imperative to understand the relationship between the robustness of the HRV to data lengths, such that the minimum data points necessary for accurate measurements can be determined.

Traditionally in HRV analysis, the data acquisition time is set to at least 5 min.[85] A limitation to longer data acquisition is that the hydrogel layer used in ECG electrodes can degrade and lower the signal-to-noise ratio.[93,98–100] Some studies evaluated the influence of shorter data acquisition time in different HRV measures.[101] For instance, Munoz and coworkers suggested that some time-domain HRV measures can be reliably obtained from

less than a minute of recording.[102] Others investigated the influences of data length in both time- and frequency-domain HRV measures.[93,103–106] In the time-domain analysis, the standard deviation of normal-to-normal (NN) interval (SDNN), root mean square of standard deviation (RMSSD), and the percentage of successive NN intervals greater than 50 ms in all NN internals (pNN50) have been suggested as reliable measures for 5 min data lengths. However, frequency-domain HRV measures cannot produce consistent conclusions. For nonlinear dynamics, Entropy-based HRV measures[107–109] have been used to differentiate patients with cardiovascular disease from healthy controls using shorter time-series data. Sample entropy (SampEn) is reported to be less dependent on data length than approximate entropy (ApEn).[108] In conclusion, the relationship between the robustness of HRV derived by linear and nonlinear methods to the required minimum data lengths has yet to be systematically evaluated and clearly understood.

In addressing such limitations, this study explores how the data length of the ECG signal affects the HRV measures (time and frequency domain variables and nonlinear variables). In this study, 14 healthy volunteers were monitored in resting-state. Various data lengths of ECG recordings were applied to eight (two time, two frequency, and four nonlinear) approaches, including 13 different methods (statistical and geometric methods in time domain, Welch's and Lomb–Scargle in frequency domain, and Poincaré plot, recurrence quantification analysis (RQA), detrended fluctuation analysis (DFA), Wolf and Rosenstein's Lyapunov exponents (LE), ApEn, SampEn, multiscale entropy (MSE), and composite multiscale entropy (CMSE) in nonlinear analyses), and 34 HRV measures (**Figure 4.1**), to determine the shortest data length that can keep the system dynamics

intact. To understand the robustness of optimal minimum data length that can be utilized to quantify HRV, each data set size was compared with the most prolonged (2000 R peaks or 750 s) using the Mann–Whitney U test to determine the 0.05 level of significance.

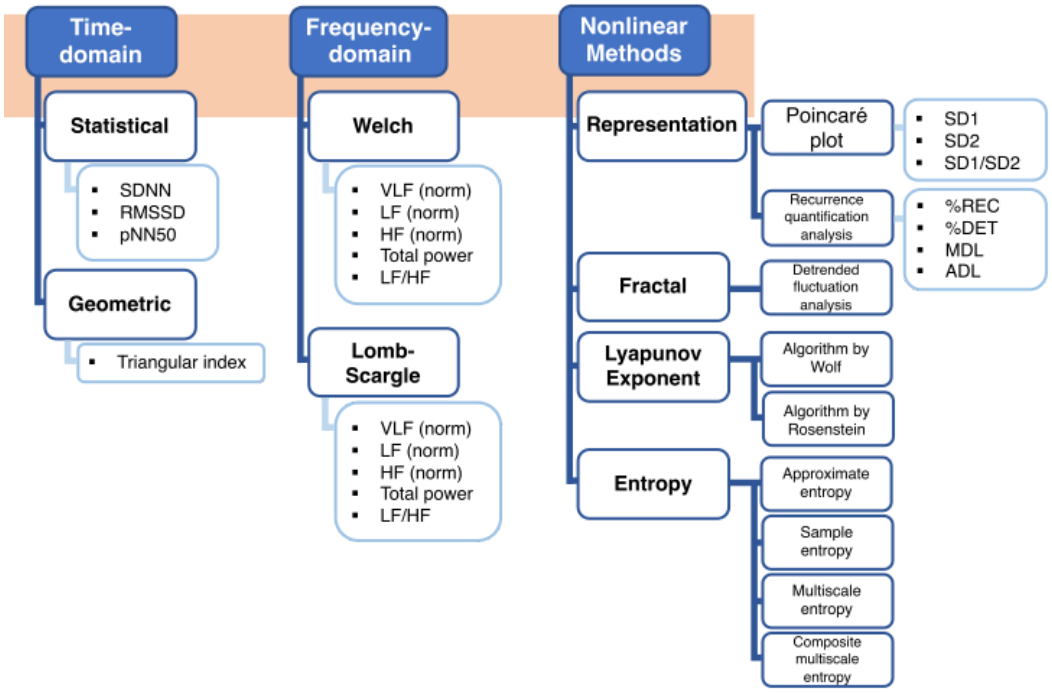

Figure 4.1. Approaches, methods, and outputted measures used to calculate HRV in the study.

Chapter 4.3: Materials and Methods

4.3.1. Subjects

The data was collected from healthy young participants with normal ECG recordings. A total of 14 subjects (seven male) participated with the age of 23.8 ± 4.1 years (mean ± standard deviation) and BMI of 23.4 ± 5.1 kg/cm^2. Participants were excluded if any neurological disorder or heart-related disease was reported. Only one male participant

reported having a history of Kawasaki's disease but did not present any symptoms during this data collection.

4.3.2. Experimental protocol

The ECG signals were recorded with lead II placement at a sampling rate of 2 kHz from 14 subjects by BIOPAC MP36 System (BIOPAC Systems, Inc., Goleta, CA USA). Subjects were asked to avoid taking caffeine two hours before the time of the study. Participants were provided enough rest on the chair (at least five minutes) after arrival to ensure the subjects were recorded in a relatively calm state during the studies. At least 10 minutes of ECG recordings were acquired while the subjects were seated still on the chair. All subjects provided written informed consent for the study, which the Institutional Review Board approved of the University of California (IRB #2016-2924).

4.3.3. Data preprocessing

The effect of data length on HRV measures was quantified by analyzing R-R intervals on the raw ECG recordings using time, frequency domain and nonlinear analyses methods. We segmented and standardized ECG data length using R peaks ranging from 60 to 2000, thus controlling HR difference.[93] In the study, three statistical (SDNN, RMSSD and pNN50) and one geometrical method (triangulation index) were included in time-domain measurements (**Figure 4.1**). Welch and Lomb-Scargle algorithms for each of the eight measures (total power, power, and normalized power of very low-frequency, low-frequency, and high-frequency, and the ratio of low-frequency to high-frequency) were investigated in the frequency-domain method. Eight nonlinear methods were investigated to present

different HRV measures. Besides the RQA, all the measures were computed with consecutive discrete R-R intervals with R peaks ranging from 60 to 2000. RQA was estimated by raw ECG recordings ranging from 60 to 750 seconds. In the section below, we have provided details for i) R peak extraction, ii) evaluation for HRV measures, and iii) statistical analysis.

4.3.4. Extraction of R peaks using wavelet analysis

The consecutive discrete R-R intervals were processed initially from the raw ECG signal. Symlet 4 (Sym4) wavelet was chosen to enhance R peaks by using maximal overlap discrete wavelet transform (MODWT) due to its similarity with the QRS complex as shown in **Figure 4.2**. Potential artifacts as arrhythmic events were excluded. The identified R peaks were then extracted as R-R interval segments used for HRV analysis.

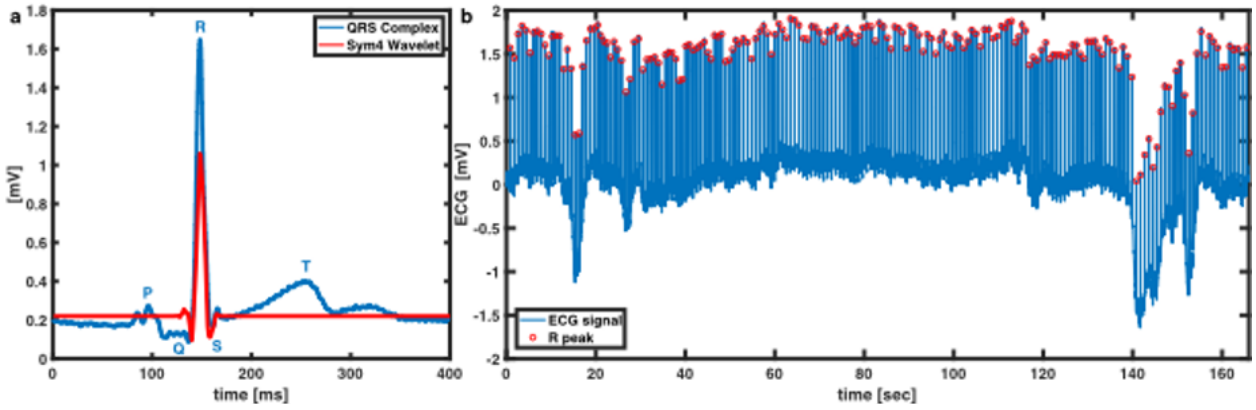

Figure 4.2. R peak detection technique. a) Sym4 resembles the QRS complex that can be used for the wavelet transform. b) A representative raw ECG signal with extracted R peaks in red circles.

4.3.5. Time-domain analysis

Three statistical measures (SDNN, RMSSD, pNN50) and a geometric measure (Triangular index) were discussed in time-domain analysis. SDNN is the standard deviation of the normal-to-normal (NN) interval. RMSSD represents the square root of the mean of the sum of the squares of differences between adjacent NN intervals. pNN50 calculates the ratio of the counts of adjacent NN intervals that are more than 50 ms and the total number of NN intervals in the dataset. The basic variable in the geometric method, HRV triangular index, is also computed (**Equation 4-1**).

$$HRV\ Triangular\ Index\ =\ \frac{total\ number\ of\ NN\ intervals}{number\ of\ NN\ intervals\ in\ the\ modal\ bin} \quad (4\text{-}1)$$

SDNN, RMSSD, pNN50 and HRV triangular index were computed as standards of measurement.[85]

4.3.6. Frequency-domain analysis

According to the task force's guideline[85], frequency domain measures of HRV can be categorized into four bands, ultra-low-frequency (ULF, ≤ 0.003 Hz), very low-frequency (VLF, 0.003-0.04 Hz), low-frequency (LF, 0.04-0.15 Hz), and high-frequency (HF, 0.15-0.4 Hz). It is also suggested that VLF, LF, and HF rhythms are distinct components for a 2–5-minute short-term ECG recording. Hence, there were eight parameters calculated in the study: i) VLF power, ii) LF power, iii) HF power, iv) total power, v) normalized VLF (VLF norm), vi) normalized LF (LF norm), vii) normalized HF (HF norm), and viii) the ratio of LF to HF (LF/HF). The total power is a sum of the VLF, LF, and HF absolute power. The

normalized HRV power is defined as the proportion of one power range to the total power in absolute values and allows to compare individuals and various data lengths appropriately. To estimate HRV power spectral analysis, both Welch's method[110] and Lomb-Scargle periodogram[111,112] were applied. Welch's method utilizes Fast Fourier Transform (FFT) and is advantageous for low computation workload. The original signal with data points is split into K segments, $X_1(j),\ ..., X_K(j)$. Each segment has a length of L and is apart from the previous segment in the distance of D such that N can be written as **Equation 4-2**.

$$N = (K - 1)D + L. \tag{4-2}$$

The overlapped segments are helpful to mitigate the loss. The windowed finite Fourier transform $A_k(n)$ is applied to each segment ($k = 1, 2,\ ...,\ K$) with a data window $W(j)$ where $j = 0,\ ...,\ L - 1$ as **Equation 4-3**.

$$A_k(n) = \frac{1}{L}\sum_{j=0}^{L-1} X_k(j)W(j)e^{-\frac{2kijn}{L}} \qquad n = 0,\ ...,\ \frac{L}{2}, \tag{4-3}$$

where $X_k(j)W(j)$ is the windowed segment sequences and $i = \sqrt{-1}$. Therefore, the modified periodogram, $P_k(f_n)$, for each segment, can be written as **Equation 4-4**.

$$P_k(f_n) = \frac{L^2|A_k(n)|^2}{\sum_{j=0}^{L-1} W^2(j)} \qquad f_n = \frac{n}{L} \qquad n = 0,\ ...,\ \frac{L}{2}. \tag{4-4}$$

And Welch's method is estimated as the average of the periodogram values as **Equation 4-5**.

$$\langle P(f_n) \rangle = \frac{1}{K} \sum_{k=1}^{K} P_k(f_n). \quad (4\text{-}5)$$

The Lomb-Scargle periodogram is inspired by Fourier transform and a least-squares method known for identifying periodicity. It offers advantages in dealing with unevenly sampled data and allows ectopic or missing beats.[113–115]

4.3.7. Nonlinear methods

We investigated several nonlinear variability methods such as Poincaré plots, fractal dimension, Lyapunov exponent, entropy in the study.

4.3.7.1. Poincaré plot

The Poincaré plot is a nonlinear technique that can depict HRV in a two-dimensional graphic. It visualizes the beat-to-beat detail to dispersion and provides quantitative information on cardiac performances. Popular approaches to quantify Poincaré plot include ellipse fitting, histogram, and correlation coefficient. The study characterized the R-R interval as illustrated by the Poincaré plot by fitting an ellipse as in the **Figure 4.3**.[116–118]

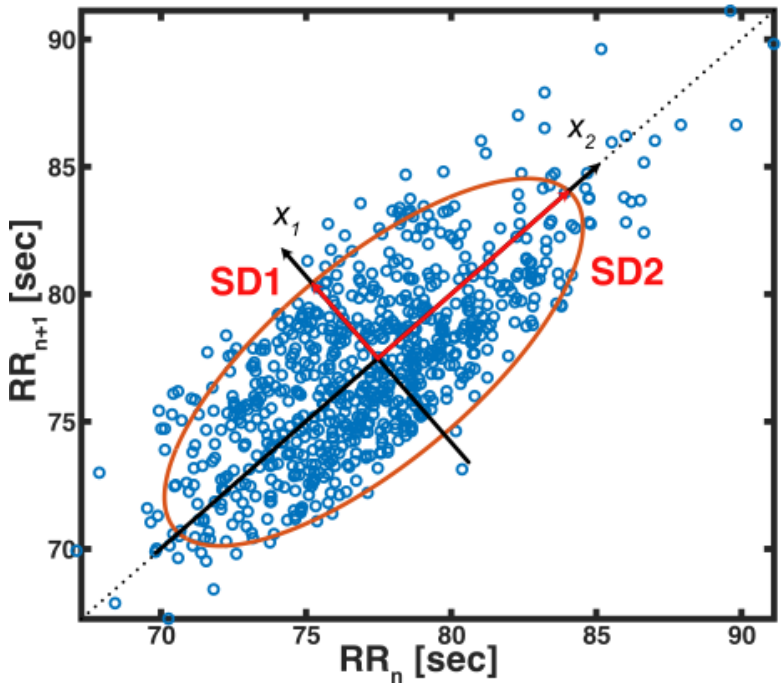

Figure 4.3. A representative Poincaré plot with a new set of a coordinate plane. x_1 and x_2 are the axes of the plane. $SD1$ and $SD2$ represent the radii of a fitted ellipse on x_1- and x_2-axis.

A new set of the coordinate plane, x_1 and x_2, is formed at the intersection of the ellipse center (**Equation 4-6**).

$$\begin{bmatrix} x_1 \\ x_2 \end{bmatrix} = \begin{bmatrix} \cos\theta & -\sin\theta \\ \sin\theta & \cos\theta \end{bmatrix} \begin{bmatrix} RR_n \\ RR_{n+1} \end{bmatrix} \quad (4\text{-}6)$$

$SD1$ and $SD2$ represent the distribution of points perpendicular and parallel to the line-of-identity of the fitted ellipse, which indicated the level of short- and long-term variability.[119,120] Mathematically, $SD1$ and $SD2$ are the standard deviations around x_1 and x_2, respectively. They were computed by using linear measures of HRV as shown in **Equation 4-7** and **4-8**:[120]

$$SD1^2 = Var(x_1) = Var(\frac{1}{\sqrt{2}}RR_n - \frac{1}{\sqrt{2}}RR_{n+1}) \\ = \frac{1}{2}Var(RR_n - RR_{n+1}) = \frac{1}{2}SDSD^2 \quad (4\text{-}7)$$

$$SD2^2 = 2SDNN^2 - \frac{1}{2}SDSD^2, \quad (4\text{-}8)$$

where the standard deviation of the differences between adjacent RR intervals is denoted by $SDSD$. The axis ratio $SD1/SD2$ indicates the relationship of the instantaneous interval variation to the long-term variation.

4.3.7.2. Approximate entropy

Approximate entropy (ApEn) is a method to quantify the complexity of time-series data. Its application is limited to data lengths greater than 100 data points.[121,122] Complexity can quantify variability to indicate the unpredictability of HR fluctuations. To assess complexity, ApEn was computed as the difference between the probability of the series of a vector with a fixed data length and the probability of the series of another vector with a similar length $(m + 1)$ that both fall within a tolerance as **Equation 4-9**.

$$ApEn(m, r, N) = \Phi^{m+1}(r) - \Phi^m(r), \quad (4\text{-}9)$$

where $\Phi^m(r)$ from the element in Eckmann-Ruelle (E-R) entropy[123] is defined in **Equation 4-10**

$$\Phi^m(r) = \frac{1}{N-m+1}\sum_{i=1}^{N-m+1} logC_i^m(r), \quad (4\text{-}10)$$

where $C_i^m(r)$ is the conditional probability of vector length m.

Pincus et. al. recommended that given 1,000 data points, using parameters $m = 2$ and r value between 0.1 to 0.25 of data standard deviation gave a robust result of ApEn.[121,124] Hence, ApEn was applied to different quantities of R-R interval time series with the values $m = 2$ and $r = 0.2$ in this study.

4.3.7.3. Sample entropy

Sample entropy (SampEn) was initially introduced 9 years after ApEn.[125] With a similar goal, SampEn is a useful mathematical algorithm that measures the predictability in time series and can be viewed as a refinement of ApEn. SampEn addressed ApEn's shortcoming as its ability to have independence for different data lengths and showed robustness for the change of data lengths.[125–127] Richman and Moorman defined the negative natural logarithm of the probability using vector length m, tolerance r, and signal data length N from ApEn **(Equation 4-11)**.

$$SampEn(m, r, N) = -\ ln\frac{A}{B}, \tag{4-11}$$

where A and B are $\frac{(N-m)(N-m-1)}{2}$ times the sum of all the conditional probabilities, C_i^{m+1} and C_i^m, divided by $N - m$ without considering the self-matches, respectively.

4.3.7.4. Multiscale entropy

The traditional multiscale entropy (MSE) algorithm[128,129] is conducted in two parts: i) a coarse-graining procedure for different scaled time series from an original signal; ii) SampEn is used to calculate each time series scale. However, some disadvantages of

traditional MSE had been issued.[130] Therefore, several newly developed MSE methods were reported.[102,131–133] However, most of the solutions suggested modifying the first step's time-series scale with different algorithms or using other entropies for the second step instead.[134] Therefore, instead of the conventional MSE, composite multiscale entropy (CMSE)[133] was used to evaluate cardiovascular complexity in the study. Traditional MSE computed SampEn with the first coarse-grained time series of each scale only (**Equation 4-12**)

$$MSE(x,\ \tau,\ m,\ r)\ =\ SampEn(y_1^{(\tau)},\ m,\ r), \tag{4-12}$$

where x is the original one-dimensional time series, τ is the scale factor, and the same parameters m and r from computing SampEn. **Equation 4-13** is the first coarse-grained time series $y_1^{(\tau)}$ which is defined as:

$$y_{1,j}^{(\tau)} = \frac{1}{\tau}\sum_{i=(j-1)\tau+1}^{j\tau} x_i, \qquad 1 \le j \le \frac{N}{\tau} \tag{4-13}$$

Nevertheless, the SampEn of the first coarse-grained time series derives poor reliability. CMSE algorithm was then introduced to overcome the problem.[133] Therefore, instead of using the first coarse-grained time series, all the coarse-grained time series SampEn are considered in CMSE as shown in **Equation 4-14**.

$$CMSE(x,\ \tau,\ m,\ r)\ = \frac{1}{\tau}\sum_{k=1}^{\tau} SampEn(y_k^{(\tau)},\ m,\ r), \tag{4-14}$$

where $y_k^{(\tau)}$ represents the coarse-graining procedure is determined from x_k, the kth data point from the original signal (**Equation 4-15**).

$$y_{k,j}^{(\tau)} = \frac{1}{\tau} \sum_{i=(j-1)\tau+k}^{j\tau+k-1} x_i, \qquad 1 \le j \le \frac{N}{\tau},\ 1 \le k \le \tau \tag{4-15}$$

4.3.7.5. Detrended fluctuation analysis

In time series analysis, detrended fluctuation analysis (DFA) is used to estimate self-similarity. It is calculated as the root-mean-square error of the least-squares line fitted in separate non-overlapping windows of the cumulative integral of the original time series. For example, given the interbeat intervals of an original ECG signal in time series x with length N, the cumulative integral of the signal $y(k)$ is written as **Equation 4-16**.

$$y(k) = \sum_{i=1}^{k} (x(i) - < x >). \tag{4-16}$$

where $<x>$ denotes the average of x. $y(k)$ is then divided into segments of equal length n. The root-mean-square fluctuation F as a function of the window sizes n is computed by **Equation 4-17**.

$$F(n) = \sqrt{\frac{1}{N} \sum_{k=1}^{N} \left[y(k) - y_n(k) \right]^2}. \tag{4-17}$$

where $y_n(k)$ is the y-coordinate of the linear fitted line in each of the segments.

The fluctuation is indicated as the slope of $F(n)$ versus n in a logarithmic scale by a scaling exponent α. Peng's work found that there is a significant difference in α over a wide range of window sizes ($20 \leq n \leq 1000$) among the interbeat interval time series of 15 severe heart failures and 12 controls.[135]

4.3.7.6. Recurrence quantification analysis

The research of recurrences is commonly used to understand the complexity of a nonlinear dynamical system. The RQA is known for being able to handle short and nonstationary data. Recurrence plot (RP) and its quantification measures are the tools to visualize and quantify the recurrence behavior of the state space trajectory.[136–138] RP was first introduced in 1987, allowing the recurrences of higher dimensional phase space to be visualized by a two-dimensional representation.[139] It is an effective way to understand the behavior of a dynamic system. Mathematically, it shows the phase space vectors $\overline{x}$ that recur at time i and another time j (**Equation 4-18**)

$$R_{i,j} = \Theta(\varepsilon_i - \left\|\overline{x_i} - \overline{x_j}\right\|), \quad \overline{x_i} \in R^m, \quad i, j = 1,..., K, \tag{4-18}$$

where K is considered size for the recurrence matrix, m is the highest dimension being investigated, ε_i is a threshold distance, and $\Theta(.)$ is the Heaviside function.

To infer RQA, there are three parameters that need to be taken into consideration, a time-delay τ, the embedding parameter D, and a threshold distance ε. The time-delay parameter of Takens Embedding Theorem[140] brings the original one-dimensional time series into multiple dimensional manifolds. Here, the average mutual information (AMI) is

used to estimate τ.[141] Essentially, AMI calculates the least dependent information in the time-delayed coordinates. Then, the embedding parameter comes in to reconstruct the phase space vector since a time delay is applied to the raw data. The choice of a deficient *D* may lead to unwanted results such as the false bifurcation points.[141] Hence, false nearest neighbors,[142] which inspects whether there's a significant change in distance between two adjacent data points with embedding dimensions, was used to determine *D* here. In our work, the time-delay and embedding parameters were chosen as the median values across 14 studies ($\tau = 22$ and $D = 2$). Lastly, the threshold distance parameter defines who the RP neighbors are as the radius of a sphere. To select a sufficient threshold distance can be critical, it may lose the key information of the recurrence structure or include a lot of artifacts if ε is chosen too small or too large.[86,143] It is suggested that a proper selection of ε should correspond to a specific range of the percent recurrence (%REC), a quantification measure discussed in detail in the next paragraph.[137,144]

In comparing various subsets of data, the recommended threshold parameter should be chosen so that a typical %REC is in the range of 5% to 10% and the minimum is at least 1%.[144] The threshold of 8 fulfilled the guideline in the study. The quantification measures are used to characterize the information in RPs. Four of them, %REC, percent determinism (%DET), the average diagonal line length (ADL), and the maximum diagonal line length (MDL), were reported in the paper. %REC quantifies the percentage of recurrent points in a RP (**Equation 4-19**)

$$\%REC = \frac{sum\ of\ recurrent\ points}{size\ of\ RP} * 100. \quad (4\text{-}19)$$

The minimum (0%) and maximum (100%) represent that no points and all the points are fallen into the -defined recurrent sphere, respectively. The second parameter, %DET, measures the percent recurrent points occurring in connected trajectories is of total counts of recurrent points (**Equation 4-20**). The connected trajectories are formed by the continuous adjacent of two or more points that follow the diagonal lines.

$$\%DET = \frac{sum\ of\ diagonally\ adjacent\ recurrent\ points}{sum\ of\ recurrent\ points\ in\ RP} * 100. \quad (4\text{-}20)$$

ADL calculates the average length of connected trajectories. And MDL simply counts the length of the longest connected trajectory in the RP.

4.3.7.7. Lyapunov exponent

The Lyapunov exponent (LE) of a dynamical system is a quantity that measures how fast two infinitesimally close trajectories separate in phase space based on the initial condition. For instance, one point would exponentially diverge from another if the system is chaotic. Given two close trajectories, $x(t)$ and $y(t)$ are a function of time, **Equation 4-21** shows the next iteration after time separates their distance exponentially.

$$|x(t + \varepsilon) - y(t + \varepsilon)| = |x(t) - y(t)|e^{\lambda_1 \varepsilon}, \quad (4\text{-}21)$$

where λ_1 represents as the first LE (**Equation 4-22**). Hence, the first LE can be written as

$$\lambda_1 = \lim_{\varepsilon \to \infty} \lim_{|x(t)-y(t)| \to 0} \frac{1}{\varepsilon} ln\left(\frac{|x(t+\varepsilon)-y(t+\varepsilon)|}{|x(t)-y(t)|}\right). \quad (4\text{-}22)$$

The rate of separation, LE, may vary for different orientations of the initial two close trajectories. λ with a positive value ($\lambda > 0$) means the trajectories diverge exponentially.

On the contrary, two nearby points converge exponentially, which leads to a negative value of λ ($\lambda < 0$). That is to say, the larger the value of LE, the lower the predictability for a dynamical system. The largest Lyapunov exponent (LLE) is commonly referred to as the indicator of chaos. There are various computational methods to quantify LLE. Two widely used algorithms, Wolf and Rosenstein methods, are included in the study. Both track the divergence of nearest neighbors over time. However, Wolf's algorithm[145] takes one trajectory as the reference only (**Equation 4-23**). Thus, each point on the reference trajectory iterates with its single nearest neighbor's trajectory over time until their distance apart from each other grows beyond a threshold.

$$\left|\left|z(t_i) - x(t_i)\right|\right| = L(i), \tag{4-23}$$

where i is the increment, L is the difference in two trajectories, x is the point on the reference trajectory, and z is the nearest neighbor of the corresponding point. The reference point re-evaluates the new single nearest neighbor once the previous trajectory's separation is large. This procedure of following the nearest neighbor and replacing with another trajectory completes at the end of the reference trajectory. The distance between the reference point and the beginning and last point of each new nearest neighbor trajectory is denoted as L and L', respectively. The LLE by Wolf's algorithm, λ_1, tracks all the L and L'.

$$\lambda_1 \simeq \frac{1}{K}\sum_{i=0}^{M-1} ln\frac{L'_i}{L_i}, \tag{4-24}$$

where M represents the number of nearest neighbor trajectories and K is the total number of iterations in the reference trajectory.

Instead of focusing on a single nearest neighbor, Rosenstein's method[146] finds the nearest neighbor overall points on the trajectory. The distance of a certain reference point, X_j, to its nearest neighbor X_j' can be express as **Equation 4-25**.

$$d_j(0) = min_{X_j'} \left|\left| X_j - X_j' \right|\right|, \tag{4-25}$$

where $d_j(0)$ means the initial distance between the jth point and the nearest neighbor. The LLE by Rosenstein's work can be estimated as the average speed of nearest neighbor separation (**Equation 4-26**).

$$d_j(i) \approx C_j e^{\lambda_1 (i\Delta t)}, \tag{4-26}$$

where Δt is the time period of each iteration, i is the number of iterations, and C_i as the initial separation.

In our approach, the original one-dimensional signal was reconstructed using aforementioned methods to define parameters, time-delay τ and embedding dimension D (details in RQA section). To compare different data lengths, each τ and D in a particular data length group were obtained as the median values across all participants. The selected values of τ and D in each group are referenced in **Table 4.1**.

Table 4.1. The values of time-delay and embedding dimension used in different data lengths

Length (R peaks)	Time-delay	Embedding Dimension
60	2	2
100	3	2
150	2	3
200	3	3
300	2	3
400	3	4
500	3	4
750	3	4
1000	4	4
1500	3	4
2000	5	5

4.3.8. Statistical analysis

A total of 34 HRV indices were computed in this study. The indices were divided into three groups: the effect of data length on i) time-domain, ii) frequency-domain, and iii) nonlinear HRV measures. Descriptive data are presented as means and SD for continuous HRV variables. Normal distribution of all time/frequency-domain, linear/nonlinear variables was tested using the Kolmogorov-Smirnov test and visually inspected histograms and Q-Q plots. HRV parameters from ECG recordings did not exhibit normal distributions and were analyzed as non-parametric. To understand the robust/optimal minimum data length that can be utilized to quantify HRV in the methods as mentioned above, each dataset size was compared against the most extended (2000 R peaks or 750 seconds) using the Mann-Whitney U test in R. Moreover, HRV measures were then calculated with several randomly chosen segments and compared against each other using the Mann-Whitney U test to eliminate the possibility of biased results from short data length selection. The critical value was chosen at the 0.05 level of significance.

Chapter 4.4: Results

4.4.1. Time-domain HRV

Among the four time-domain HRV measures presented in the paper, we find SDNN, RMSSD, and pNN50 are consistent for very short-term HRV analysis (**Table 4.2**). SDNN in 100 R peaks was not significantly different from SDNN at 2000 R peaks. Similarly, a minimum of 60 R peaks of RMSSD and pNN50 were found consistent with longer (2000 R peaks) HRV recordings. HRV triangular index, however, is recommended to use with at least 1000 R peaks. This means that if one were an adult with a normal resting HR, a 10 to 16-minute recording would have no statistically significant difference compared to a 20 to 33-minute recording.

4.4.2. Frequency-domain HRV

Both Welch and Lomb-Scargle periodograms were included in HRV power spectral analysis (**Table 4.2**). With Welch's method, the appropriate minimum length for acquiring VLF power, LF power, total power, and VLF norm was 1000 R peaks. HF norm analysis could use 750 R peaks. HF power, LF norm, and LF/HF ratio had no change from 60 to 2000 R peaks. On the contrary, the lengths required to calculate HRV measures by Lomb-Scargo periodogram were shorter than Welch's in general. However, the recommended lengths to obtain VLF norm, LF norm, and LF/HF ratio remained the same. Furthermore, using 200, 500, 500, and 750 R peaks for HF norm, LF power, total power, and HF power, respectively,

were acceptable. VLF power with the Lomb-Scargle algorithm had no statistically

significant difference using very short-term recordings.

Table 4.2. Mann-Whitney U test results for comparing HRV measures at 2000 R peaks with shorter data lengths. Data length is in R peaks. Statistical significant differences ($p<0.05$) and statistical highly significant differences ($p<0.001$) are color labeled in lighter and darker gray with bold font, respectively.

Length	60	100	150	200	300	400	500	750	1000	1500
Time-domain HRV										
Geometric measure										
Triangular index	**<0.000**	**0.002**	**0.004**	**0.004**	**0.005**	**0.008**	**0.017**	**0.048**	0.148	0.800
Statistical measure										
SDNN	**0.016**	0.056	0.056	0.069	0.056	0.062	0.104	0.094	0.265	0.946
RMSSD	0.982	0.804	0.667	0.734	0.734	0.701	0.701	0.635	0.769	1.000
pNN50	0.945	0.909	0.730	0.872	0.836	0.765	0.909	0.836	0.909	0.982
Frequency-domain HRV										
Welch's periodogram										
VLF	**<0.000**	**0.002**	**0.002**	**0.002**	**0.001**	**0.003**	**0.006**	**0.009**	0.104	0.734
LF	**0.035**	**0.050**	0.104	0.056	**0.044**	**0.048**	**0.044**	**0.044**	0.210	0.839
HF	0.603	0.804	0.910	0.839	0.874	0.910	0.874	0.946	0.982	0.982
Total power	**0.016**	**0.039**	**0.050**	**0.050**	**0.044**	**0.035**	0.057	**0.050**	0.210	0.910
VLF norm	**<0.000**	**<0.000**	**<0.000**	**<0.000**	**<0.000**	**0.001**	**0.005**	**0.009**	0.103	0.646
LF norm	0.946	0.701	0.734	0.927	0.804	0.769	0.748	0.946	0.734	0.890
HF norm	**0.008**	**0.003**	**0.008**	**0.014**	**0.019**	**0.024**	**0.044**	0.085	0.137	0.734
LF/HF	0.137	0.062	0.085	0.062	0.069	0.085	0.113	0.183	0.306	0.839
Lomb-Scargle's periodogram										
VLF	0.945	0.121	0.188	0.105	0.256	0.306	0.418	1.000	0.069	0.728
LF	**<0.000**	**<0.000**	**0.006**	**0.004**	**0.013**	**0.050**	0.188	0.188	0.798	0.694
HF	**<0.000**	**<0.000**	**0.001**	**0.001**	**0.003**	**0.011**	**0.030**	0.112	0.982	0.963
Total power	**<0.000**	**<0.000**	**0.001**	**<0.000**	**0.001**	**0.013**	0.073	0.140	0.645	0.890
VLF norm	**<0.000**	**<0.000**	**<0.000**	**0.002**	**0.002**	**0.010**	0.056	**0.040**	0.358	0.804
LF norm	0.137	0.435	0.839	0.807	1.000	0.982	0.910	0.769	0.890	0.982
HF norm	**0.027**	0.077	**0.048**	0.062	0.081	0.094	0.178	0.198	0.511	0.818
LF/HF	0.839	0.541	0.482	0.511	0.520	0.401	0.520	0.804	0.734	0.982
Nonlinear HRV										
Poincaré plot										
SD1	0.667	1.000	0.890	0.963	0.908	0.874	0.910	0.769	0.854	0.910
SD2	**0.009**	**0.031**	**0.021**	**0.027**	**0.014**	**0.014**	**0.031**	**0.044**	0.198	0.910
SD1/SD2	**0.004**	**0.002**	**0.008**	**0.011**	**0.009**	**0.014**	**0.039**	0.085	0.150	0.667
Entropy										
SampEn	**0.046**	**0.009**	**0.006**	**0.007**	**0.035**	**0.021**	**0.031**	0.077	0.329	0.734
ApEn	**<0.000**	**<0.000**	**<0.000**	**<0.000**	**<0.000**	**<0.000**	**0.011**	0.541	0.701	0.511
MSE	**0.005**	0.125	**0.012**	**0.003**	**0.002**	**0.003**	**0.007**	**0.035**	0.164	0.874
CMSE	**<0.000**	**0.002**	**0.007**	**0.002**	**0.009**	**0.004**	**0.009**	0.062	0.164	0.839
Fractal										
DFA	**<0.000**	**<0.000**	**<0.000**	**<0.000**	**<0.000**	**<0.000**	**0.002**	**<0.000**	**0.002**	0.667
Lyapunov exponent										
Wolf	**<0.000**	**<0.000**	**<0.000**	**0.035**	**<0.000**	**0.001**	0.069	0.085	**0.002**	0.701
Rosenstein	**<0.000**	**<0.000**	**<0.000**	**<0.000**	**<0.000**	**<0.000**	**<0.000**	**<0.000**	**0.002**	**<0.000**

4.4.3. Nonlinear HRV

The statistical results of nonlinear HRV indices were separated into two tables. The majority of nonlinear HRV indices are shown in **Table 4.2**. The measures of RQA are listed in **Table 4.3**. As a whole, the adequate lengths of nonlinearly assessed HRV measures were longer than those of linearly assessed methods.

Poincaré plots, when compared with different data lengths, did not show any differences with . However, the minimum lengths of 1000 and 750 R peaks were not significantly different compared to the maximum (2000 R peaks) for and , respectively (**Table 4.2**). Furthermore, as entropy-based approaches, using 750 R peaks to quantify SampEn, ApEn, and CMSE showed no significant differences compared to maximum length (2000 R peaks), however traditional MSE was significantly different until 750 R peaks and robust for longer data lengths. Statistical results showed that DFA and Wolf and Rosenstein's LE were affected due to the data length. The minimum data length for DFA and Wolf's LE was 1500 R peaks such that no significant difference was found compared to 2000 R peaks (maximum data length). However, Rosenstein's LE showed significantly different values in all the data lengths when compared to full data length (2000 R peaks). Four parameters of RQA (Recurrence (REC), determinism (DET), Maximum Diagonal Length (MDL) and Average Diagonal Length (ADL)) were computed for different data lengths to compare with the maximum (ECG data of 750 seconds or 12.5 minutes) data. The

results did not show any significant differences among 1 minute and 12.5 minutes of %REC, %DET, MDL and ADL.

Table 4.3. Mann-Whitney U test results for comparing measures of RQA at 750 seconds with shorter data lengths. No significant differences show in any length considered.

Length (sec)	60	100	150	200	300	400	500	600
%REC	0.910	0.910	1.000	0.946	1.000	0.874	0.946	0.982
%DET	1.000	0.982	0.946	1.000	1.000	0.946	1.000	0.946
MDL	0.982	0.769	0.839	0.982	0.804	1.000	1.000	0.982
ADL	0.701	0.910	0.982	0.982	0.946	0.946	0.982	0.946

Table 4.4 shows recommended minimum data length suggesting consistency and unbiased to maximum data length (2000 R peaks) using the Mann-Whitney U test. We have reported time- and frequency-domain HRV measures and minimum data length with consistency. We found that most of nonlinear variables required a minimum data length of 1000 or 1500 R peaks. However, this was not the case for of Poincaré plot and RQA measures.

Table 4.4. The recommended minimum data length of each HRV measure.

HRV Parameters	Recommended minimum data length (R peaks)
Time-domain HRV	
Geometric measure	
Triangular index	1000
Statistical measure	
SDNN	100
RMSSD	60
pNN50	60
Frequency-domain HRV	
Welch's periodogram	
VLF	1000
LF	1000
HF	60
Total power	1000
VLF norm	1000
LF norm	60
HF norm	750
LF/HF	60
Lomb-Scargle's periodogram	
VLF	60
LF	500
HF	1000
Total power	500
VLF norm	1000
LF norm	60
HF norm	500
LF/HF	60
Nonlinear HRV	
Poincaré plot	
SD1	60
SD2	1000
SD1/SD2	1000
Entropy	
SampEn	1000
ApEn	1000
MSE	1000
CMSE	1000
Fractal	
DFA	1500
Lyapunov exponent	
Wolf	1500
Rosenstein	-

We investigated the effects of data length HRV measures on 14 participants utilizing the Mann-Whitney U test. Box plots were used to summarize the distribution in each HRV measure per data length (**Figure 4.4**). Figure 4a shows how data length affects the

complexity (ApEn) of the R-R interval data. With the data length increasing from 60 to 2000 R peaks, the overall value of ApEn showed a linear trend and reached a plateau around 750 R peaks. The median values and the 25-75 percentile range among 750 to 2000 R peaks remained consistent, contrasting to 60 to 500 R peaks (showed increasing linear trend). Unlike the pattern in ApEn, Rosenstein's LE showed inconsistency while the data lengths increased. In **Figure 4.4.b**, the box plots of Rosenstein's LE show scattered values with the observation of outlier quantity. Both MSE (**Figure 4.4.c**) and CMSE (**Figure 4.4.d**) had more extensive percentile ranges in shorter data lengths and a similar variation of median values after 200 R peaks.

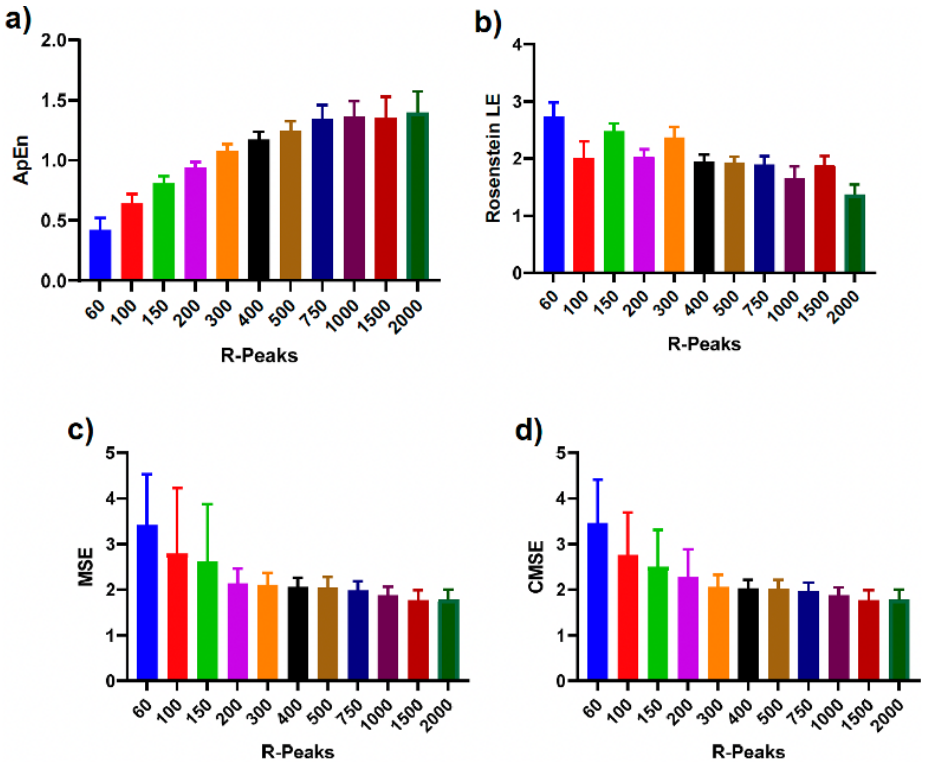

Figure 4.4. Bar plots of **a)** ApEn, **b)** Rosenstein's LE, **c)** MSE, and **d)** CMSE with different numbers of R peaks. Different R-peaks are represented with different colors for four nonlinear methods. The error bars represent SD of the values among 14 participants.

Chapter 4.5: Discussion

In this study, we investigated the effects of ECG data series length on the consistency of HRV parameters. Conventionally, short assessments of five minutes of ECG data are used for analysis (approximately 360 R-R intervals)[85] and in this study, we evaluated the statistical differences of HRV measures at different data lengths to maximum data length (2000 R peaks). We investigated 34 HRV measures in this study, including (i) time-domain, (ii) frequency-domain, and (iii) nonlinear analysis variables. We found a length of 1000 R peaks or more could provide a precise estimate of HRV for time and frequency domain variability features. Moreover, we found all variables were affected by ECG data length. For example, in the general frequency domain variables are more unstable for up to 750 R peaks of data length.

4.5.1. Importance of short data sets and R-R intervals

Although 24-hour recording is known as the gold standard for HRV analysis, a short-term variability may be capable to evaluate the interactions between the sympathetic and parasympathetic nervous system.[147] This research is essential since variation in ECG recording length may result in differences in outcomes of HRV analysis in all temporal, frequency-based, and linear/nonlinear analyses. When recordings with different duration are compared, it should be considered to use the most prolonged duration as a standard of comparison for stable HRV values. This will allow us to identify the minimum length of ECG data that can capture system dynamics without significantly differing results from long datasets. A quick HRV analysis may serve as a promising diagnostic tool in healthcare. An effort to shorten ECG data recording is critical since HRV features add essential information

for cardiac functioning. Our study highlights that most of the HRV measures are sensitive to changes in the data length. We found the sensitivity of each HRV measure was affected by the change in data lengths. It is important to note that a faster HR leads to a smaller HRV.[93] Hence, unlike most others using time as the length reference, the quantity of R peaks ranging from 60 to 2000 was used instead to avoid HR variation.[148]

4.5.2. Linear ECG variability measures

Chen and co-workers conducted a study with 3,387 adult participants with ECG recordings of longer than two minutes. But reported that such long ECG recording may not be required since the valid results of RMSSD and SDNN could be attained from 10 and 30-second of ECG recordings respectively.[102] The robustness of RMSSD from 10-second recordings was also corroborated in Thong's work.[93,104] However, 10-second based SDNN assessment was found inconsistent by both studies concluding linear variability measure like SDNN was more sensitive to data length than RMSSD. Similarly, some other studies reported similar results of RMSSD and SDNN when compared data lengths of three and five minutes[93], 50-seconds[104], and 5-minute[105,149,150] measurements as the reference. On the other hand, pNN50 evaluated from three and five minutes showed similar values.[93] Short ECG datasets of 20-second of pNN50 could reliably estimate similar to 150-second.[104] Thus, our results indicate that RMSSD and pNN50 were the least sensitive to data lengths. A shorter ECG data length of 30 seconds for SDNN evaluation could potentially replace existing guidelines by the task force.[85] The HRV triangular index was found to be affected by data length and this was consistent with previous findings.[149]

4.5.3. Frequency-domain analysis

The frequency-domain HRV measures were evaluated as per standard techniques defined by the task force.[85] We investigated two frequency domain HRV analysis methods using Welch periodogram and Lomb-Scargle. Previously, Thong investigated 10-second HRV data for HF band variables and reported results as unreliable for accuracy.[103] McNames and Aboy concluded that the performances of HF variable ranging from 10 seconds to 10 minutes compared with the five-minute estimation were comparable with the results in mean HR.[149] In addition, the study has shown that 40-second HF and 50-second LF/HF, LF norm and HF norm were reliable to monitor mental stress under mobile settings.[104] Similar to Salahuddin's work, we found 60 R peaks (36- to 60-second) LF/HF and LF norm had no significant differences with 2000 R peaks using either Welch or Lomb-Scargle algorithm. In addition, the task force manual suggested that it could be inappropriate to assess VLF in short-term recordings (≤5 minutes). However, our findings show that the optimum data length to estimate VLF depends on the methods of power spectral density (for example, 1000 and 60 R peaks in using Welch and Lomb-Scargle algorithm, respectively).

4.5.4. Nonlinear variability analysis

Most of the nonlinear methods were proposed 30 years ago. However, there are not as many literatures investigating the sensitivity on data length as the linear HRV analysis. A shorter data length of Poincare plot, MSE, CMSE have been reported and discussed for different purposes without providing any suggestions to minimum data length for reliable measurements. For instance, the short-term assessment of Poincare plot was applied in different stress levels, yet was concluded as promising results.[151,152] For entropy-based HRV

analysis, SampEn and ApEn have been compared and discussed together in most instances since SampEn was introduced to improve the unreliable outcome of ApEn due to data length. It was suggested that a minimum data length of 100 and 250 RR intervals of SampEn and ApEn could distinguish healthy from congestive heart failure patients.[107] Another group studied in the range of two minutes to the 20-minute data length. The authors concluded that SampEn was a lot less sensitive to data length compared to ApEn.[108] Additionally, McNames and Aboy considered several time domain and frequency domain HRV variables with ApEn and indicated that ApEn was the most unreliable one.[149] Although, SampEn has been reported independent of data length compared to ApEn. However, we found 1000 R peaks to be optimum for estimating ApEn or SampEn.

The results of DFA (α) represent the relationship of $F(n)$ and the window sizes n. And obviously, n cannot be larger than the length of the dataset. Therefore, the data length is an essential factor of the accuracy of α. Moreover, a crossover phenomenon was observed when DFA was proposed.[135] Therefore, Peng suggested that at least 24-hour recording was required for diagnostic purposes since the crossover phenomena could play an essential role consistent with our results.

To calculate LLE, the parameters τ and D need to be defined first. In this study, both τ and D increases with the data lengths in HRV. Gao's works had suggested that $D = 2$ should be used when analyzing a finite HRV data set.[153–155]However, others had reported larger parameters for longer data sets and shorter parameters for shorter data sets. For instance, Signorini and Cerutti calculated long-term HRV ($N = 20,000$) with $\tau = 7$ and $D = 10$.[156] And Li's group used $\tau = 1$ and $D = 3$ for less than 5-min data sets

($N = 200 - 355$).[157] Moreover, speaking of the method differences in LE, Rosenstein's LE is known for fast and easy to implement and applicable to small data sets.[146] A minimum of 200 consecutive R-R intervals was suggested as optimum data length for calculating HRV.[157] However, Li and coworkers did not report any statistical evidence supporting their conclusion. On the contrary, we found that data length is significantly different from LLE of 2000 R peaks.

The varying data lengths required for nonlinear and chaos HR analyses can be partially explained by different aspects of the autonomic heart control system which complexity (ApEn, SampEn and MSE) and LLE can measure. For instance, MSE can measure deviations or differences at different time scales thus offering insightful information on temporal dynamical variations of autonomic HR control system. In our laboratory pilot studies we have found strenuous exercises significantly decreased the complexity of HR R-R interval data. However, LLE detects the presence of chaos in heart dynamical control systems by quantifying LEs (exponential divergence of initially close state space trajectories). The computation of LLE utilizing multiple LEs derived from divergence curves requires larger datasets for stable values. Additionally, DFA is an indicator of statistical persistence and antipersistence of HR time series. Persistence indicates the deviation in HR time series is statistically more likely followed by subsequent deviation in the same direction (increase in HR is followed by subsequent increase of HR or decrease is followed by another decrease of HR). On the other hand, antipersistence implies that the deviation is followed by subsequent deviation in opposite direction (increase in HR is followed by

decrease in HR and vice-versa). Since supraspinal mechanisms involuntarily control HR, it is likely the HR control mechanism will naturally produce long-range correlated HR time series, thus requiring at least 1500 data points for robust and stable DFA values.

4.5.5. Limitations

The findings of this study must be seen together with the limitations. Firstly, our study is limited with sample size. Additionally, the subjects were within a limited range of age thus the study is limited in external validity to other age ranges. We will conduct a study with a larger number of participants and broader age ranges in the future. Secondly, this study investigated optimum data length for HRV measures and is limited to the healthy group only. Hence, a future study with pathological groups would be interesting to embolden our findings.

Chapter 4.6: Conclusions

ECG-based analysis of cardiac rhythm is critical for the diagnosis of a heart condition and disease management. In addition, novel clinical decision support systems require quick ECG analysis to assist clinicians. Our effort to shorten the ECG recording duration is vital to improve efficiency and save time and effort for patients and clinical care providers. This could be more critical for patients with frequent artifacts and HRV physiological features extracted from short ECG recordings with high confidence. Our study suggests that ECG data length collected from wearable devices must be optimized and selected such that more consistent and reliable results could be attained with existing laboratory-grade

measurements. In conclusion, this study suggests ultra-short data sequences can be collected and analyzed for quick HRV assessments retaining the rich information from linear/ non-linear variability structure, but with caution since HRV variables are affected differentially to the data length. Chaotic HR analyses such as LLE (Rosenstein and Wolf) and long-range correlation through DFA required longer dataset lengths compared to other nonlinear variability measures like ApEn, SampEn, and MSE.

CHAPTER 5: Sleep event detection from nasal airflow using deep learning algorithm

Chapter 5.1: Introduction

People with obstructive sleep apnea (OSA) suffer from excessive daytime drowsiness, morning headache, or reduced labor and learning capacity and are associated with a higher risk of CVD.[158] However, with the estimation of one billion people affected[159], a proper measure for the severity of this most common sleep-related breathing disorder is yet completely understood.

Currently, the apnea-hypopnea index (AHI), the average number of apnea or hypopnea events captured in an hour of sleep, is a well-accepted estimation for OSA severity. The American Academy of Sleep Medicine (AASM) defined it into three categories – mild (AHI of 5-15), moderate (AHI of 15-30), and severe (AHI of more than 30).[160] Another similar measure, respiratory disturbance index (RDI) included not only AHI but other breathing irregularities, has been proposed as the association of excess sleepiness[161] and risk of mortality in coronary artery diseases.[162] However, relying on a simple count of the event frequency as the only factor, it has been questioned the ability to best represent the disorder.[163] The full picture of physiological characteristics, such as the duration of the apnea and hypopnea events, and the durations, areas, and depths of oxygen desaturation episodes, was omitted to evaluate when only AHI or RDI was considered. Nevertheless, it has been suggested that longer and deeper apnea, hypopnea, or oxygen desaturation episodes are related to higher risks in adverse events.

With that being said, patients with similar AHI may not necessarily show similar sleep apnea-hypopnea syndrome. Hence, several parameters were proposed and discussed in providing more detailed information supplementing AHI.[164–170] For instance, the nocturnal hypoxemia computed by the percentage of the duration under 90% of oxygen saturation could better predict CVD and mortality than AHI.[169–171] Dr. Töyräs's study group published various metrics in considering the durations, areas, and depths for evaluating OSA severity. They found that, with similar AHI, the deceased OSA patients had higher obstruction severity values than the demographically matched alive ones.[165,172] The obstruction severity allows the duration and area of area and hypopnea events to be considered as shown in **Equation 5-1**.[164,165,172]

$$Obstruction\ severity\ = \frac{\sum_{n=1}^{L} n(HypDur_n \times DesArea_n) + \sum_{n=1}^{L} n(ApDur_n \times DesArea_n)}{Index\ time} \quad (5\text{-}1)$$

where individual hypopnea and apnea event duration are denoted as $HypDur$ and $ApDur$, respectively. The area of an individual desaturation event is denoted as $DesArea$. $Index\ time$ is the total analyzed time that is used to normalize different study recording lengths. L is the quantity of individual events in one study recording. Another parameter proposed from the same study group is the desaturation severity (**Equation 5-2**).[164]

It was found as a stronger predictor of daytime sleepiness than AHI.[173] Furthermore, they presented an adjusted-AHI (**Equation 5-3**) which indicates the relationship between AHI and obstruction severity.

$$Desaturation\ severity\ = \frac{\sum_{n=1}^{L} DesArea_n}{Index\ time} \tag{5-2}$$

$$Adjusted\ AHI\ = 5.328\ \times \sqrt{Obstruction\ Severity} \tag{5-3}$$

Another popular alternative metric, hypoxic burden, which is believed as the desaturation severity parameter[167], has been studied as having predictive power in mortality from CVD.[168,174]

Notwithstanding the traditional practice has the AHI to identify OSA severity, it is certainly not adequate in describing the morphology of sleep events. Alternative parameters may reveal missing information to compensate for the insufficiency of AHI being used alone. Additionally, other strategies can be helpful to predict complications. First, factors such as genetics and symptom subtypes are likely to contribute to individual differences. Studies found that the variation between individuals in neurobehavioral impairment during sleep deprivation was trait-like differential vulnerability.[175] Another perspective to improve the severity classification of OSA strategy focuses on identifying more sophisticated patterns using methods such as machine learning and deep learning techniques.[176–180]

Chapter 5.2: Methods

5.2.1. Data collection

Patients who were suggested to receive on-site and overnight polysomnography (PSG) studies by the sleep specialist for further diagnosis at UCI Health Newport – Birth Street were recruited between May 2022 and June 2022 to participate in the study. All patients gave informed consent for the study which was approved by the Institutional Review Board of the University of California (IRB no.). The protocol followed the standard guidelines of a PSG study to monitor patients' sleep.

The sleep recordings were scored manually with sleep stages, respiratory events, and any irregular sleep events by the sleep technicians and physicians. The number of channels recorded per patient was based on their situation. Then, 37 recommended channels were extracted, deidentified, and saved in European data format (EDF) for further analysis.

5.2.2 Data preprocessing

We aim to demonstrate that a single channel acquired from the PSG study can stratify the severity of sleep events through deep learning models. Considering that the dataset was relatively small (more data will be included since this is an ongoing study), two binary classifiers were established for confirming that nasal airflow could be used to stratify the sleep event and non-sleep event. To lessen the computational cost, the nasal airflow signals were originally recorded with 512 Hz sampling frequency and were downsampled to 32 Hz and segmented into 60 seconds recordings.

Data were categorized into two groups, the sleep and non-sleep events, by the annotation. The sleep event for the first classifier was defined based on wherever the word 'Hypopnea' or 'Apnea' contained in the annotation. Possible circumstances such as central hypopnea, obstructive hypopnea, central apnea, and obstructive apnea were included in the sleep group. On the other hand, the sleep event for the second classifier was defined according to the arousal label in the annotation. Only events during the non-rapid eye movement (NREM) sleep and before continuous positive airway pressure (CPAP) therapy (if any) were used in the study. The data preparation demonstrated above was prepared using Matlab (R2021b, The MathWorks, Natick, Massachusetts, USA).

In addition, to avoid imbalanced classes, the quantity of the larger group was reduced to match the smaller group by random selection. For instance, there were 1037 and 769 epochs of non-sleep and sleep events for the first classifier initially, respectively. 769 epochs from the 1,037 non-sleep events were randomly chosen to match the number of sleep events.

The complete data sets for both binary classifiers were split into training and test sets in the ratio of 4:1. For the first classifier, there were 769 apnea-hypopnea and non-apnea-hypopnea events collected then split into 1,230 (80%) and 308 (20%) recordings as training and test sets, respectively. The second classifier had 1,343 recordings for both arousal and non-arousal events and therefore split into 2,148 (80%) training and 538 (20%) test sets.

5.2.3 Neural network architecture

We intended to utilize the nasal airflow signals from the PSG study for predicting apnea-hypopnea and arousal events through two separate deep-learning classification systems. A one-dimensional convolution neural network (1D-CNN) was implemented using Python 3 deep learning framework including Keras and Tensorflow. The integrated development environment (IDE) for data processing was Google Colaboratory.

5.2.3.1 Binary classification for apnea-hypopnea event

A similar structure to an AlexNet[181] including five 1D convolutions, five batch normalization, three max-pooling layers, and two fully connected layers were used to build a classifier and predict in the work. The diagram of the 1D-CNN structure is shown in **Figure 5.1**. The first 1D convolution layer had 64 filters, a kernel size of 11, and a stride of 4. The second had 64 filters, a kernel size of 5, and a stride of 1. The last three 1D convolution layers had 256 filters, a kernel size of 3, and a stride of 1. Each 1D convolution was followed by batch normalization. All the max-pooling layers had a pool size of 3 with a stride size of 2. To reduce overfitting, a dropout rate of 30% was applied for each fully connected layer. The last layer was a softmax activation function that provides binary classification. A sparse categorical cross-entropy loss function with the Adam optimizer was used for model optimization.

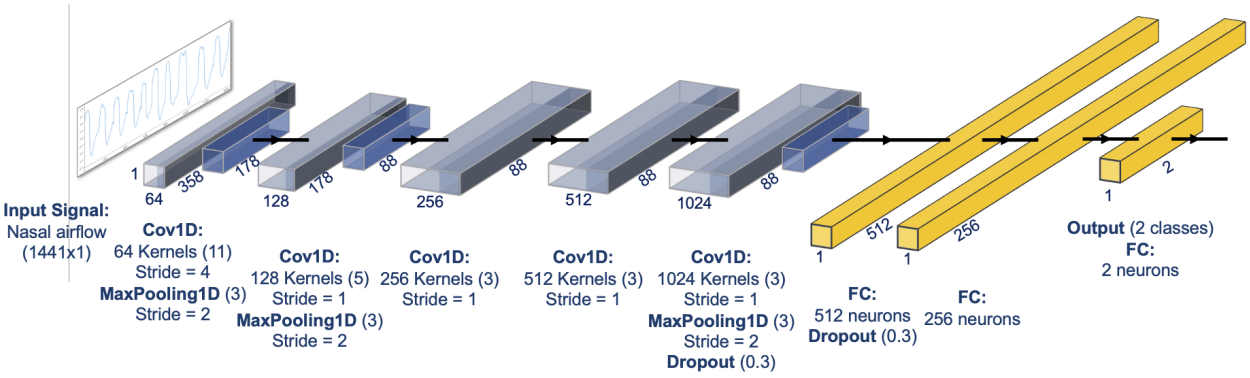

Figure 5.1. 1D-CNN AlexNet applied as a binary classification in the work.

5.2.3.2 Binary classification for arousal event

Similar to the structure in section 5.2.3.1, the binary classifier for arousal event was implemented with an AlexNet, but with the following exceptions. We progressively enlarged the filter numbers in the five 1D convolution layers to capture more complex abstractions. The kernel sizes and strides remained the same but the filter numbers increased subsequently starting from 64, 128, 256, 512, to 1,024.

5.2.4 Cross-validation

K-fold cross-validation is considered a gold standard for machine learning model evaluation. It overcomes the disadvantage of testing part of the dataset only. It provides a more trustworthy result for model performance. A 10-fold cross-validation was used to ensure the bias of subset selection was minimum.

Chapter 5.3: Results

Binary classification for apnea-hypopnea events versus baseline events achieved an accuracy of 87%. The accuracies of training and testing datasets are shown in **Figure 5.2**.

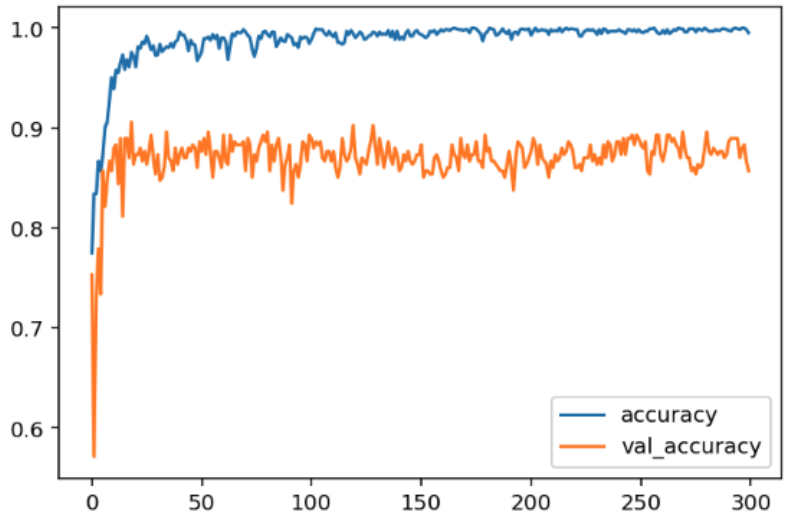

Figure 5.2. The accuracy of binary classification for apnea-hypopnea events. The blue line represents the accuracy of the training dataset. The orange line represents the accuracy of the testing dataset.

The input signal time window of the second binary classification was optimized to 45 seconds with 30 seconds prior to and 15 seconds after the onset of arousal. The input signals of baseline were selected when there were 45 seconds without sleep events. 1,343 signals were prepared for both arousal and non-arousal datasets. The average accuracy after 10-fold cross-validation reached 85%. The loss and accuracy of each fold are shown in **Table 5.1**.

Table 5.1. The loss and accuracy of each fold from 10-fold cross-validation.

Fold	Loss	Accuracy(%)
1	3.945	81.041
2	5.442	85.502
3	4.379	85.130
4	1.841	84.758
5	1.1710	89.591
6	3.4223	83.643
7	2.7648	85.448
8	3.5239	85.075
9	1.8879	81.343
10	3.9301	88.433

CHAPTER 6: Effect of electroacupuncture on heart rate variability and blood pressure variability in subjects with hypertension

Chapter 6.1: Background information

Most of the time, the "silent killer", hypertension, has no obvious symptoms but has strong effects on the human body in many ways such as organ damage. However, it was estimated that nearly half of the adults in the United States were hypertensive, and only about a quarter of them had it controlled.[182] What is even worse is that there is no cure. The common treatments for hypertension are medications and healthy lifestyle habits. An appropriate lifestyle change could potentially have the same efficacy as antihypertensive drugs[183] yet is difficult to sustain.[85] In addition, Diao's work found that the outcome of antihypertensive medications used for treating mild hypertensive adults was controversial and accompanied by adverse effects.[184]

Alternatively, some studies had suggested that both acupuncture and electroacupuncture could manage BP in patients with hypertension.[185–191] Furthermore, Li et al. mentioned that acupuncture therapy was likely to have a long-lasting effect in treating hypertension.[188] Because an overactive sympathetic nervous system plays a dominant role in elevated BP[192–200], this study aims to better understand how EA therapy affect the sympathetic and parasympathetic activities that precipitate hypertension.

The responder and non-responder in the study are defined as whether one's BP after an eight-week intervention reduces in peak and average SBP and DBP compared to the baseline. Besides absolute BP values, HRV and BPV were the major outcome measures.

6.1.1. HRV

HRV measures the variation of heartbeat interval in time. Since HR is mainly regulated by the autonomic nervous system, HRV can be served as a non-invasive index to assess the autonomic activity of the heart. In frequency-domain analysis, the HF component of HRV reflects parasympathetic activity.[201–204] On the other hand, the LF component of HRV was suggested either reflecting mainly on sympathetic activity[204] or a combination of sympathetic and parasympathetic activities[203]. The ratio of LF and HF (LF/HF) reflects the sympathetic modulations.[85] Moreover, frequency-domain HRV had been used to investigate the effect of acupuncture on sympathetic and parasympathetic activities in several studies.[205–207]

6.1.2. BPV

BPV has previously been reported its association with organ damage, cardiovascular event, and mortality[208]. Ultrashort-term BPV is referred to beat-to-beat BP fluctuation with the use of continuous BP devices. Similar to HRV's power spectral analysis, the LF component (0.077~0.15 Hz) of BPV was believed to reflect on sympathetic activity[209].

Chapter 6.2: Methods

6.2.1. Trial design and subjects

The randomized controlled clinical trial aims to evaluate the effectiveness of EA in decreasing BP. Adults with hypertension were recruited at University of California Irvine Health Susan Samueli Integrative Health Institute between May 2022 to October 2022. Volunteers were asked to consent to a screening session including resting ECG recording, 24-hour ambulatory BP monitor (Spacelabs Healthcare, Snoqualmie, Washington, USA), and EndoPAT™ (Itamar Medical, Caesarea, Israel) for eligibility prior to the intervention. Participants who were non-hypertension, pregnant, nursing, have had ischemic heart disease, or did not consent were excluded. All enrolled participants gave informed written consent for the study which was approved by the IRB of the University of California (IRB no. 1999-2222).

The enrolled participants were then randomized into three groups, the authentic electroacupuncture for BP reduction, the sham electroacupuncture, and the wait-list group. The protocols of authentic and sham interventions were similar except that the needles were inserted at different acupoints which neither participants nor researchers knew the settings. Each EA group received eight treatments. Typically, the participants received the treatment once per week for eight weeks except when the schedule was conflicted.

The overall goal of the clinical trial is to investigate the influence of EA treatment on sympathetic and parasympathetic activities. BP, HRV, and BPV collected during the interventions were used as part of the outcome measures to understand the effectiveness of EA and the activities of the sympathetic and parasympathetic nervous systems. Besides a 24-hour ambulatory BP monitor for intermittent BP tracking 24 hours after the treatments, the CAP sensor (Kim et al. 2019) which monitors continuous beat-to-beat BP was used during the weekly visits to track HRV and ultra-short-term BPV.

6.2.2. Experimental protocol

After the participants gave consent, they were asked to go through a screening session to be assessed their eligibility to partake in the study according to the inclusion and exclusion criteria of the clinical trial. Moving forward to the EA intervention, regardless of which group was assigned, the beat-to-beat hemodynamic information was captured by the CAP sensor continuously in every visit. Three BP was measured in a row using an intermittent digital BP monitor on one arm in the sitting position at the beginning of each visit. The participants were then asked to lie down in a supine position for the EA intervention. The CAP sensor was placed on either side of the dorsalis pedis arteries. An acrylic backing and an acupressure wristband (Sea-Band Ltd.) were used to mount the sensor onto the subject's skin. The data from the pressure sensor, accelerometer, and gyroscope was collected on a customized app. On the same side of the body, a wireless intermittent BP monitor, Evolv® (Omron Corporation, Kyoto, Japan) was placed on the upper arm as the BP reference for the CAP sensor. The intermittent BP measurements were

taken at least every 10 minutes. Additional measurements were taken if needed. By design, a total of 50-minute BP readings, a 10-minute baseline, a 30-minute intervention, and a 10-minute post-intervention, were recorded by the CAP system. Three seated BP measurements were obtained again afterward at the end of every visit.

In the fourth week, the participants were asked to wear a 24-hour ambulatory BP monitor. At the end of the eight-week therapy, similar to the examinations prior to the therapy, subjects underwent the 24-hour ambulatory BP and HR monitoring again to compare the changes between pre- and post-therapy.

Chapter 6.3: Results

In the period between May 2022 and October 2022, a total of 15 subjects were originally recruited but only four completed the study (three from the authentic EA group and one from the sham group). The completed four participants are all males. For the 11 subjects who withdrew from the study, there were cases either that the subjects were disqualified from the screening session according to exclusion criteria or that they were unwilling to commit to eight weeks of treatments.

The one subject in the sham group is denoted as C1. The other three subjects in the authentic EA group are denoted as S1, S2, and S3 in the order of when they were recruited. The average BP values from the three measurements at the beginning and last of each visit are shown in **Table 6.1**.

Table 6.1. Averaged SBP and DBP from three intermittent measurements before and after EA treatments.

week	C1		S1		S2		S3	
	Pre-EA	Post-EA	Pre-EA	Post-EA	Pre-EA	Post-EA	Pre-EA	Post-EA
0	146/87	137/77			153/85	151/83	121/72	121/72
1	153/89	158/88	142/80	141/83	169/90	152/84	121/71	121/71
2	150/90	147/88	130/72	134/79	155/91	154/89	128/70	130/74
3	140/85	146/84	136/83	126/76	157/88	149/85	119/66	121/72
4	149/89	150/91	138/79	133/80	139/78	150/78	130/63	129/67
5	138/86	145/84	128/77	127/79	149/88	150/84	120/68	125/65
6	139/84	144//79	141/81	149/87	145/81	129/81	118/75	121/74
7	142/85	151/86	131/78	145/77	162/88	153/83	135/78	113/73
8	155/86	144/80	148/81	148/79	156/89	162/90	124/71	116/66

The data for week 0 (baseline) to week 8 averaged over 24 hours BP and the peak BP taken within 24 hours is shown in **Table 6.2**. In both averaged and peak BP over 24 hours, C1, S1, and S3 results were expected. The BP decreased after eight authentic EA treatments compared to the baseline when no treatment was given to S1 and S3. The data for week 0 (baseline) to week 8 averaged over 24 hours BP and the peak BP taken within 24 hours is shown in **Table 6.2**. In both averaged and peak BP over 24 hours, results of C1, S1, and S3 were expected. The BP decreased after eight authentic EA treatments compared to the baseline when no treatment was given to S1 and S3.

Table 6.2. Averaged and peak BP over 24 hours before (week 0) and after (week 8) a course of eight EA treatments.

	C1	S1	S2	S3
Averaged SBP/DBP over 24hr				
Week 0	131/84	146/94	139/84	130/78
Week 8	138/90	136/87	146/86	117/68
Peak SBP/DBP within 24hr				
Week 0	158/109	181/116	167/104	176/102
Week 8	165/108	170/100	171/100	142/86

Moreover, the study assessed 5-min of HRV and ultra-short-term BPV to investigate how EA treatment effect sympathetic and parasympathetic activities. From the recording of the CAP system, S1 was found to have frequent irregular heartbeats across the weeks. Therefore, S1 was excluded from HRV and BPV calculation. For C1, S2, and S3, HRV and ultra-short-term BPV were evaluated whenever it's applicable since the protocol varied between visits. A representative subject, S3, displayed the trend following that the LF power components, the ratio of HF/LF, and BPV decreased whereas the HF power increased (**Figure 6.1**).

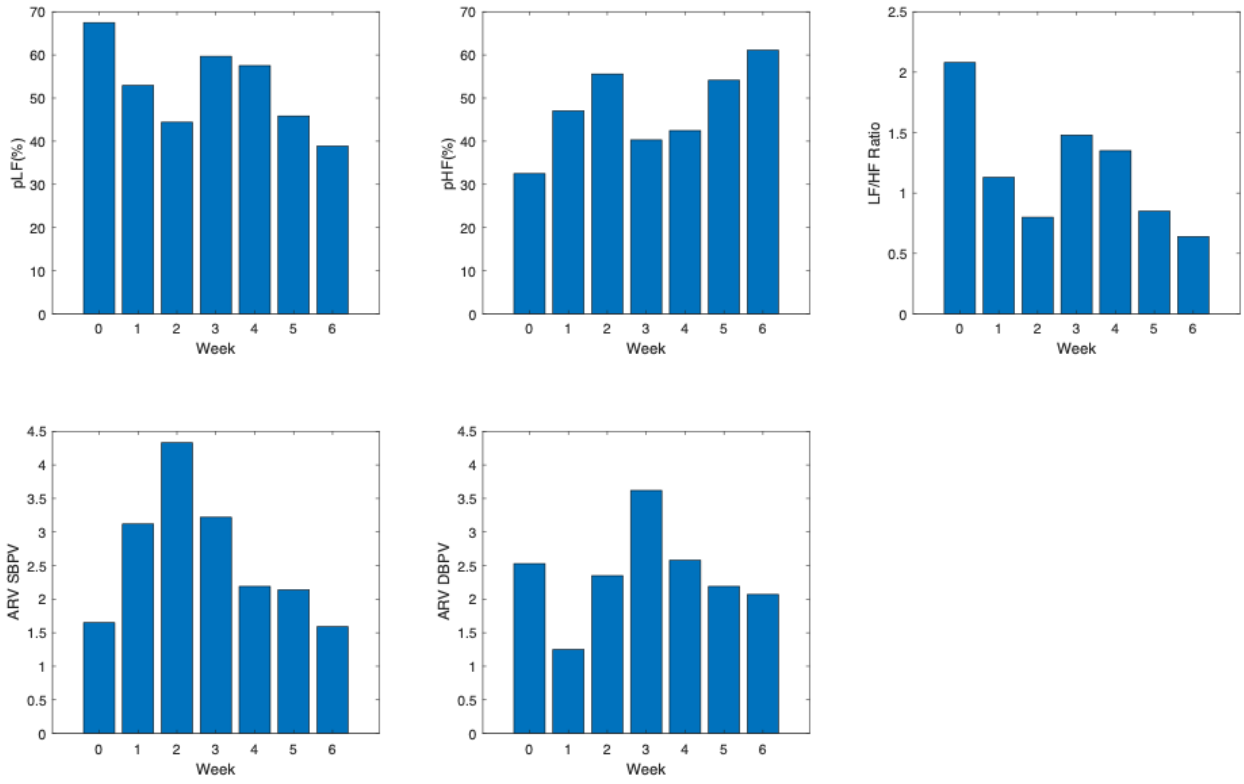

Figure 6.1. 5-min HRV (upper row) and BPV (lower row) of a representative subject from week 0 to week 6. pLF and pHF represent the normalized LF and HF components. ARV represents the average real variability of BPV.

REFERENCES

1. Adab, P., Haroon, S., O'Hara, M. E. & Jordan, R. E. Comorbidities and covid-19. *BMJ* o1431 (2022) doi:10.1136/bmj.o1431.
2. Djaharuddin, I. *et al.* Comorbidities and mortality in COVID-19 patients. *Gaceta Sanitaria* **35**, S530–S532 (2021).
3. Grand View Research. *Health Sensors Market Size, Share & Trends Analysis Report By Application, By Product, By Region And Segment Forecasts, 2022-2030*. (2022).
4. Future Market Insights, Inc. Diversification of Product Portfolio to Accelerate the Wearable Medical Devices Market Growth Rate to 28.1% through 2032. (2022).
5. Mass Needham. Wearables Market Sees First Decline at Beginning of 2022 as Demand Normalizes, According to IDC. https://www.idc.com/getdoc.jsp?containerId=prUS49250022 (2022).
6. Ibáñez, V., Silva, J., Navarro, E. & Cauli, O. Sleep assessment devices: types, market analysis, and a critical view on accuracy and validation. *Expert Review of Medical Devices* **16**, 1041–1052 (2019).
7. Milner, Q. J. W. & Mathews, G. R. An assessment of the accuracy of pulse oximeters: Accuracy of pulse oximeters. *Anaesthesia* **67**, 396–401 (2012).
8. Case, M. A., Burwick, H. A., Volpp, K. G. & Patel, M. S. Accuracy of Smartphone Applications and Wearable Devices for Tracking Physical Activity Data. *JAMA* **313**, 625 (2015).
9. Haghayegh, S., Khoshnevis, S., Smolensky, M. H., Diller, K. R. & Castriotta, R. J. Accuracy of Wristband Fitbit Models in Assessing Sleep: Systematic Review and Meta-Analysis. *J Med Internet Res* **21**, e16273 (2019).
10. Nuss, K. J. *et al.* Assessment of Accuracy of Overall Energy Expenditure Measurements for the Fitbit Charge HR 2 and Apple Watch. *am j health behav* **43**, 498–505 (2019).
11. Hajj-Boutros, G., Landry-Duval, M.-A., Comtois, A. S., Gouspillou, G. & Karelis, A. D.

Wrist-worn devices for the measurement of heart rate and energy expenditure: A validation study for the Apple Watch 6, Polar Vantage V and Fitbit Sense. *European Journal of Sport Science* 1–13 (2022) doi:10.1080/17461391.2021.2023656.

12. Lee, C., Lee, C., Fernando, C. & Chow, C.-M. Comparison of Apple Watch Series 4 vs. KardiaMobile: A Tale of Two Devices. *CJC Open* S2589790X22001391 (2022) doi:10.1016/j.cjco.2022.07.011.

13. Meidert, A. S., Briegel, J. & Saugel, B. Grundlagen und Fallstricke der arteriellen Blutdruckmessung. *Anaesthesist* **68**, 637–650 (2019).

14. Roach, J. K. & Thiele, R. H. Perioperative blood pressure monitoring. *Best Practice & Research Clinical Anaesthesiology* **33**, 127–138 (2019).

15. Kim, J. *et al.* Soft Wearable Pressure Sensors for Beat-to-Beat Blood Pressure Monitoring. *Adv. Healthcare Mater.* **8**, 1900109 (2019).

16. Association for the Advancement of Medical Instrumentation. Non-invasive sphygmomanometers. Part 2: Clinical investigation of automated measurement type. (2013).

17. Wall, C., Moore, J. & Thachil, J. Catheter-related thrombosis: A practical approach. *Journal of the Intensive Care Society* **17**, 160–167 (2016).

18. O'Horo, J. C., Maki, D. G., Krupp, A. E. & Safdar, N. Arterial Catheters as a Source of Bloodstream Infection: A Systematic Review and Meta-Analysis*. *Critical Care Medicine* **42**, 1334–1339 (2014).

19. Adrie, C. *et al.* Attributable mortality of ICU-acquired bloodstream infections: Impact of the source, causative micro-organism, resistance profile and antimicrobial therapy. *Journal of Infection* **74**, 131–141 (2017).

20. Nuttall, G. *et al.* Surgical and Patient Risk Factors for Severe Arterial Line Complications in Adults. *Anesthesiology* **124**, 590–597 (2016).

21. Gershengorn, H. B. *et al.* Variation of Arterial and Central Venous Catheter Use in United States Intensive Care Units. *Anesthesiology* **120**, 650–664 (2014).

22. Lakhal, K., Ehrmann, S. & Boulain, T. Noninvasive BP Monitoring in the Critically Ill. *Chest* **153**, 1023–1039 (2018).

23. Meidert, A. S. & Saugel, B. Techniques for Non-Invasive Monitoring of Arterial Blood Pressure. *Front. Med.* **4**, 231 (2018).

24. Chung, E., Chen, G., Alexander, B. & Cannesson, M. Non-invasive continuous blood pressure monitoring: a review of current applications. *Front. Med.* **7**, 91–101 (2013).

25. Penáz, J., Voigt, A. & Teichmann, W. [Contribution to the continuous indirect blood pressure measurement]. *Z Gesamte Inn Med* **31**, 1030–1033 (1976).

26. Landowne, M. A Method Using Induced Waves to Study Pressure Propagation in Human Arteries. *Circulation Research* **5**, 594–601 (1957).

27. Yoon, Y., Cho, J. H. & Yoon, G. Non-constrained Blood Pressure Monitoring Using ECG and PPG for Personal Healthcare. *J Med Syst* **33**, 261–266 (2009).

28. Cattivelli, F. S. & Garudadri, H. Noninvasive Cuffless Estimation of Blood Pressure from Pulse Arrival Time and Heart Rate with Adaptive Calibration. in *2009 Sixth International Workshop on Wearable and Implantable Body Sensor Networks* 114–119 (IEEE, 2009). doi:10.1109/BSN.2009.35.

29. Ma, H. T. A Blood Pressure Monitoring Method for Stroke Management. *BioMed Research International* **2014**, 1–7 (2014).

30. Shen, Z., Miao, F., Meng, Q. & Li, Y. Cuffless and continuous blood pressure estimation based on multiple regression analysis. in *2015 5th International Conference on Information Science and Technology (ICIST)* 117–120 (IEEE, 2015). doi:10.1109/ICIST.2015.7288952.

31. Ghosh, S. *et al.* Continuous blood pressure prediction from pulse transit time using ECG and PPG signals. in *2016 IEEE Healthcare Innovation Point-Of-Care Technologies Conference (HI-POCT)* 188–191 (IEEE, 2016). doi:10.1109/HIC.2016.7797728.

32. Lass, J. *et al.* Continuous blood pressure monitoring during exercise using pulse wave transit time measurement. in *The 26th Annual International Conference of the IEEE*

Engineering in Medicine and Biology Society vol. 3 2239–2242 (IEEE, 2004).

33. Chen, Y., Wen, C., Tao, G., Bi, M. & Li, G. Continuous and Noninvasive Blood Pressure Measurement: A Novel Modeling Methodology of the Relationship Between Blood Pressure and Pulse Wave Velocity. *Ann Biomed Eng* **37**, 2222–2233 (2009).

34. Gesche, H., Grosskurth, D., Küchler, G. & Patzak, A. Continuous blood pressure measurement by using the pulse transit time: comparison to a cuff-based method. *Eur J Appl Physiol* **112**, 309–315 (2012).

35. Ma, Y. *et al.* Relation between blood pressure and pulse wave velocity for human arteries. *Proc Natl Acad Sci USA* **115**, 11144–11149 (2018).

36. D. Unglaub Silverthorn. *Human Physiology: An Integrated Approach*. (Pearson, 2013).

37. Novak, V. *et al.* Influence of respiration on heart rate and blood pressure fluctuations. *Journal of Applied Physiology* **74**, 617–626 (1993).

38. Schramm, P. *et al.* Noninvasive Hemodynamic Measurements During Neurosurgical Procedures in Sitting Position. *Journal of Neurosurgical Anesthesiology* **29**, 251–257 (2017).

39. Balzer, F. *et al.* Comparison of the non-invasive Nexfin® monitor with conventional methods for the measurement of arterial blood pressure in moderate risk orthopaedic surgery patients. *J Int Med Res* **44**, 832–843 (2016).

40. Heusdens, J. F. *et al.* Validation of non-invasive arterial pressure monitoring during carotid endarterectomy. *British Journal of Anaesthesia* **117**, 316–323 (2016).

41. Martin Bland, J. & Altman, DouglasG. STATISTICAL METHODS FOR ASSESSING AGREEMENT BETWEEN TWO METHODS OF CLINICAL MEASUREMENT. *The Lancet* **327**, 307–310 (1986).

42. Lakhal, K., Martin, M., Ehrmann, S. & Boulain, T. Noninvasive monitors of blood pressure in the critically ill: What are acceptable accuracy and precision? *European Journal of Anaesthesiology* **32**, 367–368 (2015).

43. Chou, E.-F. *et al.* Clinical Validation of a Soft Wireless Continuous Blood Pressure

Sensor During Surgery. *Front. Digit. Health* **3**, 696606 (2021).

44. Garland, A. Arterial Lines in the ICU. *Chest* **146**, 1155–1158 (2014).

45. Durie, M., Beckmann, U. & Gillies, D. M. Incidents Relating to Arterial Cannulation as Identified in 7525 Reports Submitted to the Australian Incident Monitoring Study (AIMS—ICU). *Anaesth Intensive Care* **30**, 60–65 (2002).

46. Olga V, S., Muhammad A, A. & Alan M, S. Postoperative Hypertension: When Blood Pressure Cuff and Arterial Line Disagree. *J Clin Anesth Pain Manag* **3**, (2019).

47. Kallioinen, N., Hill, A., Horswill, M. S., Ward, H. E. & Watson, M. O. Sources of inaccuracy in the measurement of adult patients' resting blood pressure in clinical settings: a systematic review. *Journal of Hypertension* **35**, 421–441 (2017).

48. Picone, D. S. *et al.* Accuracy of Cuff-Measured Blood Pressure. *Journal of the American College of Cardiology* **70**, 572–586 (2017).

49. Whelton PK *et al.* Correction to: 2017 ACC/AHA/AAPA/ABC/ACPM/AGS/APhA/ASH/ASPC/NMA/PCNA Guideline for the Prevention, Detection, Evaluation, and Management of High Blood Pressure in Adults: Executive Summary: A Report of the American College of Cardiology/American Heart Association Task Force on Clinical Practice Guidelines. *Hypertension* **71**, (2018).

50. Bartels, K., Esper, S. A. & Thiele, R. H. Blood Pressure Monitoring for the Anesthesiologist: A Practical Review. *Anesthesia & Analgesia* **122**, 1866–1879 (2016).

51. Lakhal, K. *et al.* The CNAP™ Finger Cuff for Noninvasive Beat-To-Beat Monitoring of Arterial Blood Pressure: An Evaluation in Intensive Care Unit Patients and a Comparison with 2 Intermittent Devices. *Anesthesia & Analgesia* **123**, 1126–1135 (2016).

52. Ruiz-Rodríguez, J. C. *et al.* Innovative continuous non-invasive cuffless blood pressure monitoring based on photoplethysmography technology. *Intensive Care Med* **39**, 1618–1625 (2013).

53. Raichle, C. J. *et al.* Performance of a Blood Pressure Smartphone App in Pregnant

Women: The iPARR Trial (iPhone App Compared With Standard RR Measurement). *Hypertension* **71**, 1164–1169 (2018).

54. Wang, C. *et al.* Monitoring of the central blood pressure waveform via a conformal ultrasonic device. *Nat Biomed Eng* **2**, 687–695 (2018).

55. Sempionatto, J. R. *et al.* An epidermal patch for the simultaneous monitoring of haemodynamic and metabolic biomarkers. *Nat Biomed Eng* **5**, 737–748 (2021).

56. Greiwe, G. *et al.* Is applanation tonometry a reliable method for monitoring blood pressure in morbidly obese patients undergoing bariatric surgery? *British Journal of Anaesthesia* **116**, 790–796 (2016).

57. Greiwe, G. *et al.* Comparison of blood pressure monitoring by applanation tonometry and invasively assessed blood pressure in cardiological patients. *J Clin Monit Comput* **32**, 817–823 (2018).

58. Lee, T.-Y., Vo, K., Baek, W., Khine, M. & Dutt, N. STINT: selective transmission for low-energy physiological monitoring. in *Proceedings of the ACM/IEEE International Symposium on Low Power Electronics and Design* 115–120 (ACM, 2020). doi:10.1145/3370748.3406563.

59. Wilkes, M. P., Bennett, A., Hall, P., Lewis, M. & Clutton-Brock, T. H. Comparison of invasive and non-invasive measurement of continuous arterial pressure using the Finapres in patients undergoing spinal anaesthesia for lower segment Caesarean section. *British Journal of Anaesthesia* **73**, 738–743 (1994).

60. Bland, J. M. & Altman, D. G. Measuring agreement in method comparison studies. *Stat Methods Med Res* **8**, 135–160 (1999).

61. Bland, J. M. & Altman, D. G. Agreement Between Methods of Measurement with Multiple Observations Per Individual. *Journal of Biopharmaceutical Statistics* **17**, 571–582 (2007).

62. Chan, Y. H. Biostatistics 104: correlational analysis. *Singapore Med J* **44**, 614–619 (2003).

63. Gayat, E. *et al.* CNAP ® does not reliably detect minimal or maximal arterial blood pressures during induction of anaesthesia and tracheal intubation: CNAP during induction of anaesthesia. *Acta Anaesthesiol Scand* **57**, 468–473 (2013).

64. Ghamri, Y. *et al.* Automated Pulse Oximeter Waveform Analysis to Track Changes in Blood Pressure During Anesthesia Induction: A Proof-of-Concept Study. *Anesthesia & Analgesia* **130**, 1222–1233 (2020).

65. Janelle, G. M. & Gravenstein, N. An Accuracy Evaluation of the T-Line® Tensymeter (Continuous Noninvasive Blood Pressure Management Device) versus Conventional Invasive Radial Artery Monitoring in Surgical Patients. *Anesthesia & Analgesia* **102**, 484–490 (2006).

66. Kaisti, M. *et al.* Clinical assessment of a non-invasive wearable MEMS pressure sensor array for monitoring of arterial pulse waveform, heart rate and detection of atrial fibrillation. *npj Digit. Med.* **2**, 39 (2019).

67. Esper, S. A. & Pinsky, M. R. Arterial waveform analysis. *Best Practice & Research Clinical Anaesthesiology* **28**, 363–380 (2014).

68. O'Rourke, M. F. Wave Reflections and the Arterial Pulse. *Arch Intern Med* **144**, 366 (1984).

69. Pollreisz, D. & TaheriNejad, N. Detection and Removal of Motion Artifacts in PPG Signals. *Mobile Netw Appl* **27**, 728–738 (2022).

70. Chou, E.-F., Khine, M., Lockhart, T. & Soangra, R. Effects of ECG Data Length on Heart Rate Variability among Young Healthy Adults. *Sensors* **21**, 6286 (2021).

71. Tang, L. & Liu, G. The novel approach of temporal dependency complexity analysis of heart rate variability in obstructive sleep apnea. *Computers in Biology and Medicine* **135**, 104632 (2021).

72. Shashikant, R., Chaskar, U., Phadke, L. & Patil, C. Gaussian process-based kernel as a diagnostic model for prediction of type 2 diabetes mellitus risk using non-linear heart rate variability features. *Biomed. Eng. Lett.* **11**, 273–286 (2021).

73. Wu, S., Chen, M., Wang, J., Shi, B. & Zhou, Y. Association of Short-Term Heart Rate Variability With Breast Tumor Stage. *Front. Physiol.* **12**, 678428 (2021).

74. Shi, B. *et al.* Nonlinear heart rate variability biomarkers for gastric cancer severity: A pilot study. *Sci Rep* **9**, 13833 (2019).

75. Malpas, S. C., Whiteside, E. A. & Maling, T. J. Heart rate variability and cardiac autonomic function in men with chronic alcohol dependence. *Heart* **65**, 84–88 (1991).

76. Kudat, H. *et al.* Heart Rate Variability in Diabetes Patients. *J Int Med Res* **34**, 291–296 (2006).

77. Stein, P. K. & Reddy, A. Non-linear heart rate variability and risk stratification in cardiovascular disease. *Indian Pacing Electrophysiol J* **5**, 210–220 (2005).

78. Thayer, J. F., Yamamoto, S. S. & Brosschot, J. F. The relationship of autonomic imbalance, heart rate variability and cardiovascular disease risk factors. *International Journal of Cardiology* **141**, 122–131 (2010).

79. Sajadieh, A. Increased heart rate and reduced heart-rate variability are associated with subclinical inflammation in middle-aged and elderly subjects with no apparent heart disease. *European Heart Journal* **25**, 363–370 (2004).

80. Lampert, R. *et al.* Decreased heart rate variability is associated with higher levels of inflammation in middle-aged men. *American Heart Journal* **156**, 759.e1-759.e7 (2008).

81. Williams, D. P. *et al.* Heart rate variability and inflammation: A meta-analysis of human studies. *Brain, Behavior, and Immunity* **80**, 219–226 (2019).

82. Chalmers, J. A., Quintana, D. S., Abbott, M. J.-A. & Kemp, A. H. Anxiety Disorders are Associated with Reduced Heart Rate Variability: A Meta-Analysis. *Front. Psychiatry* **5**, (2014).

83. Gorman, J. M. & Sloan, R. P. Heart rate variability in depressive and anxiety disorders. *American Heart Journal* **140**, S77–S83 (2000).

84. Shaffer, F. & Ginsberg, J. P. An Overview of Heart Rate Variability Metrics and Norms. *Front. Public Health* **5**, 258 (2017).

85. Electrophysiology, T. F. of the E. S. of C. the N. A. Heart Rate Variability: Standards of Measurement, Physiological Interpretation, and Clinical Use. *Circulation* **93**, 1043–1065 (1996).

86. Henriques, T. *et al.* Nonlinear Methods Most Applied to Heart-Rate Time Series: A Review. *Entropy* **22**, 309 (2020).

87. Rhea, C. K. *et al.* Noise and Complexity in Human Postural Control: Interpreting the Different Estimations of Entropy. *PLoS ONE* **6**, e17696 (2011).

88. Singh, B., Singh, M. & Banga, V. K. Sample Entropy based HRV: Effect of ECG Sampling Frequency. *Biomedical Science and Engineering* **2**, 68–72 (2014).

89. McCamley, J., Denton, W., Arnold, A., Raffalt, P. & Yentes, J. On the Calculation of Sample Entropy Using Continuous and Discrete Human Gait Data. *Entropy* **20**, 764 (2018).

90. Raffalt, P. C., McCamley, J., Denton, W. & Yentes, J. M. Sampling frequency influences sample entropy of kinematics during walking. *Med Biol Eng Comput* **57**, 759–764 (2019).

91. Ramdani, S., Bouchara, F. & Lagarde, J. Influence of noise on the sample entropy algorithm. *Chaos* **19**, 013123 (2009).

92. Casaleggio, A. & Braiotta, S. Estimation of Lyapunov exponents of ECG time series—The influence of parameters. *Chaos, Solitons & Fractals* **8**, 1591–1599 (1997).

93. Xinnian Chen, Solomon, I. C. & Chon, K. H. Comparison of the Use of Approximate Entropy and Sample Entropy: Applications to Neural Respiratory Signal. in *2005 IEEE Engineering in Medicine and Biology 27th Annual Conference* 4212–4215 (IEEE, 2005). doi:10.1109/IEMBS.2005.1615393.

94. Kaffashi, F., Foglyano, R., Wilson, C. G. & Loparo, K. A. The effect of time delay on Approximate & Sample Entropy calculations. *Physica D: Nonlinear Phenomena* **237**, 3069–3074 (2008).

95. Singh, B. & Singh, D. Effect of Threshold Value r on Multiscale Entropy based Heart Rate Variability. *Cardiovasc Eng Tech* **3**, 211–216 (2012).

96. Estrada, L., Torres, A., Sarlabous, L. & Jané, R. Influence of Parameter Selection in Fixed Sample Entropy of Surface Diaphragm Electromyography for Estimating Respiratory Activity. *Entropy* **19**, 460 (2017).

97. Stergious, N. *Nonlinear Analysis for Human Movement Variability*. (CRC Press, 2018).

98. Yokus, M. A. & Jur, J. S. Fabric-Based Wearable Dry Electrodes for Body Surface Biopotential Recording. *IEEE Trans. Biomed. Eng.* **63**, 423–430 (2016).

99. Arquilla, K., Webb, A. & Anderson, A. Textile Electrocardiogram (ECG) Electrodes for Wearable Health Monitoring. *Sensors* **20**, 1013 (2020).

100. Crosby, J. Development of a Flexible Printed Paper-Based Battery. (Western Michigan University, 2020).

101. Smith, A.-L., Owen, H. & Reynolds, K. J. Heart rate variability indices for very short-term (30 beat) analysis. Part 1: survey and toolbox. *J Clin Monit Comput* **27**, 569–576 (2013).

102. Munoz, M. L. *et al.* Validity of (Ultra-)Short Recordings for Heart Rate Variability Measurements. *PLoS ONE* **10**, e0138921 (2015).

103. Thong, T., Li, K., McNames, J., Aboy, M. & Goldstein, B. Accuracy of ultra-short heart rate variability measures. in *Proceedings of the 25th Annual International Conference of the IEEE Engineering in Medicine and Biology Society (IEEE Cat. No.03CH37439)* 2424–2427 (IEEE, 2003). doi:10.1109/IEMBS.2003.1280405.

104. Salahuddin, L., Cho, J., Jeong, M. G. & Kim, D. Ultra Short Term Analysis of Heart Rate Variability for Monitoring Mental Stress in Mobile Settings. in *2007 29th Annual International Conference of the IEEE Engineering in Medicine and Biology Society* 4656–4659 (IEEE, 2007). doi:10.1109/IEMBS.2007.4353378.

105. Nussinovitch, U. *et al.* Reliability of Ultra-Short ECG Indices for Heart Rate Variability: Ultra-Short HRV Reliability. *Annals of Noninvasive Electrocardiology* **16**, 117–122 (2011).

106. Choi, W.-J., Lee, B.-C., Jeong, K.-S. & Lee, Y.-J. Minimum Measurement Time Affecting the Reliability of the Heart Rate Variability Analysis. *Korean J Health Promot* **17**, 269 (2017).

107. Graff, B., Graff, G. & Kaczkowska, A. Entropy measures of heart rate variability for short ECG datasets in patients with congestive heart failure. *Acta Phys. Pol. B Proc. Suppl.* **5**, 153 (2012).

108. Singh, M., Singh, B. & Singh, G. Optimal RR-Interval Data Length for Entropy based Heart Rate Variability Analysis. *IJCA* **123**, 39–42 (2015).

109. Lee, D.-Y. & Choi, Y.-S. Multiscale Distribution Entropy Analysis of Short-Term Heart Rate Variability. *Entropy* **20**, 952 (2018).

110. Welch, P. The use of fast Fourier transform for the estimation of power spectra: A method based on time averaging over short, modified periodograms. *IEEE Trans. Audio Electroacoust.* **15**, 70–73 (1967).

111. Lomb, N. R. Least-squares frequency analysis of unequally spaced data. *Astrophys Space Sci* **39**, 447–462 (1976).

112. Estévez, M. *et al.* Spectral analysis of heart rate variability. *International Journal on Disability and Human Development* **15**, (2016).

113. Press, W. H., Flannery, B. P., Teukolsky, A. A. & Vetterling, W. T. *Numerical recipes in C: the art of scientific computing*. (1992).

114. Moody, G. B. Spectral analysis of heart rate without resampling. in *Proceedings of Computers in Cardiology Conference* 715–718 (IEEE Comput. Soc. Press, 1993). doi:10.1109/CIC.1993.378302.

115. Fonseca, D. S., Netto, A. D., Ferreira, R. B. & de Sa, A. M. F. L. M. Lomb-scargle periodogram applied to heart rate variability study. in *2013 ISSNIP Biosignals and Biorobotics Conference: Biosignals and Robotics for Better and Safer Living (BRC)* 1–4 (IEEE, 2013). doi:10.1109/BRC.2013.6487524.

116. Marciano, F., Migaux, M. L., Acanfora, D., Furgi, G. & Rengo, F. Quantification of Poincare' maps for the evaluation of heart rate variability. in *Computers in Cardiology 1994* 577–580 (IEEE Comput. Soc. Press, 1995). doi:10.1109/CIC.1994.470126.

117. Tulppo, M. P., Makikallio, T. H., Takala, T. E., Seppanen, T. & Huikuri, H. V. Quantitative beat-to-beat analysis of heart rate dynamics during exercise. *American Journal of Physiology-Heart and Circulatory Physiology* **271**, H244–H252 (1996).

118. D'Addio, G. *et al.* Reproducibility of short- and long-term Poincare plot parameters compared with frequency-domain HRV indexes in congestive heart failure. in *Computers in Cardiology 1998. Vol. 25 (Cat. No.98CH36292)* 381–384 (IEEE, 1998). doi:10.1109/CIC.1998.731819.

119. Kamen, P. W., Krum, H. & Tonkin, A. M. Poincaré Plot of Heart Rate Variability Allows Quantitative Display of Parasympathetic Nervous Activity in Humans. *Clinical Science* **91**, 201–208 (1996).

120. Brennan, M., Palaniswami, M. & Kamen, P. New insights into the relationship between Poincare plot geometry and linear measures of heart rate variability. in *2001 Conference Proceedings of the 23rd Annual International Conference of the IEEE Engineering in Medicine and Biology Society* vol. 1 526–529 (IEEE, 2001).

121. Pincus, S. M. Approximate entropy as a measure of system complexity. *Proceedings of the National Academy of Sciences* **88**, 2297–2301 (1991).

122. Pincus, S. Approximate entropy (ApEn) as a complexity measure. *Chaos* **5**, 110–117 (1995).

123. Eckmann, J.-P. & Ruelle, D. Ergodic theory of chaos and strange attractors. in *The Theory of Chaotic Attractors* (eds. Hunt, B. R., Li, T.-Y., Kennedy, J. A. & Nusse, H. E.) 273–312 (Springer New York, 1985). doi:10.1007/978-0-387-21830-4_17.

124. Pincus, S. M., Cummins, T. R. & Haddad, G. G. Heart rate control in normal and aborted-SIDS infants. *American Journal of Physiology-Regulatory, Integrative and Comparative Physiology* **264**, R638–R646 (1993).

125. Richman, J. S. & Moorman, J. R. Physiological time-series analysis using approximate entropy and sample entropy. *American Journal of Physiology-Heart and Circulatory*

Physiology **278**, H2039–H2049 (2000).

126. Yentes, J. M. *et al.* The Appropriate Use of Approximate Entropy and Sample Entropy with Short Data Sets. *Ann Biomed Eng* **41**, 349–365 (2013).

127. Montesinos, L., Castaldo, R. & Pecchia, L. On the use of approximate entropy and sample entropy with centre of pressure time-series. *J NeuroEngineering Rehabil* **15**, 116 (2018).

128. Costa, M., Goldberger, A. L. & Peng, C.-K. Multiscale Entropy Analysis of Complex Physiologic Time Series. *Phys. Rev. Lett.* **89**, 068102 (2002).

129. Costa, M., Goldberger, A. L. & Peng, C.-K. Multiscale entropy analysis of biological signals. *Phys. Rev. E* **71**, 021906 (2005).

130. Faes, L., Porta, A., Javorka, M. & Nollo, G. Efficient Computation of Multiscale Entropy over Short Biomedical Time Series Based on Linear State-Space Models. *Complexity* **2017**, 1–13 (2017).

131. Amoud, H., Snoussi, H., Hewson, D., Doussot, M. & Duchene, J. Intrinsic Mode Entropy for Nonlinear Discriminant Analysis. *IEEE Signal Process. Lett.* **14**, 297–300 (2007).

132. Valencia, J. F. *et al.* Refined Multiscale Entropy: Application to 24-h Holter Recordings of Heart Period Variability in Healthy and Aortic Stenosis Subjects. *IEEE Trans. Biomed. Eng.* **56**, 2202–2213 (2009).

133. Wu, S.-D., Wu, C.-W., Lin, S.-G., Wang, C.-C. & Lee, K.-Y. Time Series Analysis Using Composite Multiscale Entropy. *Entropy* **15**, 1069–1084 (2013).

134. Humeau-Heurtier, A. The Multiscale Entropy Algorithm and Its Variants: A Review. *Entropy* **17**, 3110–3123 (2015).

135. Peng, C. -K., Havlin, S., Stanley, H. E. & Goldberger, A. L. Quantification of scaling exponents and crossover phenomena in nonstationary heartbeat time series. *Chaos* **5**, 82–87 (1995).

136. Zbilut, J. P. & Webber, C. L. Embeddings and delays as derived from quantification of

recurrence plots. *Physics Letters A* **171**, 199–203 (1992).

137. Webber, C. L. & Zbilut, J. P. Dynamical assessment of physiological systems and states using recurrence plot strategies. *Journal of Applied Physiology* **76**, 965–973 (1994).

138. Trulla, L. L., Giuliani, A., Zbilut, J. P. & Webber, C. L. Recurrence quantification analysis of the logistic equation with transients. *Physics Letters A* **223**, 255–260 (1996).

139. Eckmann, J.-P., S.Oliffson, K. & David, R. Recurrence plots of dynamical systems. in *World Scientific Series on Nonlinear Science* 441–446 (1995).

140. Takens, F. Detecting strange attractors in turbulence. in *Dynamical Systems and Turbulence, Warwick 1980* (eds. Rand, D. & Young, L.-S.) vol. 898 366–381 (Springer Berlin Heidelberg, 1981).

141. Gao, J. & Cai, H. On the structures and quantification of recurrence plots. *Physics Letters A* **270**, 75–87 (2000).

142. Kennel, M. B., Brown, R. & Abarbanel, H. D. I. Determining embedding dimension for phase-space reconstruction using a geometrical construction. *Phys. Rev. A* **45**, 3403–3411 (1992).

143. Marwan, N., Carmenromano, M., Thiel, M. & Kurths, J. Recurrence plots for the analysis of complex systems. *Physics Reports* **438**, 237–329 (2007).

144. Wallot, S. Recurrence Quantification Analysis of Processes and Products of Discourse: A Tutorial in R. *Discourse Processes* **54**, 382–405 (2017).

145. Wolf, A., Swift, J. B., Swinney, H. L. & Vastano, J. A. Determining Lyapunov exponents from a time series. *Physica D: Nonlinear Phenomena* **16**, 285–317 (1985).

146. Rosenstein, M. T., Collins, J. J. & De Luca, C. J. A practical method for calculating largest Lyapunov exponents from small data sets. *Physica D: Nonlinear Phenomena* **65**, 117–134 (1993).

147. Zulli, R. *et al.* QT Dispersion and Heart Rate Variability Abnormalities in Alzheimer's Disease and in Mild Cognitive Impairment: CARDIOVASCULAR ABNORMALITIES IN

ALZHEIMER'S DISEASE AND MCI. *Journal of the American Geriatrics Society* **53**, 2135–2139 (2005).

148. Giubilei, F. *et al.* Cardiac autonomic dysfunction in patients with Alzheimer disease: possible pathogenetic mechanisms. *Alzheimer Dis Assoc Disord* **12**, 356–361 (1998).

149. Ke, J.-Q. *et al.* Sympathetic skin response and heart rate variability in predicting autonomic disorders in patients with Parkinson disease. *Medicine (Baltimore)* **96**, e6523 (2017).

150. Kallio, M. *et al.* Comparison of heart rate variability analysis methods in patients with Parkinson's disease. *Med. Biol. Eng. Comput.* **40**, 408–414 (2002).

151. Valappil, R. A. *et al.* Exploring the electrocardiogram as a potential tool to screen for premotor Parkinson's disease. *Mov. Disord.* **25**, 2296–2303 (2010).

152. Javorka, M. *et al.* Short-term heart rate complexity is reduced in patients with type 1 diabetes mellitus. *Clinical Neurophysiology* **119**, 1071–1081 (2008).

153. Mussalo, H. *et al.* Heart rate variability and its determinants in patients with severe or mild essential hypertension: HRV and its determinants in severe and mild hypertension. *Clinical Physiology* **21**, 594–604 (2001).

154. Kumar, M. S. *et al.* Cardiovascular Autonomic Dysfunction in Patients of Nonalcoholic Fatty Liver Disease. *International Journal of Hepatology* **2016**, 1–8 (2016).

155. Nguyen Phuc Thu, T. *et al.* Improving methodology in heart rate variability analysis for the premature infants: Impact of the time length. *PLoS ONE* **14**, e0220692 (2019).

156. McNames, J. & Aboy, M. Reliability and accuracy of heart rate variability metrics versus ECG segment duration. *Med Bio Eng Comput* **44**, 747–756 (2006).

157. Baek, H. J., Cho, C.-H., Cho, J. & Woo, J.-M. Reliability of Ultra-Short-Term Analysis as a Surrogate of Standard 5-Min Analysis of Heart Rate Variability. *Telemedicine and e-Health* **21**, 404–414 (2015).

158. Somers, V. K. *et al.* Sleep Apnea and Cardiovascular Disease. *Journal of the American*

College of Cardiology **52**, 686–717 (2008).

159. Benjafield, A. V. *et al.* Estimation of the global prevalence and burden of obstructive sleep apnoea: a literature-based analysis. *The Lancet Respiratory Medicine* **7**, 687–698 (2019).

160. American Academy of Sleep Medicine. Obstructive sleep apnea. *Illinois: American Academy of Sleep Medicine* (2008).

161. Gottlieb, D. J. *et al.* Relation of Sleepiness to Respiratory Disturbance Index: The Sleep Heart Health Study. *Am J Respir Crit Care Med* **159**, 502–507 (1999).

162. Peker, Y., Hedner, J., Kraiczi, H. & Löth, S. Respiratory Disturbance Index: An Independent Predictor of Mortality in Coronary Artery Disease. *Am J Respir Crit Care Med* **162**, 81–86 (2000).

163. Asghari, A. & Mohammadi, F. Is Apnea-Hypopnea Index a proper measure for Obstructive Sleep Apnea severity? *Med J Islam Repub Iran* **27**, 161–162 (2013).

164. Kulkas, A. *et al.* Novel parameters for evaluating severity of sleep disordered breathing and for supporting diagnosis of sleep apnea-hypopnea syndrome. *Journal of Medical Engineering & Technology* **37**, 135–143 (2013).

165. Kulkas, A., Tiihonen, P., Julkunen, P., Mervaala, E. & Töyräs, J. Novel parameters indicate significant differences in severity of obstructive sleep apnea with patients having similar apnea–hypopnea index. *Med Biol Eng Comput* **51**, 697–708 (2013).

166. Kulkas, A. *et al.* Novel parameters reflect changes in morphology of respiratory events during weight loss. *Physiol. Meas.* **34**, 1013–1026 (2013).

167. Leppänen, T., Kulkas, A. & Töyräs, J. The hypoxic burden: also known as the desaturation severity parameter. *European Heart Journal* **40**, 2991–2993 (2019).

168. Azarbarzin, A. *et al.* The hypoxic burden of sleep apnoea predicts cardiovascular disease-related mortality: the Osteoporotic Fractures in Men Study and the Sleep Heart Health Study. *European Heart Journal* **40**, 1149–1157 (2019).

169. Smagula, S. F. *et al.* Actigraphy- and Polysomnography-Measured Sleep Disturbances, Inflammation, and Mortality Among Older Men. *Psychosom Med* **78**, 686–696 (2016).

170. Jung, H. H., Lee, J. H., Baek, H. J., Kim, S. J. & Lee, J. J. Nocturnal Hypoxemia and Periodic Limb Movement Predict Mortality in Patients on Maintenance Hemodialysis. *CJASN* **5**, 1607–1613 (2010).

171. Oldenburg, O. *et al.* Nocturnal hypoxaemia is associated with increased mortality in stable heart failure patients. *Eur Heart J* **37**, 1695–1703 (2016).

172. Muraja-Murro, A. *et al.* The severity of individual obstruction events is related to increased mortality rate in severe obstructive sleep apnea. *J Sleep Res* **22**, 663–669 (2013).

173. Kainulainen, S. *et al.* Severity of Desaturations Reflects OSA-Related Daytime Sleepiness Better Than AHI. *Journal of Clinical Sleep Medicine* **15**, 1135–1142 (2019).

174. Azarbarzin, A., Sands, S. A., Taranto-Montemurro, L., Redline, S. & Wellman, A. Hypoxic burden captures sleep apnoea-specific nocturnal hypoxaemia. *European Heart Journal* **40**, 2989–2990 (2019).

175. P.A. Van Dongen, Maurice D. Baynard, Greg Maislin, & David F. Dinges. Systematic Interindividual Differences in Neurobehavioral Impairment from Sleep Loss: Evidence of Trait-Like Differential Vulnerability. *Sleep* (2004) doi:10.1093/sleep/27.3.423.

176. Ferreira-Santos, D., Amorim, P., Silva Martins, T., Monteiro-Soares, M. & Pereira Rodrigues, P. Enabling Early Obstructive Sleep Apnea Diagnosis With Machine Learning: Systematic Review. *J Med Internet Res* **24**, e39452 (2022).

177. Gutiérrez‐Tobal, G. C. *et al.* Reliability of machine learning to diagnose pediatric obstructive sleep apnea: Systematic review and meta‐analysis. *Pediatric Pulmonology* **57**, 1931–1943 (2022).

178. Tsai, C.-Y. *et al.* Machine learning approaches for screening the risk of obstructive sleep apnea in the Taiwan population based on body profile. *Informatics for Health and Social Care* 1–16 (2021) doi:10.1080/17538157.2021.2007930.

179. Bahrami, M. & Forouzanfar, M. Sleep Apnea Detection From Single-Lead ECG: A Comprehensive Analysis of Machine Learning and Deep Learning Algorithms. *IEEE Trans. Instrum. Meas.* **71**, 1–11 (2022).

180. Borah, S., Gogoi, P., Gohain, P., Boro, C. & Muchahari, M. K. Machine Learning for Detection of Obstructive Sleep Apnoea. in *Smart Intelligent Computing and Applications, Volume 2* (eds. Satapathy, S. C., Bhateja, V., Favorskaya, M. N. & Adilakshmi, T.) vol. 283 243–251 (Springer Nature Singapore, 2022).

181. Krizhevsky, A., Sutskever, I. & Hinton, G. E. ImageNet classification with deep convolutional neural networks. *Commun. ACM* **60**, 84–90 (2017).

182. Centers for Disease Control and Prevention. *Hypertension Cascade: Hypertension Prevalence, Treatment and Control Estimates Among U.S. Adults Aged 18 Years and Older Applying the Criteria from the American College of Cardiology and American Heart Association's 2017 Hypertension Guideline—NHANES 2015–2018*. (2021).

183. Elmer, P. J. *et al.* Effects of Comprehensive Lifestyle Modification on Diet, Weight, Physical Fitness, and Blood Pressure Control: 18-Month Results of a Randomized Trial. *Ann Intern Med* **144**, 485 (2006).

184. Diao, D., Wright, J. M., Cundiff, D. K. & Gueyffier, F. Pharmacotherapy for mild hypertension. *Cochrane Database of Systematic Reviews* **2014**, (2012).

185. Liu, Y. *et al.* Acupuncture lowers blood pressure in mild hypertension patients: A randomized, controlled, assessor-blinded pilot trial. *Complementary Therapies in Medicine* **23**, 658–665 (2015).

186. Flachskampf, F. A. *et al.* Randomized Trial of Acupuncture to Lower Blood Pressure. *Circulation* **115**, 3121–3129 (2007).

187. Yin, C. *et al.* Acupuncture, a promising adjunctive therapy for essential hypertension: a double-blind, randomized, controlled trial. *Neurological Research* **29**, 98–103 (2007).

188. Li, P. *et al. CME Article:* Long-Lasting Reduction of Blood Pressure by

Electroacupuncture in Patients with Hypertension: Randomized Controlled Trial. *Medical Acupuncture* **27**, 253–266 (2015).

189. Zhang, J., Ng, D. & Sau, A. Effects of electrical stimulation of acupuncture points on blood pressure. *Journal of Chiropractic Medicine* **8**, 9–14 (2009).

190. Kim, L.-W. & Zhu, J. Acupuncture for essential hypertension. *Altern Ther Health Med* **16**, 18–29 (2010).

191. Wang, J., Xiong, X. & Liu, W. Acupuncture for essential hypertension. *International Journal of Cardiology* **169**, 317–326 (2013).

192. Grassi, G. Assessment of Sympathetic Cardiovascular Drive in Human Hypertension: Achievements and Perspectives. *Hypertension* **54**, 690–697 (2009).

193. Mancia, G. & Grassi, G. The Autonomic Nervous System and Hypertension. *Circ Res* **114**, 1804–1814 (2014).

194. Grassi, G., Mark, A. & Esler, M. The Sympathetic Nervous System Alterations in Human Hypertension. *Circ Res* **116**, 976–990 (2015).

195. Brook, R. Autonomic imbalance, hypertension, and cardiovascular risk. *American Journal of Hypertension* **13**, S112–S122 (2000).

196. Julius, S., Pascual, A. V. & London, R. Role of Parasympathetic Inhibition in the Hyperkinetic Type of Borderline Hypertension. *Circulation* **44**, 413–418 (1971).

197. Julius, S. The Evidence for a Pathophysiologic Significance of the Sympathetic Overactivity in Hypertension. *Clinical and Experimental Hypertension* **18**, 305–321 (1996).

198. Julius, S. & Nesbitt, S. Sympathetic Overactivity in Hypertension*A Moving Target. *American Journal of Hypertension* **9**, 113S-120S (1996).

199. Esler, M. *et al.* Mild High-Renin Essential Hypertension: Neurogenic Human Hypertension? *N Engl J Med* **296**, 405–411 (1977).

200. Mark, A. L. The sympathetic nervous system in hypertension: a potential long-term regulator of arterial pressure. *J Hypertens Suppl* **14**, S159-165 (1996).

201. Malliani, A., Pagani, M., Lombardi, F. & Cerutti, S. Cardiovascular neural regulation explored in the frequency domain. *Circulation* **84**, 482–492 (1991).

202. van Ravenswaaij-Arts, C. M. A. Heart Rate Variability. *Ann Intern Med* **118**, 436 (1993).

203. Pomeranz, B. *et al.* Assessment of autonomic function in humans by heart rate spectral analysis. *American Journal of Physiology-Heart and Circulatory Physiology* **248**, H151–H153 (1985).

204. Pagani, M. *et al.* Power spectral analysis of heart rate and arterial pressure variabilities as a marker of sympatho-vagal interaction in man and conscious dog. *Circ Res* **59**, 178–193 (1986).

205. Haker, E., Egekvist, H. & Bjerring, P. Effect of sensory stimulation (acupuncture) on sympathetic and parasympathetic activities in healthy subjects. *Journal of the Autonomic Nervous System* **79**, 52–59 (2000).

206. Lee, S. Y. *et al.* Intradermal Acupuncture on *Shen-Men* and *Nei-Kuan* Acupoints Improves Insomnia in Stroke Patients by Reducing the Sympathetic Nervous Activity: A Randomized Clinical Trial. *Am. J. Chin. Med.* **37**, 1013–1021 (2009).

207. Li, Z., Wang, C., Mak, A. F. T. & Chow, D. H. K. Effects of acupuncture on heart rate variability in normal subjects under fatigue and non-fatigue state. *Eur J Appl Physiol* **94**, 633–640 (2005).

208. Parati, G., Ochoa, J. E. & Bilo, G. Blood Pressure Variability, Cardiovascular Risk, and Risk for Renal Disease Progression. *Curr Hypertens Rep* **14**, 421–431 (2012).

209. Stauss, H. M. IDENTIFICATION OF BLOOD PRESSURE CONTROL MECHANISMS BY POWER SPECTRAL ANALYSIS: BP control mechanisms and spectral analysis. *Clinical and Experimental Pharmacology and Physiology* **34**, 362–368 (2007).